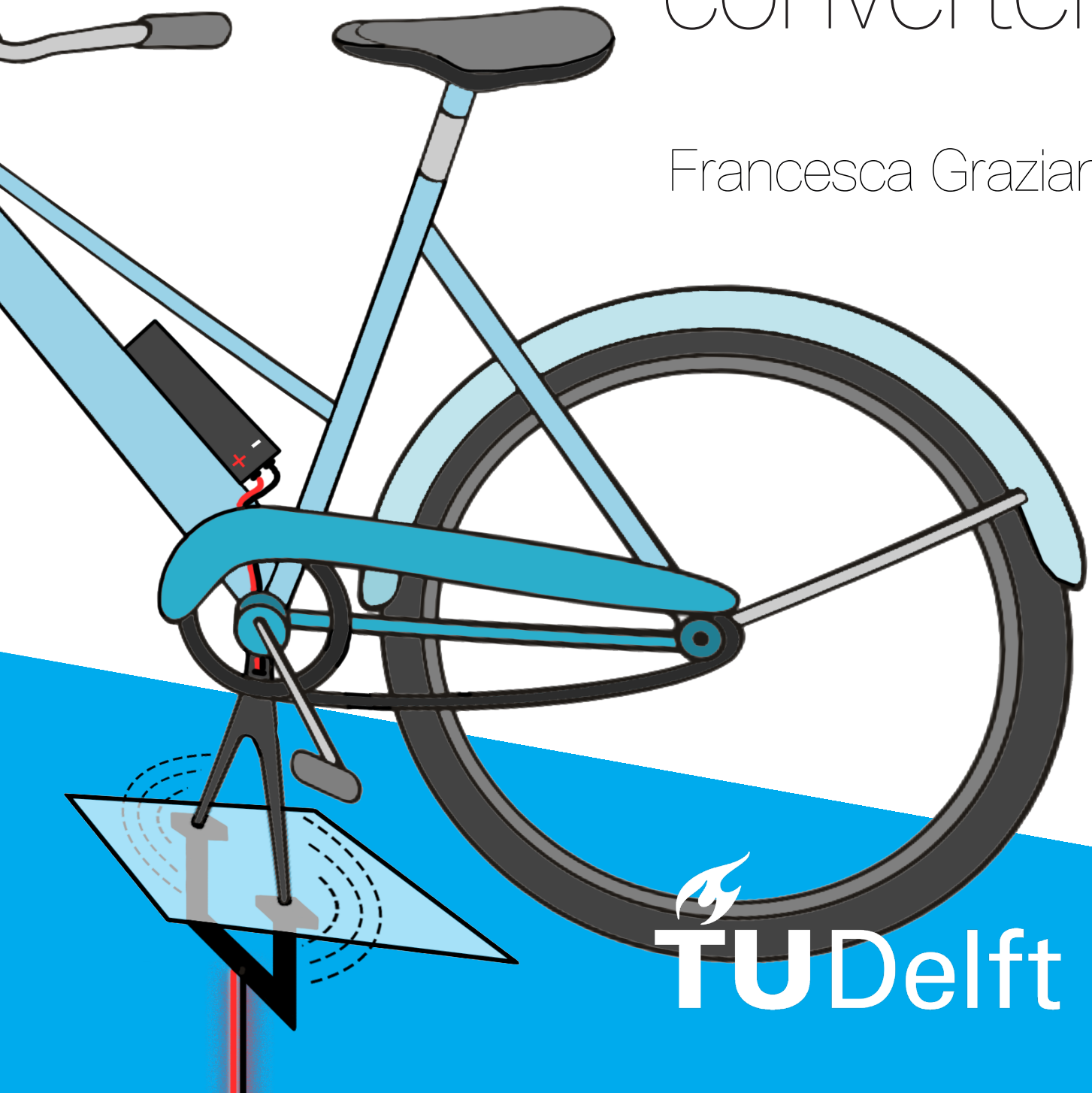


# Control of a resonant wireless e-bike charging converter

Francesca Grazian





# Control of a resonant wireless e-bike charging converter

by

Francesca Grazian

to obtain the degree of Master of Science  
at Delft University of Technology,  
to be defended publicly on Monday October 29, 2018 at 13:00 AM.

Student number: 4626516  
Project duration: February 12, 2018 – October 29, 2018  
Thesis committee: Prof. dr. P. Bauer, TU Delft, supervisor  
Dr. ir. P. J. Van Duijsen, TU Delft, daily supervisor  
Prof. dr. ir. A. H. M. Smets, TU Delft

An electronic version of this thesis is available at <http://repository.tudelft.nl/>.





*Alla mia famiglia,  
che mi sostiene sempre nel seguire i miei sogni.*



# Contents

<b>List of Figures</b>	<b>vii</b>
<b>List of Tables</b>	<b>xiii</b>
<b>Notation</b>	<b>xv</b>
<b>1 Introduction</b>	<b>1</b>
<b>2 Problem Definition</b>	<b>3</b>
2.1 The e-bike WPT charging system . . . . .	3
2.2 System constraints and goals . . . . .	4
2.3 Methodology . . . . .	5
<b>3 Inductive and resonant coupling</b>	<b>7</b>
3.1 Inductive coupling . . . . .	7
3.2 Resonant coupling . . . . .	8
3.3 Series-Series compensation network . . . . .	9
3.3.1 Equivalent circuit and equations . . . . .	9
3.3.2 Analysis of the model. . . . .	11
3.3.3 The bifurcation phenomenon . . . . .	14
3.3.4 Efficiency and Power Factor calculation. . . . .	16
3.3.5 Discussion of the results . . . . .	17
3.4 Double-sided LCC compensation . . . . .	18
<b>4 Power electronics topologies</b>	<b>21</b>
4.1 Single-ended topologies . . . . .	22
4.1.1 ZVS-VS inverter . . . . .	22
4.1.2 ZCS-VS inverter . . . . .	24
4.2 Double-ended topologies. . . . .	27
4.2.1 Royer Inverter . . . . .	27
4.2.2 Half-bridge . . . . .	29
4.2.3 Full-bridge . . . . .	30
4.3 Comparison between fixed frequency and auto-resonant frequency operation . . . . .	31
4.3.1 Zero Voltage Switching operation . . . . .	32
4.3.2 Summary of the comparison between fixed frequency and auto-resonant frequency operation . . . . .	33
<b>5 Comparison between S-S and LCC compensations in the charging system</b>	<b>35</b>
5.1 Series-series compensation in the charging system . . . . .	35
5.1.1 Analysis at variable load $R_L$ and coupling factor $k$ . . . . .	36
5.1.2 Results discussion of S-S compensation . . . . .	38
5.2 LCC compensation in the charging system . . . . .	39
5.2.1 Analysis at variable load $R_L$ and coupling factor $k$ . . . . .	39
5.2.2 Results discussion of double-sided LCC compensation . . . . .	42
5.3 Comparison between LCC and S-S compensation . . . . .	43
<b>6 Power transfer control</b>	<b>45</b>
6.1 Power transfer control: introduction . . . . .	45
6.2 Nominal operating point . . . . .	46
6.2.1 Example on the e-bike WPT charging system . . . . .	46

6.3	The inner control loop . . . . .	50
6.3.1	Reference voltage computation block . . . . .	50
6.3.2	$i_1$ zero-crossing detection block . . . . .	52
6.3.3	Creation of the gating control signals Q and $\bar{Q}$ block . . . . .	53
6.4	Outer control loop . . . . .	54
6.4.1	Phase shifting. . . . .	54
6.4.2	Input DC-link voltage control . . . . .	54
6.4.3	Switching at a multiple of the resonant frequency . . . . .	56
6.4.4	Outer control loop selection . . . . .	56
<b>7</b>	<b>Communication between primary and secondary converters</b>	<b>57</b>
7.1	WPT communication standards . . . . .	57
7.2	Qi version 1.2.3. . . . .	59
7.2.1	Operation sequence . . . . .	59
7.2.2	Amplitude Shift Keying (ASK) communication . . . . .	60
7.2.3	The object detection . . . . .	62
7.2.4	The FOD . . . . .	62
7.2.5	Outer control loop . . . . .	63
7.2.6	Electromagnetic Compatibility (EMC) . . . . .	64
7.3	Communication in the e-bike WPT charging system . . . . .	64
7.3.1	Communication stage at the PRx circuit. . . . .	64
7.3.2	FOD for measuring $k$ . . . . .	65
<b>8</b>	<b>Design of the inner control loop</b>	<b>67</b>
8.1	Design process . . . . .	68
8.2	PCB design . . . . .	73
8.3	Properties of the primary inner control loop . . . . .	73
8.3.1	Analog Control Circuit . . . . .	73
8.3.2	Low Cost Control Circuit . . . . .	74
<b>9</b>	<b>Experimental set-up and results</b>	<b>75</b>
9.1	Model validation . . . . .	75
9.1.1	Measurement of the circuit parameters and $C_1$ selection. . . . .	75
9.1.2	Comparison between theoretical results and measurements . . . . .	77
9.2	Results and performance of the inner control loop . . . . .	81
9.2.1	Start-up transient . . . . .	82
9.2.2	Steady-state operation . . . . .	83
<b>10</b>	<b>Conclusion</b>	<b>85</b>
10.1	Conclusions on the e-bike WPT charging system. . . . .	86
10.2	Recommendations for future research . . . . .	87
	<b>Appendices</b>	<b>89</b>
<b>A</b>	<b>Primary compensation capacitor <math>C_1</math> calculation</b>	<b>91</b>
<b>B</b>	<b>Equivalent circuit and calculation of double-sided LCC compensation</b>	<b>93</b>
<b>C</b>	<b>Matlab Code of the equivalent circuit</b>	<b>97</b>
<b>D</b>	<b>PCB design</b>	<b>101</b>
	<b>Bibliography</b>	<b>103</b>

# List of Figures

1	Voltages and currents in the e-bike WPT charging system for measuring: a) $\eta_{DC}$ , b) $\eta_{AC}$ .	xvii
1.1	The overall e-bike WPT charging system resembles radio waves transmission, where the radio is tuned to the preferred station.	2
2.1	Schematic of the e-bike WPT charging system.	3
2.2	Schematic of the e-bike WPT charging system, including the control loops.	4
2.3	Prototype of the e-bike WPT charging system, already existing from previous projects.	5
2.4	Schematic of the e-bike WPT charging system, starting from the already existing prototype. The red-dashed-line blocks are covered by literature research only, and the green-double-line blocks are covered by the literature research, design and implementation.	5
2.5	Final prototype of the e-bike WPT charging system, starting from the one in Figure 2.3. It includes the two main contributions of this project: the primary compensation network and the inner control loop.	6
3.1	Basic transformer equivalent circuit.	7
3.2	Equivalent input impedance $Z_{in}$ seen from the input voltage $V_{AB}$ .	8
3.3	Four possible compensation networks for the primary and secondary coils. a) Series-Series (S-S), b) Series-Parallel (S-P), c) Parallel-Series(P-S), and d) Parallel-Parallel(P-P).	8
3.4	Equivalent circuit of the S-S compensation network.	9
3.5	a) Absolute peak value and b) phase angle of the voltage $V_1$ across the primary inductor L1 in function of the operating frequency, at different load values, computed from (3.9).	12
3.6	a) Absolute peak value and b) phase angle of the primary current $I_1$ in function of the operating frequency, at different load values, computed from (3.7) and (3.8).	12
3.7	a) Absolute peak value and b) phase angle of the voltage $V_2$ across the secondary inductor L2 in function of the operating frequency, at different load values, computed from (3.10).	12
3.8	a) Absolute peak value and b) phase angle of the secondary current $I_2$ in function of the operating frequency, at different load values, computed from (3.7) and (3.8).	13
3.9	a) Absolute peak value and b) phase angle of the output voltage $V_{ab}$ across the load resistor $R_L$ in function of the operating frequency, at different load values, computed from (3.7) and (3.8).	13
3.10	a) Absolute value and b) phase angle of the equivalent input impedance $Z_{in}$ in function of the operating frequency, at different load values, computed from (3.6).	13
3.11	Plot of $Q_1$ and $Q_x$ for $k=0.1, 0.25$ .	15
3.12	a) Voltage gain $G_v$ , b) Current gain $G_i$ at $k=0.25$ for different values of $R_L$ .	16
3.13	a) Efficiency p.u., b) Power factor (PF) of the wireless power transfer at $k=0.25$ for different values of $R_L$ .	16
3.14	Secondary circuit: a) used for the theoretical model with only AC voltages and currents, b) of the e-bike WPT charging system, with a DC voltage across $R_L$ .	17
3.15	Equivalent circuit of the double-sided LCC compensation network.	18
3.16	a) Primary LC filter. b) Norton equivalent circuit. c) Norton equivalent circuit at the resonant frequency $f_0$ .	18
4.1	Block diagram of the e-bike WPT charging system, pointing out the converters and the compensation networks.	21
4.2	The secondary converter in its simplest topology: a diode-bridge rectifier. This topology is used in all the further analysis.	21
4.3	Single-ended ZVS-VS inverter schematic.	22

4.4	Waveforms of single-ended ZVS-VS inverter. . . . .	23
4.5	Single-ended ZVS-VS inverter during the interval: a) $[t_0, t_1]$ , b) $[t_1, t_2]$ , c) $[t_2, t_3]$ , and d) $[t_3, t_4]$ . The solid lines are conducting, and the dashed ones are not conducting. . . . .	23
4.6	Single-ended ZCS-VS inverter schematics. . . . .	24
4.7	Waveforms of single-ended ZCS-VS inverter. . . . .	25
4.8	Single-ended ZCS-VS inverter during the interval: a) $[t_0, t_1]$ , and $[t_1, t_2]$ , b) $[t_2, t_3]$ , and $[t_3, t_4]$ . The solid lines are conducting, and the dashed ones are not conducting. . . . .	26
4.9	Self-oscillating Royer inverter schematic. . . . .	27
4.10	Waveforms of the double-ended Royer inverter. . . . .	28
4.11	Half-bridge inverter schematic. . . . .	29
4.12	Full-bridge inverter schematic. . . . .	30
4.13	Transmitter circuit of the e-bike WPT charging system, in which the full-bridge inverter is operating at: a) fixed frequency, and b) auto-resonant frequency. . . . .	31
4.14	Full-bridge inverter working at ZVS in combination of a double-sided LCC compensation network. . . . .	32
5.1	S-S compensation schematic in the e-bike wireless charging system. . . . .	35
5.2	Simulation results of S-S compensated system at $k=0.1$ , depending on the load resistance $R_L$ . Plot of a) DC input power $P_{in}$ , DC output power $P_{out}$ and efficiency $\eta_{DC}$ , b) output voltage $V_{out}$ and current $I_{out}$ across $R_L$ , c) peak current through $L_1$ and $L_2$ , d) peak voltage across $L_1$ , $C_1$ , $L_2$ and $C_2$ . . . . .	36
5.3	Simulation results of S-S compensated system at $k=0.17$ , depending on the load resistance $R_L$ . Plot of a) DC input power $P_{in}$ , DC output power $P_{out}$ and efficiency $\eta_{DC}$ , b) output voltage $V_{out}$ and current $I_{out}$ across $R_L$ , c) peak current through $L_1$ and $L_2$ , d) peak voltage across $L_1$ , $C_1$ , $L_2$ and $C_2$ . . . . .	37
5.4	Simulation results of S-S compensated system at $k=0.25$ , depending on the load resistance $R_L$ . Plot of a) DC input power $P_{in}$ , DC output power $P_{out}$ and efficiency $\eta_{DC}$ , b) output voltage $V_{out}$ and current $I_{out}$ across $R_L$ , c) peak current through $L_1$ and $L_2$ , d) peak voltage across $L_1$ , $C_1$ , $L_2$ and $C_2$ . . . . .	37
5.5	Double-sided LCC compensation schematic in the e-bike WPT charging system. . . . .	39
5.6	Simulation results of double-sided LCC system at $k=0.1$ , depending on the load resistance $R_L$ . Plot of a) DC input power $P_{in}$ , DC output power $P_{out}$ and efficiency $\eta_{DC}$ , b) output voltage $V_{out}$ and current $I_{out}$ across $R_L$ , c) peak current through $L_1$ , $L_2$ , $L_{f1}$ and $L_{f2}$ , d) peak voltage across $L_1$ , $C_1$ , $L_2$ and $C_2$ , e) peak voltage across $L_{f1}$ , $C_{f1}$ , $L_{f2}$ and $C_{f2}$ . . . . .	40
5.7	Simulation results of double-sided LCC system at $k=0.17$ , depending on the load resistance $R_L$ . Plot of a) DC input power $P_{in}$ , DC output power $P_{out}$ and efficiency $\eta_{DC}$ , b) output voltage $V_{out}$ and current $I_{out}$ across $R_L$ , c) peak current through $L_1$ , $L_2$ , $L_{f1}$ and $L_{f2}$ , d) peak voltage across $L_1$ , $C_1$ , $L_2$ and $C_2$ , e) peak voltage across $L_{f1}$ , $C_{f1}$ , $L_{f2}$ and $C_{f2}$ . . . . .	41
5.8	Simulation results of double-sided LCC system at $k=0.25$ , depending on the load resistance $R_L$ . Plot of a) DC input power $P_{in}$ , DC output power $P_{out}$ and efficiency $\eta_{DC}$ , b) output voltage $V_{out}$ and current $I_{out}$ across $R_L$ , c) peak current through $L_1$ , $L_2$ , $L_{f1}$ and $L_{f2}$ , d) peak voltage across $L_1$ , $C_1$ , $L_2$ and $C_2$ , e) peak voltage across $L_{f1}$ , $C_{f1}$ , $L_{f2}$ and $C_{f2}$ . . . . .	42
6.1	Block diagram of e-bike WPT charging system, highlighting the inner and outer control loops. The red-dashed-line blocks (outer control loop) are covered by literature research only and the green-double-line (inner control loop) blocks are covered by the literature research, design and implementation. . . . .	45
6.2	AC analysis at $V_{in} = 48$ V, $k=0.1$ of: a) absolute peak value of $I_1$ , b) absolute peak value of $I_2$ , c) phase angle of $I_1$ . . . . .	47
6.3	AC analysis at $V_{in} = 48$ V, $k=0.17$ of: a) absolute peak value of $I_1$ , b) absolute peak value of $I_2$ , c) phase angle of $I_1$ . . . . .	48
6.4	AC analysis at $V_{in} = 48$ V, $k=0.25$ of: a) absolute peak value of $I_1$ , b) absolute peak value of $I_2$ , c) phase angle of $I_1$ . . . . .	49

6.5	Comparator for zero-current detection. . . . .	50
6.6	Delay in the zero-crossing detection due to the ICs and gate driver delays. . . . .	51
6.7	Example of different $\frac{di_1}{dt}$ , in which the frequency is fixed and the parameter changing is the current amplitude. However, the frequency could also change because of the auto-resonant frequency operation. . . . .	52
6.8	Sub-blocks of the reference voltage computation block. . . . .	52
6.9	Sub-blocks of the $i_1$ zero-crossing detection block. . . . .	53
6.10	Sub-blocks of the creation of the gating control signals Q and $\bar{Q}$ block. . . . .	53
6.11	DC/DC buck converter that changes the input voltage $V_{in}$ of the inverter. . . . .	54
6.12	Combination of HB and FB inverter. . . . .	55
6.13	Start-up simulated waveforms for $V_{in} = 48\text{ V}$ , $k = 0.25$ and $R_L = 4\ \Omega$ , using the combined HB/FB inverter. . . . .	55
6.14	Simulated waveforms at the inverter start-up for $V_{in} = 48\text{ V}$ , $k = 0.1$ and $R_L = 12\ \Omega$ , commutating the inverter any other 3 primary current oscillations for reducing the output power. . . . .	56
7.1	Communication between the primary and secondary converter of the e-bike WPT charging system, via the outer control loop. . . . .	57
7.2	Operation sequence of the communication between the PTx and RTx, according to the Qi specification. . . . .	60
7.3	PRx structure, including the power and the communication stages. The thick arrows represents power signals and the thin arrows communication signals. . . . .	61
7.4	Byte encoding in ASK modulation. . . . .	61
7.5	Packet structure in the ASK modulation. . . . .	62
7.6	Measurement of the quality factor $Q_{meas}$ for the FOD, before the start of the power transfer. . . . .	62
7.7	Power Transfer outer control loop between the PTx and the PRx. . . . .	63
7.8	Communication stage at the DC side of the PRx, for ASK communication. . . . .	64
7.9	Example of modulated voltage for ASK communication, from the PRx to the PTx. In the simulation, the output capacitor $C = 3\ \mu\text{F}$ , the communication resistance $R_{CM} = 40\ \Omega$ , the coupling factor $k = 0.25$ and the load resistance $R_L = 12\ \Omega$ . The top waveform is the voltage across a shunt resistor $V_{shunt}$ in series with the primary coil, and the bottom waveform is the gate-source voltage $V_{gs}$ applied to the switch SW. . . . .	65
7.10	Plot of the simulated quality factors $V1/V2$ depending on the coupling factor $k$ and for different values of $R_L$ , before the start of the power transfer. . . . .	66
7.11	Plot of the simulated quality factors $V1/V2$ depending on the coupling factor $k$ and for different values of $R_L = 60$ and $100\ \Omega$ , before the start of the power transfer. Trend lines between the points are also included. . . . .	66
8.1	Laboratory setup of the e-bike WPT charging system: a) already-existing version, used as a start point; b) addition of the two main contributions of this project, that are the ones highlighted by the double-line. . . . .	67
8.2	Schematic of the designed inner control loop. . . . .	69
8.3	Simulated waveforms of the designed inner control loop in Figure 8.2. . . . .	70
8.4	Differentiator circuit, which takes as input the primary current $i_1$ and gives as output both the positive and negative rectified derivatives $V_{diff+}$ and $V_{diff-}$ , at the zero-crossing. . . . .	70
8.5	Example of measured $v_{i_1}$ and $v_{diff}$ for $I_{1,RMS} = 4.5\text{ A}$ . Channel 1 (yellow waveform) is the short pulse $p_1$ . Channel 2 (green waveform) is the short pulse $p_2$ , inverted. Channel 3 (pink waveform) is $v_{i_1}$ . Channel 4 (blue waveform) is $v_{diff}$ . All the waveforms are shown with a bandwidth of 10 MHz. . . . .	71
8.6	Channel 1 (yellow waveform) is the short pulse $p_1$ . Channel 2 (green waveform) is the short pulse $p_2$ , inverted. Channel 3 (pink waveform) is $v_{i_1}$ . Channel 4 (blue waveform) is $v_{diff}$ . a) Derivative centered at $p_1$ , at the positive slope of $v_{i_{1,B}}$ . b) Derivative centered at $p_2$ , at the positive slope of $v_{i_{1,B}}$ . . . . .	71

8.7	Dependence of the reference $V_{ref}$ voltage on the derivative $V_{diff}$ at the current at the zero-crossing, for both comparators. The measured points are plotted with their linear trend lines, equations and their coefficient of determination $R^2$ . . . . .	72
8.8	Circuits that automatically set the reference voltage $V_{ref}$ depending on the derivative of the primary current $V_{diff}$ . a) $V_{ref+}$ for the positive comparator from $V_{diff+}$ . b) $V_{ref-}$ for the negative comparator from $V_{diff-}$ . . . . .	72
8.9	a) Inner control loop board. b) Entire laboratory setup of the e-bike WPT charging system. . . . .	73
9.1	Open-circuit voltage test. . . . .	76
9.2	Open-circuit voltage test waveforms. The yellow waveform (channel 1) is open-circuit voltage $v_{oc}$ , the green waveform (channel 2) is inverted voltage at the full-bridge output $v_{AB}$ , pink waveform (channel 3) is the voltage across the primary capacitor $C_1$ and the blue waveform (channel 4) is the primary current $i_1$ . . . . .	77
9.3	Comparison between the measured and theoretical peak values of: a) $i_1$ , and b) $i_2$ , depending on the operating frequency, at $V_{in} = 48\text{ V}$ , $k = 0.28$ and different values of $R_L$ . . . . .	77
9.4	Absolute percentage errors of $f$ , $i_1$ and $i_2$ of Figure 9.3. . . . .	78
9.5	Comparison between the measured and the theoretical peak values of: a) $i_1$ , $i_2$ , and b) $Z_{in}$ , depending on the resonant working frequency. Moreover, $V_{in} = 20\text{ V}$ and the rectifier is not included in the set-up. . . . .	78
9.6	Absolute percentage errors of $f$ , $I_1$ , $I_2$ and $Z_{in}$ of Figure 9.5. . . . .	78
9.7	Plot of $i_1$ phase angle depending on the operating frequency and at different $R_L$ values. In the right pictures, the frequencies at which the phase angle is zero are pointed out. . . . .	79
9.8	Plot of $i_1$ absolute peak value depending on the operating frequency and at different $R_L$ values. In the right pictures, the points at which the $i_1$ phase angle is zero are pointed out. . . . .	79
9.9	Plot of $i_2$ absolute peak value depending on the operating frequency and at different $R_L$ values. In the right pictures, the points at which the $i_1$ phase angle is zero are pointed out. . . . .	79
9.10	Plot of $Z_{in}$ phase depending on the operating frequency and at different $R_L$ values. In the right pictures, the points at which the $i_1$ phase angle is zero are pointed out. . . . .	80
9.11	Plot of $Z_{in}$ absolute value depending on the operating frequency and at different $R_L$ values. In the right pictures, the points at which the $i_1$ phase angle is zero are pointed out. . . . .	80
9.12	Plot of $\eta_{AC}$ depending on the operating frequency and at different $R_L$ values. In the right pictures, for each curve, the efficiency achieved with auto-resonant frequency operation is highlighted with a red square, and the one achieved with fixed frequency operation is highlighted with a blue square. . . . .	81
9.13	Start-up waveforms. a) The yellow waveform (channel 1) is the inverter voltage at the primary circuit $v_{AB}$ and the green waveform (channel 2) is the primary current $i_1$ . b) The green waveform (channel 2) is the voltage reference of the negative-current-slope comparator $v_{ref-}$ and the purple waveform (channel 3) is the positive-current-slope comparator $v_{ref+}$ . . . . .	82
9.14	Start-up waveforms. The yellow waveform (channel 1) is the inverter voltage at the primary circuit $v_{AB}$ and the green waveform (channel 2) is the primary current $i_1$ . Time scale: a) $20\text{ }\mu\text{s/div}$ , b) $5\text{ }\mu\text{s/div}$ . . . . .	82
9.15	Steady-state waveforms. The yellow waveform (channel 1) is the inverter voltage at the primary circuit $v_{AB}$ and the green waveform (channel 2) is the primary current $i_1$ . . . . .	83
9.16	Zoom-in of the waveforms in Figure 9.15: a) positive-slope and b) negative-slope zero-crossing of $i_1$ . . . . .	83
B.1	a) Equivalent circuit of the double-sided LCC compensation, treating the coupled inductors as a transformer. b) Equivalent circuit of LCC based on superposition principle: a input voltage applied an the output is shorted. c) Equivalent circuit of LCC based on the superposition principle: input is shorted and a output voltage is applied. . . . .	93
B.2	Simulated $V_{AB}$ and $I_{Lf1}$ . . . . .	95
B.3	Simulated $V_{ab}$ and $I_{Lf2}$ . . . . .	95
B.4	Simulated $I_{Lf1}$ , $I_{L1}$ , $I_{L2}$ and $I_{Lf2}$ . . . . .	95



---

D.1 Controller PCB. . . . .	101
-----------------------------	-----




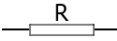
# List of Tables

1	Accuracy of the instruments used for the measurements. . . . .	xvi
2.1	Constraints of the e-bike WPT charging system. . . . .	4
2.2	Goals of the e-bike WPT charging system. . . . .	4
3.1	Primary compensation capacitance $C_1$ for each possible compensation network. . . . .	9
3.2	Value of the parameters used in the circuit analysis. . . . .	11
3.3	Minimum values of $R_L$ for a bifurcation-free operation at $k = 0.1$ and $k = 0.25$ . . . . .	15
4.1	Value of the parameters used in the ZVS-VS inverter analysis. . . . .	24
4.2	Value of the parameters used in the ZVS-VS inverter analysis. . . . .	26
4.3	Value of the parameters used in the circuit analysis of the Royer inverter. . . . .	28
4.4	Comparison between fixed frequency and auto-resonant frequency operation. Each attribute is classified with either a +, - or 0. The + indicates a positive attribute, The - indicates a negative attribute, and the 0 indicates a neutral attribute. . . . .	33
5.1	Value of the parameters used in the circuit analysis. . . . .	41
5.2	Comparison between double-sided LCC and S-S compensation circuits, in the e-bike WPT charging system. . . . .	44
6.1	The resulting $R_{L,min}$ boundary of the bifurcation, at each $k$ are reported. . . . .	47
6.2	$I_{1,max}$ and $I_{2,max}$ peak values at $k=0.1$ , 0.17 and 0.25, distinguishing the cases with bifurcation and with a bifurcation-free operation. The nominal operation at the highest $k$ and $V_{in} = 48$ V is taken as reference. . . . .	49
6.3	Switching table of the HB/FB combined inverter, in Figure 6.12. . . . .	55
7.1	Comparison between WPT standards. . . . .	58
8.1	Components' and approximate total cost for the control circuit. . . . .	74
9.1	Measured primary and secondary resonant inductance values at 100 kHz, for $k = 0$ a $k = k_{max}$ . . . . .	75
9.2	Parameters' value of the set-up, measured at 100 kHz, and $k = k_{max}$ . . . . .	76
9.3	Power transfer efficiency at both ZCS and $I_1 = I_{1,max}$ conditions, for two values of $R_L$ . . . . .	81
9.4	Measured input and output DC voltage and current at $V_{in} = 48$ V, $k = 0.28$ and $R_L = 12 \Omega$ . . . . .	83
10.1	Goals of the e-bike WPT charging system, specifying their actual state in the project. . . . .	86
A.1	Reflected inductance $Z_r$ on the primary circuit. . . . .	91
A.2	Primary compensation capacitance $C_1$ for all the compensation topologies. . . . .	92



# Notation

## Convention

Variable	Variable format	Meaning
$j$	-	Imaginary unit
$A$	$a$	Instantaneous value
	$A$	Absolute value
	$\angle a$	Phase angle in degrees
	$\underline{A}$	Phasor
Circuitual Symbol		Meaning
		Parasitic resistance
		Physical resistor
Definition	Meaning	
Bifurcation Phenomenon	According to the literature, it occurs when a resonant circuit has multiple resonant frequencies. It is not related to its common mathematical meaning: a sudden topological change in the behavior of a system, due to a small smooth change for a parameter value. [1]	

## Error and accuracy

1. *Numerical evaluation of equations.* In case of plots of the equivalent circuit's equations, which are based on phasors, the error is negligible since the capability of the data storage is big. The relative percentage error of the numerical equation solver analysis can be considered  $\leq 1\%$ .
2. *Simulations.*
  - *AC Analysis.* As mentioned in [2], the AC analysis is done in the frequency domain, using the linearized model of non-linear components. The analysis is accurate for steady-state behaviors only, since the non-linearities of the circuits are not present. The phasor method is used to represent voltages and currents, which means that they are complex quantities. The AC analysis consists in the plot of the absolute value and the phase of phasor, depending

on the frequency. The accuracy depends on the chosen number of points per interval. AC analysis <1% as set by the option RELTOL in any spice simulator.

- **Transient Analysis.** For simulating the transient response, a numerical integration method is needed, which determines the numerical solution of the circuit's differential equations. According to [3], the numerical solutions have two errors: the truncation and the round-off error. The truncation error comes from higher terms in the Taylor series expansion, and it is linearly dependent on the time step size. The truncation error of a single point is called local truncation error (LTE), and it decreases as the time step size decreases. However, considering the contribution from all the LTEs, the total truncation error can accumulate. The accumulation happens especially when there is no damping in the circuit, and the LTEs do not compensate each other. The round-off error comes from the limit in the data storage of the numerical results. The local round-off error is generally negligible. However, in case the time step size is small, the accumulated round-off error could be noticeable, because of the high number of points.

The error of the transient analysis is kept below 1% by controlling the time step size of the simulation. The time step is decreased, if the results of the current simulation differ more than 1% from a simulation with a smaller step size.

### 3. Measurements. The accuracy of the measurements depends on the instruments used.

Table 1: Accuracy of the instruments used for the measurements.

		Instrument	Accuracy
Voltage	DC	Multimeter Fluke 289	0.025%
	AC	Differential probe Yokogawa 700924	2% (<400V); 3% (>400V)
Current	DC	Multimeter Fluke 289	0.05%
	AC	Current Probe Yokogawa 701933	1% (<30 Arms); 2% (>30 Arms & <50 Apeak)
		Equation	Accuracy
Efficiency $\eta$ (see Figure 1)	DC	$\eta_{DC} = \frac{V_{in}I_{in}}{V_{out}I_{out}}$	$[(\underbrace{0.025}_{V_{in}} + \underbrace{0.025}_{I_{in}}) + (\underbrace{0.025}_{V_{out}} + \underbrace{0.025}_{I_{out}})]\% = 0.15\%$
	AC	$\eta_{AC} = \sqrt{2} \frac{V_{AB}i_{1,peak}}{i_{2,peak}^2 R_L}^*$	$[(\underbrace{0.025}_{V_{in}} + \underbrace{\frac{1}{i_{1,peak}}}_{i_{1,peak}}) + (\underbrace{\frac{1}{i_{2,peak}}}_{i_{2,peak}} + \underbrace{\frac{1}{i_{2,peak}}}_{i_{2,peak}})]\% \approx 3\%$

\* $\sqrt{2}V_{AB}$  is the first harmonic amplitude of the square wave  $\pm V_{AB}$ . In case the input voltage  $V_{in}$  is fully inverted  $V_{AB} \equiv V_{in}$ .

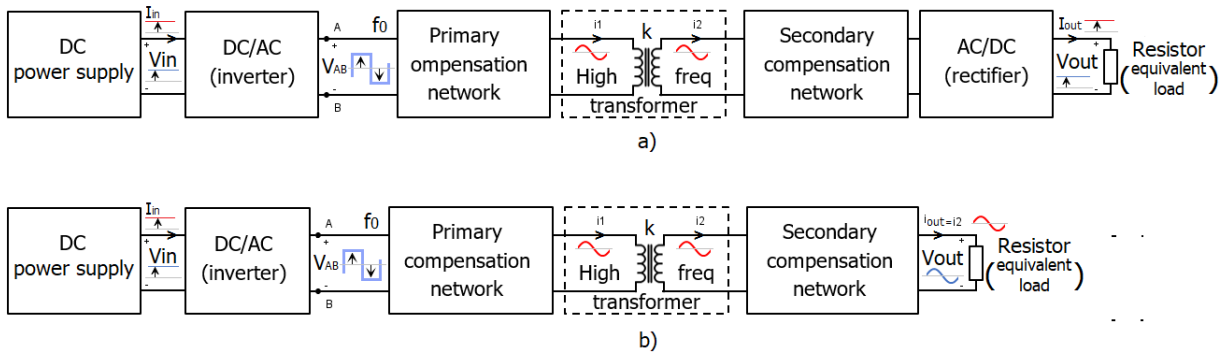


Figure 1: Voltages and currents in the e-bike WPT charging system for measuring: a)  $\eta_{DC}$ , b)  $\eta_{AC}$ .





# Introduction

The Wireless Power Transfer (WPT) has been introduced decades ago for low power applications, and more recently, it has been used for industrial high power applications. WPT is gaining popularity because it presents several advantages over the power transfer through cable. Firstly, the WPT gives galvanic isolation between the power source and the load. Secondly, in some situations it is unfeasible or problematic to place a cable between the two parts. As an example, in some medical applications it is inconvenient and unsafe to place devices inside the human body that need to be charged through a cable. Thirdly, considering that the number of e-vehicles (EVs) is expected to increase exponentially over the next years, the WPT can allow both static and dynamic wireless charging. Since the batteries have longer charging time than the refueling times, it would be engaging to realize an on-road charging system, that could reduce the charging times dramatically, and even eliminate the need for the battery. On-road charging is already present as overhead lines for EVs in public transportation, such as trains, trams, and trolleybuses. However, it is infeasible for private EVs. Finally, most of the portable devices that need to be charged do not have a cable standardization yet. This requires the users to bring along all the cables, since it is difficult to find them from third parties. This situation becomes even more critical in case the cables are bulky, and there is no possibility to store them somewhere.

The WPT can happen in different ways, depending on the transmitter (Tx) and receiver (Rx) configuration. All of them are explained in [4].

1. *Radio frequency waves.* It is typically used in data transmission application, because it works for long distances and in vacuum, with a frequency that goes from 20 kHz up to 300 GHz. It is also used in some power transfer application, such as in the microwave oven, RF heating, and welding machines.
2. *Optical link.* It is characterized by a light source as a transmitter, and a light sensitive device as a receiver. It works in the ultraviolet, visible, and infrared regions of the electromagnetic frequency spectrum. It can be used to transfer data, either using a LED or with a high amount of power over long distances, as in the case of the sun or power laser diodes.
3. *Ultrasound.* It is used when there is a source of both potential and kinetic energy, that can be transformed in electrical energy and vice versa, via piezoelectric crystals. The operating frequency is over the human hearing limit ( $\approx 20$  kHz), and goes up to several MHz. It can also be used in the vacuum for long distances. Typical applications are power data transmission, non-destructive testing, remote sensing, and navigation systems. Recently it has also been used in higher power applications, such as medical devices and consumer electronics.
4. *Capacitive power transfer.* It works in combination with a time-varying electric field between two capacitor's electrodes, of which one is the Tx, and the other is the Rx. The power transfer is limited by the electrodes area and by the minimum distance between them. It has been used generally in low power applications, but it can also be used in combination with resonant coupling, for increasing the amount of power transferred and the efficiency.

5. *Electromagnetic power transfer.* It works in combination with a time-varying magnetic field. A transmitter coil conducts a time-varying current and, according to Ampere's law, it generates a magnetic field. Then, as stated in [5], according to Faraday's law, the time-varying magnetic field links to a receiver coil, inducing a voltage that makes a current flow. The electromagnetic power transfer could happen between either tightly coupled or loosely coupled coils.

In case of tightly coupled coils, the coupling factor  $k$  is close to unity, and the efficiency of the power transfer is high. An example of tightly coupled coils is the power transformer.

On the other hand, in case of loosely coupled coils,  $k$  is lower. As explained in [4], typically  $k$  has value between 0.05 and 0.5. In case of loosely coupled coils, the *coupling* could be either *inductive* or *resonant*.

The *inductive coupling* uses the same principle as the magnetic coupling through a transformer. However, the power transfer and efficiency are lower because of the poor coupling factor. A typical application is the electric toothbrush, in which the power transfer efficiency does not matter. On the other hand, the *resonant coupling* tunes the transmitter and receiver circuits at the same frequency, combining capacitors with the main coils, which form resonant circuits. This way, both the amount of power that can be transferred and the efficiency increase. It is easier to understand the resonant coupling making an analogy with radio waves. As explained in [6], when a high-frequency AC voltage source is applied to an antenna, it works as Tx converting the AC voltage into electromagnetic waves, only if it is tuned to the same frequency  $f_0$  of the voltage source. Another antenna tuned to the same frequency, can work as Rx, converting the electromagnetic waves into AC voltage, and powering a load. The schematic of this radio system is shown in Figure 1.1. The WPT through resonant coupling works similarly to the radio transmission, with the only difference that the amount of electric power received is close to the transmitted one.

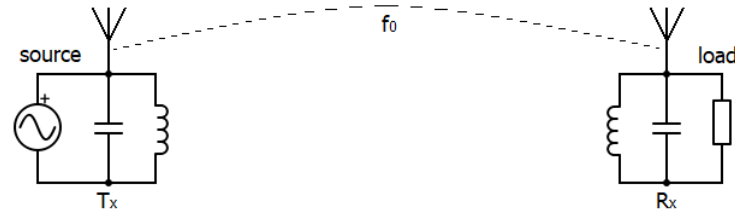


Figure 1.1: The overall e-bike WPT charging system resembles radio waves transmission, where the radio is tuned to the preferred station.

The subject of this thesis is an e-bike WPT charging system, using electromagnetic power transfer with resonant coupling. The WPT works through two coupled ferromagnetic coils with compensation capacitors. In particular, this thesis focuses on the control of the inverter of the e-bike WPT charging system. Chapter 1 is the introduction, and it gives some background on the WPT. Chapter 2 defines the problem treated in this project, explaining the whole e-bike WPT charging system with its goals and constraints. Chapter 3 analyses both the inductive and the resonant coupling, including the possible compensation networks. Chapter 4 discusses power electronics topologies for both the primary and the secondary converters. Chapter 5 compares the S-S and LCC compensation networks for the e-bike WPT charging system. Chapter 6 presents control strategies for the inner and outer control loops. Chapter 7 discusses the existing communication standards for WPT, focusing in detail on the Qi specification from the Wireless Power Consortium. Chapter 8 explains the design of the inner control loop for the primary inverter. Chapter 9 consists of the theoretical model validation with measurements on the set-up. Finally, Chapter 10 contains the conclusions on the e-bike WPT charging system, and recommendations for future research on the topic.

## Problem Definition

This Chapter explains the characteristics of the e-bike WPT charging system. Firstly, the problem of this project is defined and explained in Section 2.1. Secondly, the system constraints and goals are defined in Section 2.2. Finally, the methodology used is presented in Section 2.3.

### 2.1. The e-bike WPT charging system

The e-bike WPT charging system is composed of two main subsystems: the transmitter and the receiver. The transmitter, also called primary circuit, is located under a tile in the pavement. The receiver, also called secondary circuit, is located on the e-bike. The transmitter powers the receiver, such that it can charge the e-bike's battery. The actual power transfer happens through two loosely coupled ferromagnetic coils, of which one is part of the primary circuit, and the other one is part of the secondary circuit. In combination with these coils, compensation capacitors are needed for enhancing the transfer of real power. The schematic of the e-bike WPT charging system is shown in Figure 2.1.

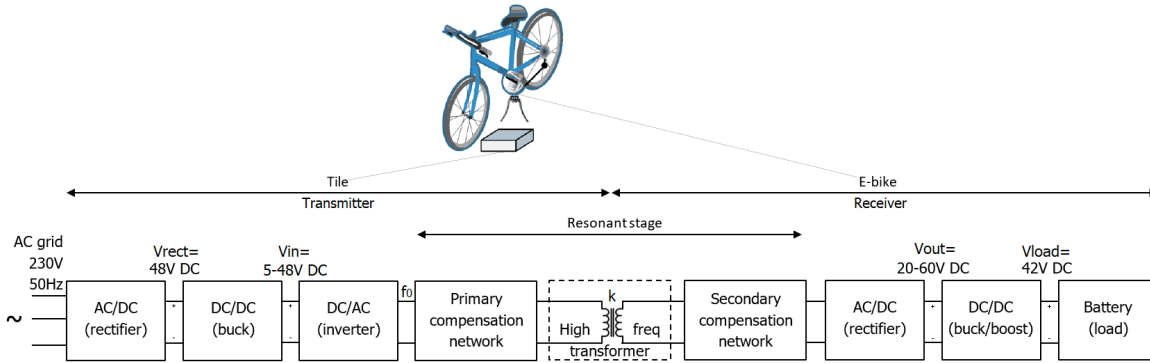


Figure 2.1: Schematic of the e-bike WPT charging system.

The transmitter is powered from the 50Hz AC grid. The grid voltage is rectified to  $V_{rect} = 48\text{ V}$  DC, and then stepped down through a DC/DC buck converter, such that at the input of the primary inverter there is  $V_{in} = 5\text{--}48\text{ V}$  DC. The primary inverter powers the primary coils at the high frequency  $f_0$ . The working cycle of the system starts when the bicycle is parked on the tile, the two coils become coupled, and the secondary circuit rectifies the received AC, charging the e-bike battery. Between the rectification stage and the battery, there is a DC/DC buck/boost converter, such that the variable rectified voltage  $V_{out}$  can be regulated, making the voltage across the battery  $V_{load}$  constant. Moreover, since the cyclist has some freedom in placing the bicycle on the charging tile, the magnetic coupling shows different behavior depending on the position and on the coils' alignment. After detecting the bicycle placement, the optimum operation point is automatically tracked by the inner control loop. The power communication between the e-bike and the tile takes place in the outer control loop, not conflicting with the inner control loop. The regulation of the rectified voltage  $V_{out}$ , with the buck/boost

converter, is done through the load voltage control loop. The e-bike WPT charging system with the inner, outer and load voltage control loops is shown in Figure 2.2.

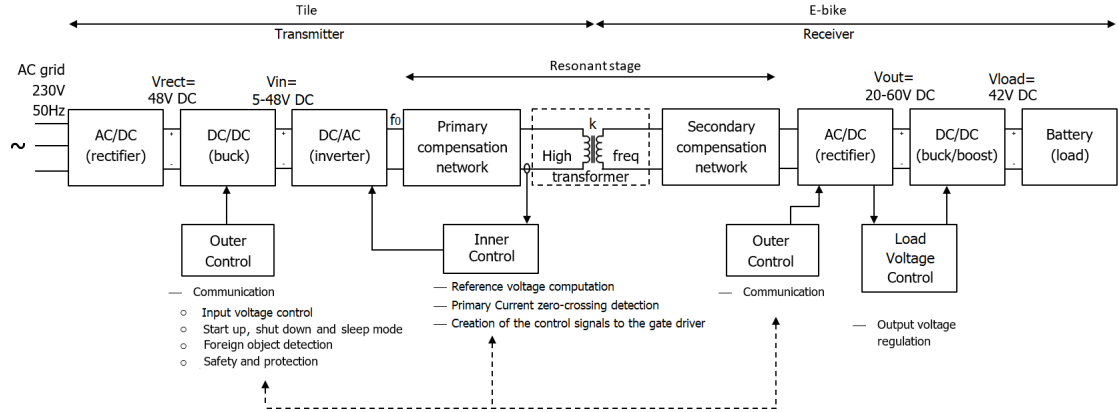


Figure 2.2: Schematic of the e-bike WPT charging system, including the control loops.

## 2.2. System constraints and goals

The entire e-bike WPT charging system in Figure 2.2 must be compliant to specific constraints and goals, which are summarized in Table 2.1 and 2.2, respectively. The constraints were already defined in former projects about the topic, and the goals have been defined at the beginning of this project. The goals concern the operation and the performance of the e-bike WPT charging system.

Table 2.1: Constraints of the e-bike WPT charging system.

Parameter	Value (Unit)
$f_0$	100 kHz
$V_{in}$	48 V DC
$V_{out}$	20-60 V
$V_{out,nom}$	42 V DC
$I_{out,nom}$	5 A
$P_{trans}$	200 W
$k_{max}$	0.25

Table 2.2: Goals of the e-bike WPT charging system.

<b>Efficiency and Power Factor (PF)</b>
Unity PF for maximizing the power transfer.
Maximize the power transfer efficiency at each coupling factor, choosing the most suitable inverter topology and compensation network.
Minimize the inverter and rectifier losses.
<b>Operation</b>
Automatic adjustment of the operating point using the inner control loop.
Implementation of the outer control loop for the communication between the transmitter and receiver.
Suitable start up and shut down strategy.
<b>Safety and protections</b>
Overvoltage and overcurrent protection.
Foreign object detection.
Sleep-mode/standby option.

## 2.3. Methodology

The methodology approach used in this project can be divided into three phases.

1. The literature research is executed to get a deep insight into the already-existing research on the WPT charging. This survey covers compensation networks, inverter topology selection, control methods and power communication standards. A prototype of the e-bike WPT charging system is already existing from a previous project, and it is used as starting point and its structure is shown in Figure 2.3. It needs to be noticed that the prototype in Figure 2.3 is just a proof of concept of the complete e-bike WPT charging system shown in Figure 2.2. The prototype is used to validate the theoretical models, and it is not the complete e-bike WPT charging system. The blocks covered by the literature research are pointed out by both the double-green and the dashed-red lines in Figure 2.4.
2. Only the blocks marked with the double-green lines in Figure 2.4 have been designed and implemented, which are the primary compensation network and the inner control loop. Therefore, the outer control loop, the protections, the foreign object detection and the DC/DC converters are not implemented in this project.
3. The primary compensation network and the inner control loop are built and used in combination with the already existing setup in Figure 2.3. The resulting prototype is shown in Figure 2.5. Finally, the measurements from the prototype are compared with the theoretical results, such that the equivalent-circuit model can be validated.

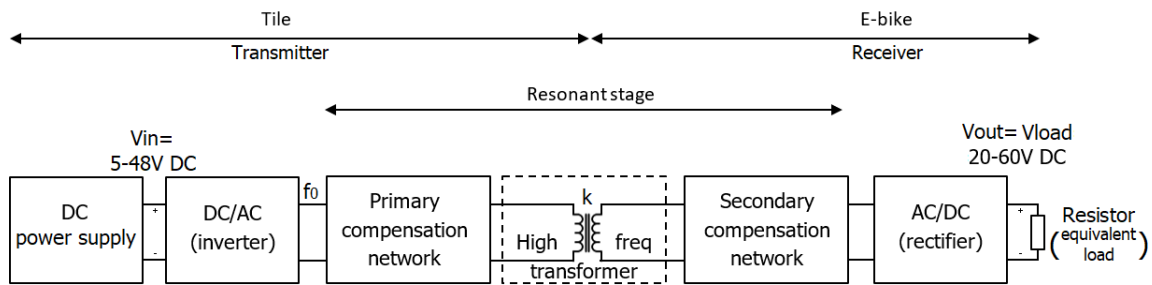


Figure 2.3: Prototype of the e-bike WPT charging system, already existing from previous projects.

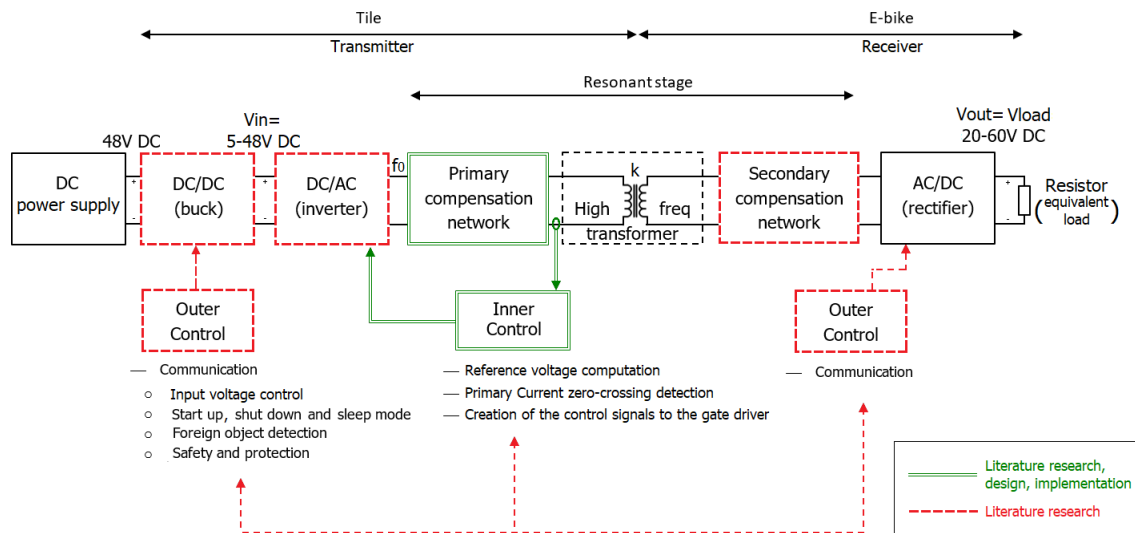


Figure 2.4: Schematic of the e-bike WPT charging system, starting from the already existing prototype. The red-dashed-line blocks are covered by literature research only, and the green-double-line blocks are covered by the literature research, design and implementation.

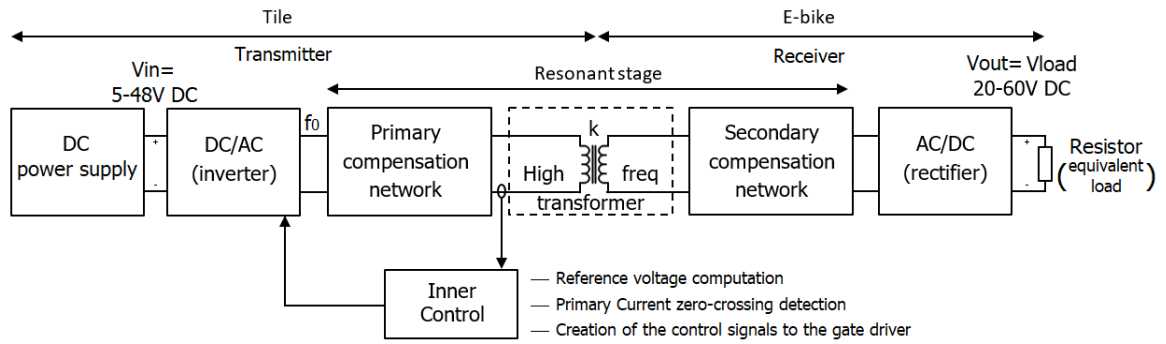


Figure 2.5: Final prototype of the e-bike WPT charging system, starting from the one in Figure 2.3. It includes the two main contributions of this project: the primary compensation network and the inner control loop.

# 3

## Inductive and resonant coupling

In this Chapter, both the inductive and resonant couplings between the primary and secondary coil are discussed. Firstly, the inductive coupling is presented in Section 3.1. After this, resonant compensation methods are discussed in Section 3.2, and the most suitable one for the e-bike WPT charging system is chosen. The chosen resonant compensation network is analyzed in detail in Section 3.3, which in turn is divided into five subsections:

1. the equivalent circuit and its equations are found, such that a theoretical model is realized,
2. the theoretical model is validated with results for circuital simulations,
3. the phenomenon of the bifurcation is defined and explained,
4. considerations about power factor and efficiency are presented and
5. the results of this analysis are discussed.

Finally, a variation of the chosen compensation network is discussed and explained in Section 3.4.

### 3.1. Inductive coupling

The WPT is possible through two coupled coils, under the name of inductive coupling as explained in the Introduction. According to Ampere's law, a current flowing in a coil produces a magnetic field and, for Faraday's law, part of this field links to a second coil inducing a voltage at its terminals. This induced voltage causes a current flowing in the second coil, realizing the WPT. The described system is a transformer, of which equivalent circuit is reported in Figure 3.1.

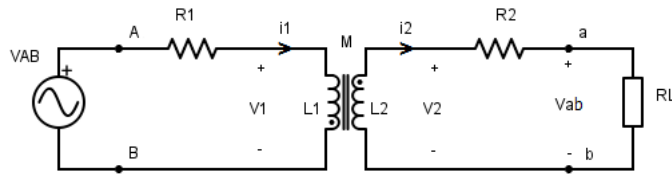


Figure 3.1: Basic transformer equivalent circuit.

$V_{AB}$  is the AC input voltage connected to the primary coil,  $R_1$  and  $L_1$  are the resistance and the inductance of the primary coil,  $R_2$  and  $L_2$  are the resistance and the inductance of the secondary coil and  $R_L$  is the load resistance. Moreover, the mutual inductance  $M$  between the two coils is defined as

$$M = k\sqrt{L_1 L_2} \quad (3.1)$$

where  $k$  is the coupling factor between the primary and secondary coil.

Another important parameter is the input impedance  $Z_{in}$  in (3.2), that is the equivalent impedance seen

from the input source  $V_{AB}$ , such that the circuit in Figure 3.1 can be redrawn as in Figure 3.2.

$$Z_{in} = \frac{M^2 \omega^2}{R_2 + R_L + j\omega L_2} + R_1 + j\omega L_1 \quad (3.2)$$

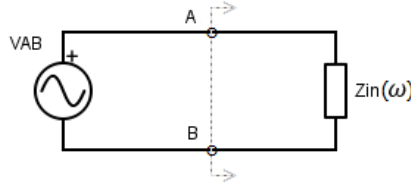


Figure 3.2: Equivalent input impedance  $Z_{in}$  seen from the input voltage  $V_{AB}$ .

The WPT system has to transfer real power from the primary to the secondary circuit for charging the e-bike battery. This means that the ratio between the real and the apparent power, commonly called Power Factor (PF), has to be as close as possible to unity. Considering the equivalent circuit in Figure 3.2, having the PF=1 implies the imaginary part of  $Z_{in}$  to be equal to zero. However, according to (3.2) it is clear that at the typical operating frequency ( $\approx 100$  kHz) the inductive component of  $Z_{in}$  would be predominant, making the PF approach zero. Therefore, it is necessary to compensate the inductive circuits in Figure 3.1 with capacitors for having a real power transfer.

### 3.2. Resonant coupling

Since (3.2) shows that  $Z_{in}$  is inductive at the typical operating frequency, adding a capacitor at both the primary and at the secondary circuits can make  $Z_{in}$  resistive for achieving the transfer of real power. These capacitors are called compensation capacitors, and the coupling between the two coils becomes then resonant.

Four combinations of compensation networks are possible, placing the capacitor either in series or parallel to the coils, as shown in Figure 3.3.

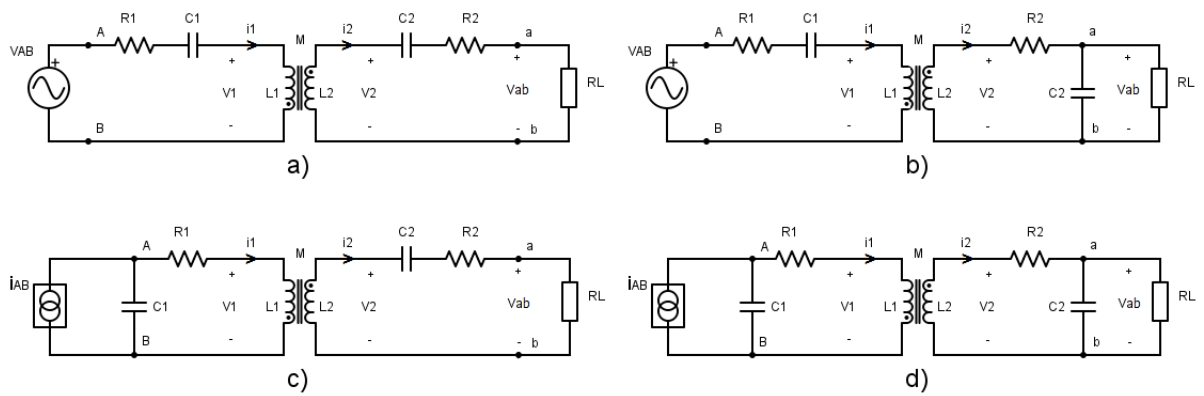


Figure 3.3: Four possible compensation networks for the primary and secondary coils. a) Series-Series (S-S), b) Series-Parallel (S-P), c) Parallel-Series (P-S), and d) Parallel-Parallel (P-P).

In all the compensation networks, the secondary capacitor  $C_2$  is selected as in (3.3), such that it is resonating with the secondary coil inductance  $L_2$ , for having a unity PF at the secondary side, and enhancing the power transferred. The resonant frequency at which the secondary circuit is resonating is  $f_0$ .

$$C_2 = \frac{1}{\omega_0^2 L_2} = \frac{1}{4\pi^2 f_0^2 L_2} \quad (3.3)$$

On the other hand, the primary capacitor  $C_1$  is chosen such that the imaginary part of the equivalent input impedance  $Z_{in}$  in Figure 3.2 is zero at the same resonant frequency  $f_0$ . Table 3.1 shows the equations



for finding the primary capacitor  $C_1$  for each compensation network in Figure 3.3. The evaluation of these equations is detailed in Appendix A, and it agrees with [7].

Table 3.1: Primary compensation capacitance  $C_1$  for each possible compensation network.

Compensation network	$C_1$	$C_1$ dependent on
S-S	$\frac{L_2 C_2}{L_1}$	-
S-P	$\frac{L_2^2 C_2}{L_1 L_2 - M^2}$	$M$
P-S	$\frac{L_1 L_2^2 C_2 R_L^2}{M^4 + L_1 L_2 R_L^2}$	$M$ and $R_L$
P-P	$\frac{L_2^2 (L_1 L_2 - M^2) C_2}{(L_1 L_2 - M^2)^2 + M^4 R_L^2 L_2 C_2}$	$M$ and $R_L$

According to Table 3.1, the S-S compensation network is the only one in which the primary compensation capacitor  $C_1$  is independent of both the mutual inductance  $M$  and the resistive load  $R_L$ . Since in the e-bike WPT charging system the secondary coil position is not fixed, and the equivalent load is changing while the battery is charging, it is important that the circuit parameters are independent of both  $M$  and  $R_L$ . Therefore, the S-S compensation network is the most suitable one, and it is discussed in detail in the next section.

### 3.3. Series-Series compensation network

#### 3.3.1. Equivalent circuit and equations

The compensation of the reactive power in a resonant converter is necessary for having both a real power transfer and a unity power factor (PF). For achieving that when  $k$  and  $R_L$  are not fixed, the best compensation network is the one with a capacitor in series with the coil at both primary and secondary circuit, as shown in Figure 3.4.

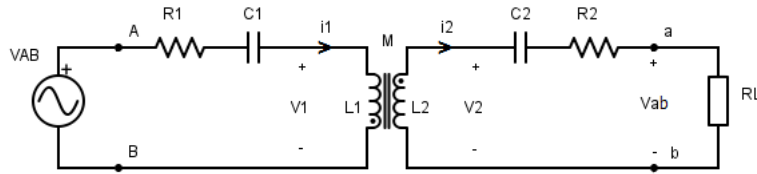


Figure 3.4: Equivalent circuit of the S-S compensation network.

The resonant frequency is tuned as in (3.3), making a unity PF at the secondary circuit for enhancing the power transfer. Moreover, according to Table 3.1, the primary capacitor  $C_1$  is chosen as

$$C_1 = \frac{L_2 C_2}{L_1} \quad (3.4)$$

such that

$$f_0 = \frac{1}{2\pi\sqrt{L_1 C_1}} = \frac{1}{2\pi\sqrt{L_2 C_2}} \quad (3.5)$$

Therefore, the input impedance  $Z_{in}$  in (3.6) is purely resistive at the chosen  $f_0$ .

$$Z_{in} = \frac{M^2 \omega^2}{R_2 + R_L + j\omega L_2 + \frac{1}{j\omega C_2}} + R_1 + j\omega L_1 + \frac{1}{j\omega C_1} \quad (3.6)$$

Two sets of equations can be written starting from the equivalent circuit in Figure 3.4. The variables in the circuit are sinusoid, and the phasor convention is used. The phase angle of the input voltage  $V_{AB}$  is considered to be zero, and it is taken as the reference for all the other phasors in the circuit.

*Kirchhoff's Voltage Law (KVL):*

$$V_{AB} = (R_1 + j\omega L_1 + \frac{1}{j\omega C_1})I_1 + j\omega M I_2 \quad (3.7)$$

$$0 = j\omega M I_1 + (R_2 + R_L + j\omega L_2 + \frac{1}{j\omega C_2})I_2 \quad (3.8)$$

*Primary and secondary voltage:*

$$V_1 = V_{L1} = V_{AB} - (R_1 + \frac{1}{j\omega C_1})I_1 = j\omega L_1 I_1 + j\omega M I_2 \quad (3.9)$$

$$V_2 = -V_{L2} = (R_2 + R_L + \frac{1}{j\omega C_2})I_2 = -(j\omega M I_1 + j\omega L_2 I_2) \quad (3.10)$$

According to [8], the maximum power transferred that the system can handle  $P_{max}$  can be calculated considering the open-circuit voltage  $V_{oc}$  and the short-circuit current  $I_{sc}$  of the circuit in Figure 3.4.

$$V_{oc} = j\omega M I_1 \quad (3.11)$$

$$I_{sc} = \frac{M}{L_2} I_1 \quad (3.12)$$

$$S_{max} = V_{oc,max} I_{sc,max}^* = j\omega M_{max} I_{1,max} \frac{M_{max}}{L_2} I_{1,max} \quad (3.13)$$

$$P_{max} = S_{max} \times Q_{max} = \omega \frac{M_{max}^2 I_{1,max}^2}{L_2} \cdot Q_{2,max} = \frac{\omega^2 M_{max}^2 I_{1,max}^2}{R_{L,min}} = \frac{\omega^2 k_{max}^2 L_1 L_2 I_{1,max}^2}{R_{L,min}} \quad (3.14)$$

where  $Q_2 = \frac{\omega_0 L_2}{R_L}$  is the quality factor of the secondary circuit. From (3.14) it is clear that the power transferred to the secondary is directly proportional to  $k^2$  and inversely proportional to  $R_L$ .

The rated power of the system can be set designing the coils' geometry, air gap, winding and inductance. At the beginning of this project, the primary and secondary coils were already designed and optimized. Therefore, the power level,  $k_{max}$  and  $f_0$  are already fixed as reported in Table 2.1.

### 3.3.2. Analysis of the model

Starting from (3.7), (3.8), (3.9) and (3.10), the primary and secondary voltages and currents are analyzed in the frequency domain, varying the load resistance  $R_L$ . These equations are plotted with a numerical equation solver, at the circuit conditions found in the former project about the e-bike WPT charging system [9]. The value of each parameter in the circuit is reported in Table 3.2. Moreover, these results are compared with circuit simulations at the same conditions.

Table 3.2: Value of the parameters used in the circuit analysis.

Parameter	Value (Unit)
$f_0$	100 kHz
$V_{AB}$	48 V
$R_1$	13 m $\Omega$
$L_1$	55.6 $\mu$ H
$C_1$	45.5 nF
$R_2$	24 m $\Omega$
$L_2$	48.6 $\mu$ H
$C_2$	52 nF
$R_L$	1, 5, 10, 15, 30, 100 $\Omega$
$k$	0.25

The results plotted with the numerical equation solver match the results from the circuit simulation, with the accuracy discussed in the second Section of Notation. This confirms that an accurate model has been built on the correct equations ((3.7), (3.8), (3.9) and (3.10)), which will be used for the further analysis.

Both the absolute peak value and the phase angle of the phasors of the equivalent circuit of Figure 3.4 are analyzed. These phasors are: the primary voltage  $V_1$ , the primary current  $I_1$ , the secondary voltage  $V_2$ , the secondary current  $I_2$ , the output voltage  $V_{ab}$  across  $R_L$  and the input impedance  $Z_{in}$  which are plotted in Figure 3.5, 3.6, 3.7, 3.8, 3.9 and 3.10, respectively.

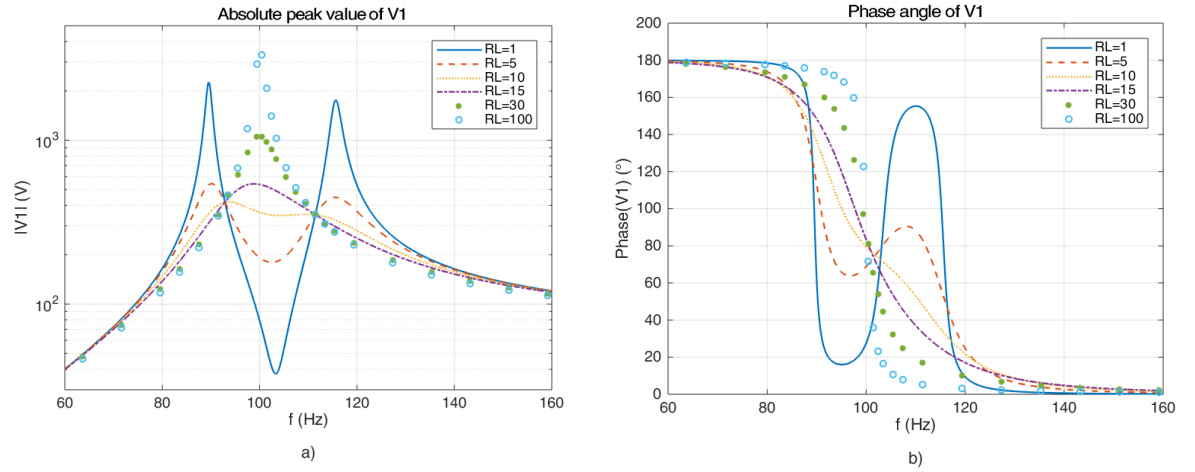


Figure 3.5: a) Absolute peak value and b) phase angle of the voltage  $V_1$  across the primary inductor  $L_1$  in function of the operating frequency, at different load values, computed from (3.9).

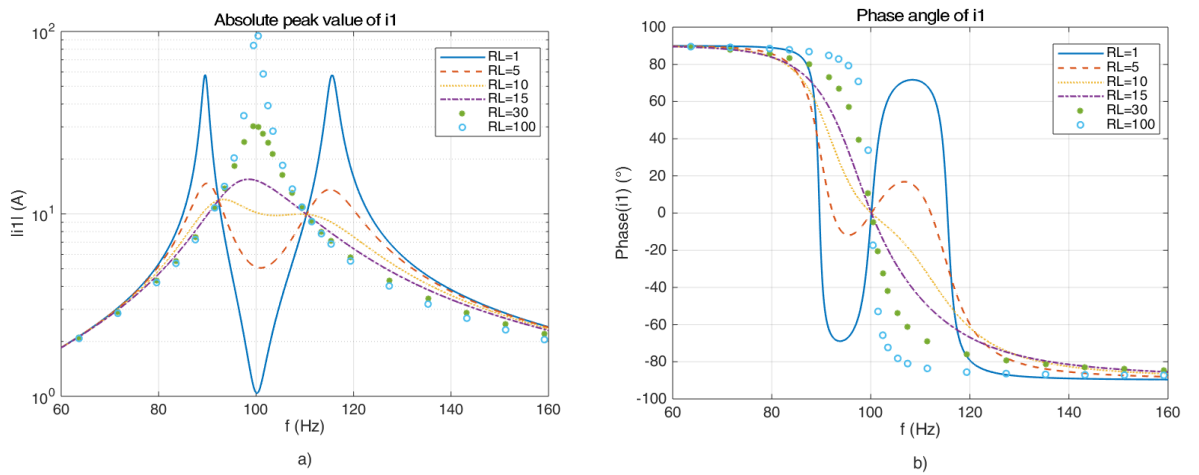


Figure 3.6: a) Absolute peak value and b) phase angle of the primary current  $I_1$  in function of the operating frequency, at different load values, computed from (3.7) and (3.8).

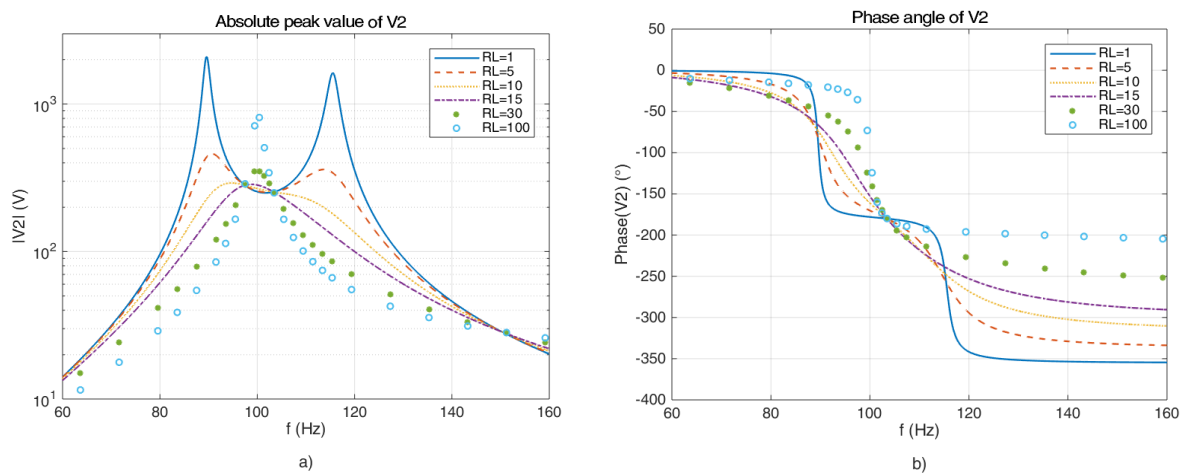


Figure 3.7: a) Absolute peak value and b) phase angle of the voltage  $V_2$  across the secondary inductor  $L_2$  in function of the operating frequency, at different load values, computed from (3.10).

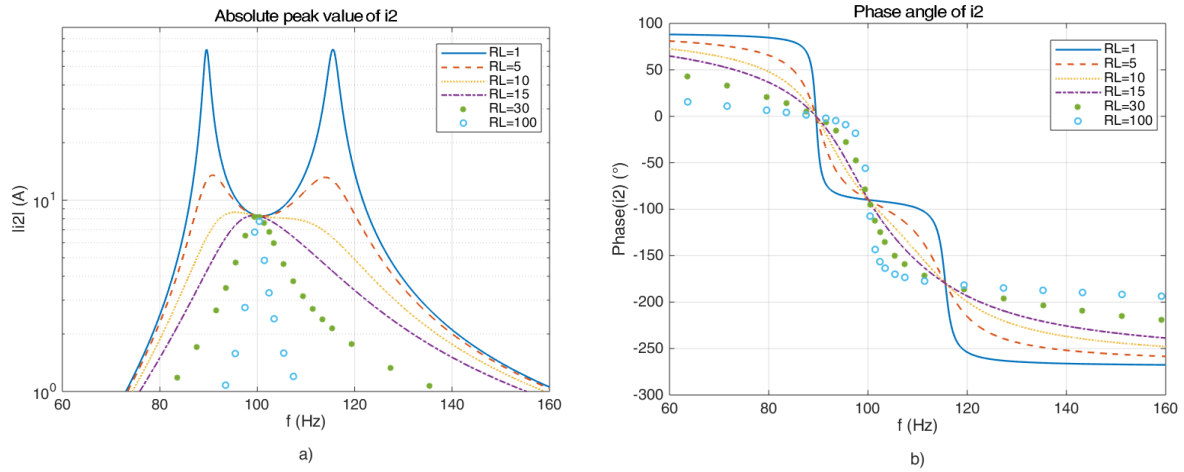


Figure 3.8: a) Absolute peak value and b) phase angle of the secondary current  $I_2$  in function of the operating frequency, at different load values, computed from (3.7) and (3.8).

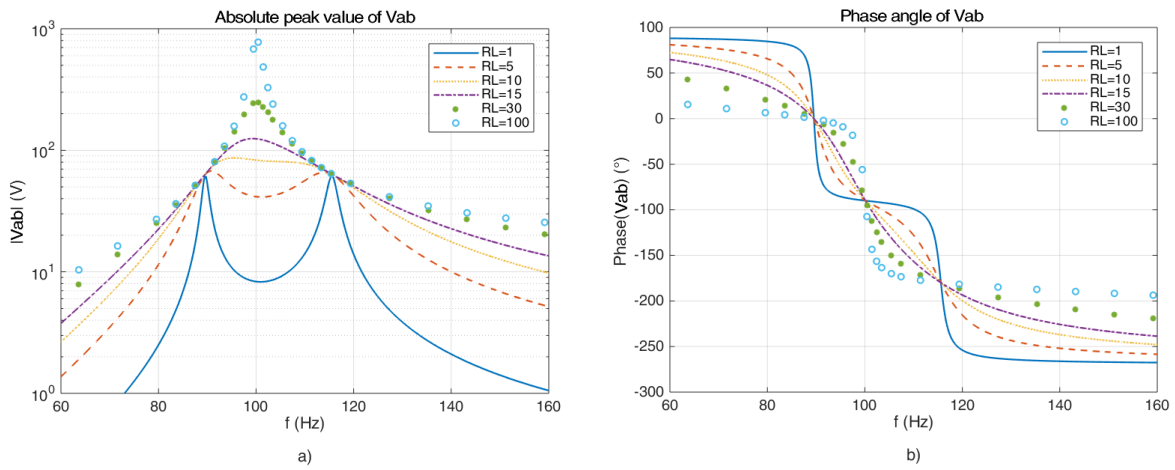


Figure 3.9: a) Absolute peak value and b) phase angle of the output voltage  $V_{ab}$  across the load resistor  $RL$  in function of the operating frequency, at different load values, computed from (3.7) and (3.8).

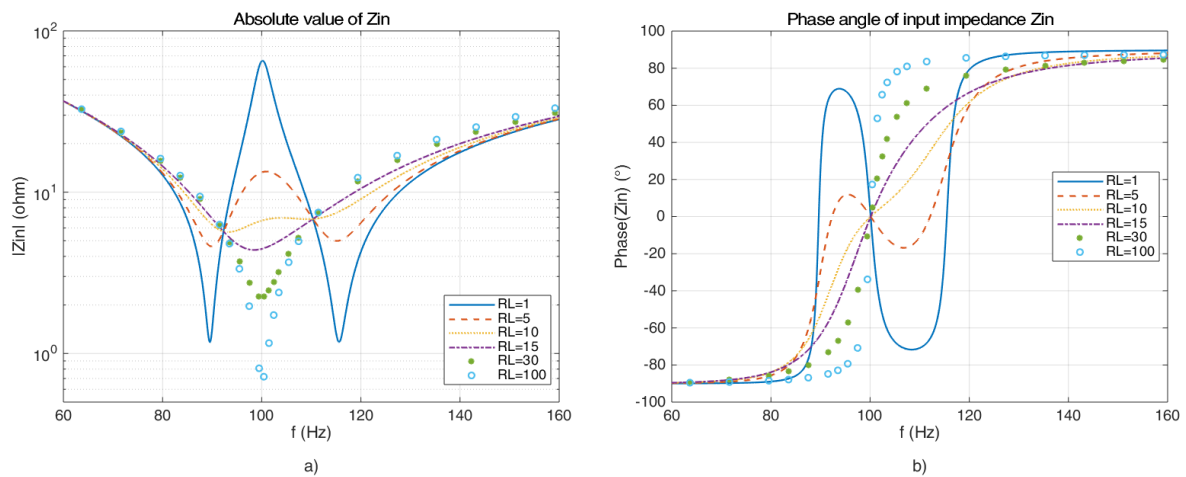


Figure 3.10: a) Absolute value and b) phase angle of the equivalent input impedance  $Z_{in}$  in function of the operating frequency, at different load values, computed from (3.6).

### 3.3.3. The bifurcation phenomenon

All the plotted waveforms in Section 3.3.2 show that they are highly dependent on the value of the resistive load  $R_L$ . In particular, their absolute value has one maximum centered on the chosen  $f_0$  for high values of  $R_L$ . On the other hand, for low values of  $R_L$ , their absolute value has two peaks in correspondence of two side frequencies.

This load-dependent behavior of the system is also visible in the input impedance  $Z_{in}$ . For having the maximum real power transfer and a unity power factor, the system must be designed in such a way that both the absolute value and the phase angle of  $Z_{in}$  are as close as possible to zero at the resonant frequency. Figure 3.10 a) shows that the absolute value of  $Z_{in}$  has a high peak in correspondence of the chosen  $f_0$  and its minimum at two side frequencies for low values of  $R_L$ . As the load  $R_L$  increases, the absolute value of  $Z_{in}$  has just one minimum point close to zero at  $f_0$ , showing a capacitive behavior for lower frequencies (negative slope) and an inductive behavior (positive slope) for higher frequencies. Figure 3.10 b) shows that the phase angle of  $Z_{in}$  is zero at the chosen  $f_0$  for any value of  $R_L$ . However, for high values of  $R_L$  the phase angle is zero just once at  $f_0$  but, as the load decreases, the phase angle is zero in correspondence of three values of frequency:  $f_0$  and two at its sides.

The phenomenon according to which the phase angle of  $Z_{in}$  is zero also for other frequencies, apart from the chosen  $f_0$ , is called bifurcation. The minimum value of  $R_L$  that allows the system to have a bifurcation-free operation is found making some consideration on  $Z_{in}$ . The imaginary part of  $Z_{in}$  has to be zero to make sure that the phase angle is zero just once at the resonant frequency.  $Z_{in}$  in (3.6) can be rewritten separating the real part from the imaginary part for a better understanding.

$$Z_{in} = R_1 + \underbrace{\frac{\omega^4 C_2^2 M^2 (R_2 + R_L)}{(\omega C_2)^2 (R_2 + R_L)^2 + (\omega^2 C_2 L_2)^2}}_{Real(Z_{in})} + j \underbrace{\left[ \omega L_1 - \frac{1}{\omega C_1} - \frac{\omega^3 M^2 C_2 (\omega^2 L_2 C_2 - 1)}{(\omega C_2)^2 (R_2 + R_L)^2 + (\omega^2 C_2 L_2)^2} \right]}_{Imag(Z_{in})} \quad (3.15)$$

The condition for a bifurcation-free operation can be expressed as

$$Imag(Z_{in}) = 0 \rightarrow \left[ \omega L_1 - \frac{1}{\omega C_1} - \frac{\omega^3 M^2 C_2 (\omega^2 L_2 C_2 - 1)}{(\omega C_2)^2 (R_2 + R_L)^2 + (\omega^2 C_2 L_2)^2} \right] = 0 \quad (3.16)$$

Then, introducing the normalized frequency  $u^2 = \frac{\omega^2}{\omega_0^2} = \omega^2 L_1 C_1 = \omega^2 L_2 C_2$  as explained in [7], (3.16) can be simplified as

$$(u^2 - 1)[(u^2 - 1)^2 + (\omega C_2)^2 (R_2 + R_L)^2 - \omega^4 M^2 C_1 C_2] = 0 \quad (3.17)$$

(3.17) has at most three real roots. The first one corresponds to the resonant frequency  $\omega_0 = 2\pi f_0$  and, because it should be the only solution, the other two must be imposed to be complex. This means that the discriminant  $\Delta$  of the terms of (3.17) in the square-brackets have to be negative. Neglecting  $R_2$  and assuming  $R_L = \frac{\omega_0 L_2}{Q_2}$  where  $Q_2$  is the secondary quality factor and  $M = k\sqrt{L_1 L_2}$ , the discriminant can be written as

$$\Delta = \left( 2 - \frac{1}{Q_2^2} \right)^2 - 4(1 - k^2) < 0 \quad (3.18)$$

The maximum secondary quality factor  $Q_2$  and minimum the load resistance  $R_L$ , that make (3.18) true, are shown in (3.19), as also mentioned in [7].

$$Q_2 < \sqrt{\frac{1}{2(1 - \sqrt{1 - k^2})}} \rightarrow R_L > \frac{\omega_0 L_2}{\sqrt{\frac{1}{2(1 - \sqrt{1 - k^2})}}} \quad (3.19)$$

Table 3.3 shows the minimum values of  $R_L$  ( $R_{L,min}$ ), at which a bifurcation-free operation is achieved. For evaluating these critical load values,  $f_0$  and  $L_2$  are chosen according to Table 3.2. On the other hand,  $k$  is considered at both its minimum value 0.1 and its maximum value 0.25.

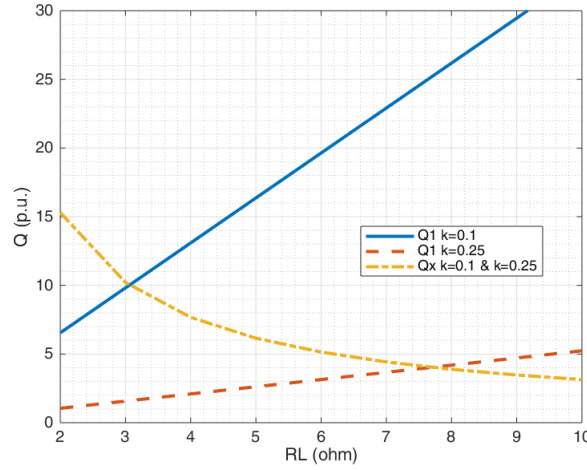
Table 3.3: Minimum values of  $R_L$  for a bifurcation-free operation at  $k = 0.1$  and  $k = 0.25$ .

$k$	$R_{L,min}$
0.1	$3.06 \Omega$
0.25	$7.7 \Omega$

Another critical condition for a bifurcation-free operation is found in [10] and [4]. In case of S-S compensation can be written as

$$Q_1 = \frac{L_1 R_L}{\omega_0 M^2} > \frac{4Q_2^3}{4Q_2^2 - 1} = Q_x \quad (3.20)$$

Similarly as in [7], in also this case the critical condition is found by setting the imaginary part of  $Z_{in}$  in (3.15) equal to zero. However, the condition is now not only written in function of the secondary quality factor  $Q_2$  but also of the primary quality factor  $Q_1$ . From (3.20),  $R_{L,min}$  that makes  $Q_1$  greater than  $Q_x$  can be found, and that value is the boundary of the bifurcation-free operation.  $Q_1$  and  $Q_x$  are plotted in Figure 3.11 in function of  $R_L$ , and for  $k=0.1, 0.25$ .

Figure 3.11: Plot of  $Q_1$  and  $Q_x$  for  $k=0.1, 0.25$ .

From the plots of Figure 3.11 it is possible to see that, according to (3.20), the bifurcation boundary is at  $R_{L,min} \sim 3.1 \Omega$  for  $k=0.1$ , and at  $R_{L,min} \sim 7.8 \Omega$  for  $k=0.25$ .

These conditions agree with the ones in Table 3.3 and so, the condition for having a bifurcation free operation in [7] and in [10] are equivalent.

Therefore,  $R_{L,min}$  that gives a bifurcation free-operation drops when the coupling between the coils worsens.

### 3.3.4. Efficiency and Power Factor calculation

From the analysis of the primary and secondary voltages and currents, the voltage gain  $G_v$  and current gain  $G_i$  can be computed as in (3.21), as stated in [11]. These two quantities are plotted in Figure 3.12 a) and b).

$$G_i = \frac{|I_2|}{|I_1|}, \quad G_v = \frac{|V_{ab}|}{|V_{AB}|} = \frac{R_L |I_2|}{|V_{AB}|} \quad (3.21)$$

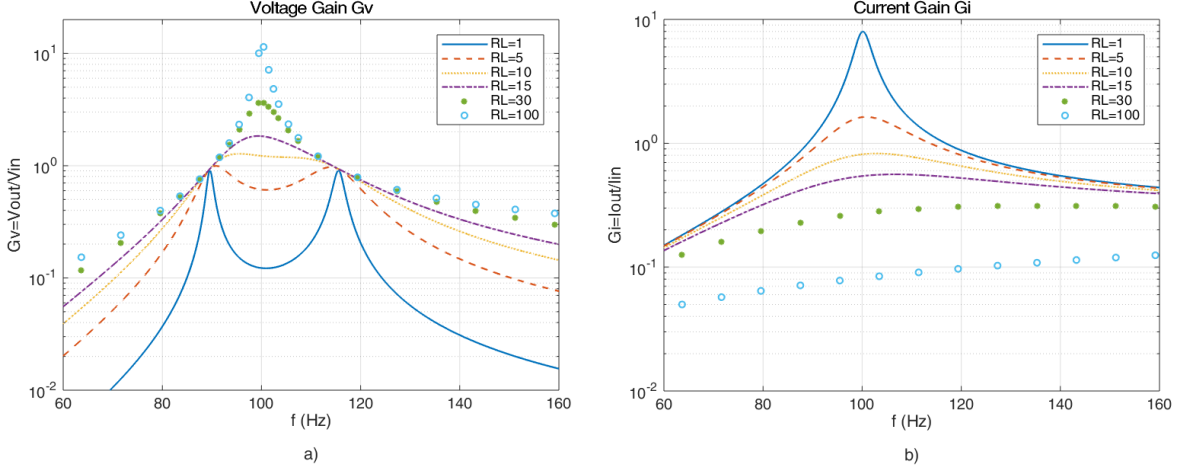


Figure 3.12: a) Voltage gain  $G_v$ , b) Current gain  $G_i$  at  $k=0.25$  for different values of  $R_L$ .

According to [11], the efficiency  $\eta$  of the wireless power transfer is

$$\eta_{AC} = \frac{|V_{ab}| |I_2|}{|V_{AB}| |I_1|} = \frac{R_L |I_2|^2}{|V_{AB}| |I_1|} = G_v G_i \quad (3.22)$$

Although the efficiency is an important parameter that has to be taken in account, the Power Factor (PF) is even more fundamental. The PF is the ratio between the real power and the apparent power in the equivalent circuit. In this wireless system the goal is to transfer as much real power as possible from the primary to the secondary circuit, because it represents the useful power for charging the bicycle battery. Considering the equivalent circuit in Figure 3.2, the PF can be easily found as

$$PF = \cos[\phi(Z_{in})] \quad (3.23)$$

where  $\phi(Z_{in})$  is the phase angle of  $Z_{in}$ .

The efficiency and the PF plots are shown in Figure 3.13 a) and b), respectively.

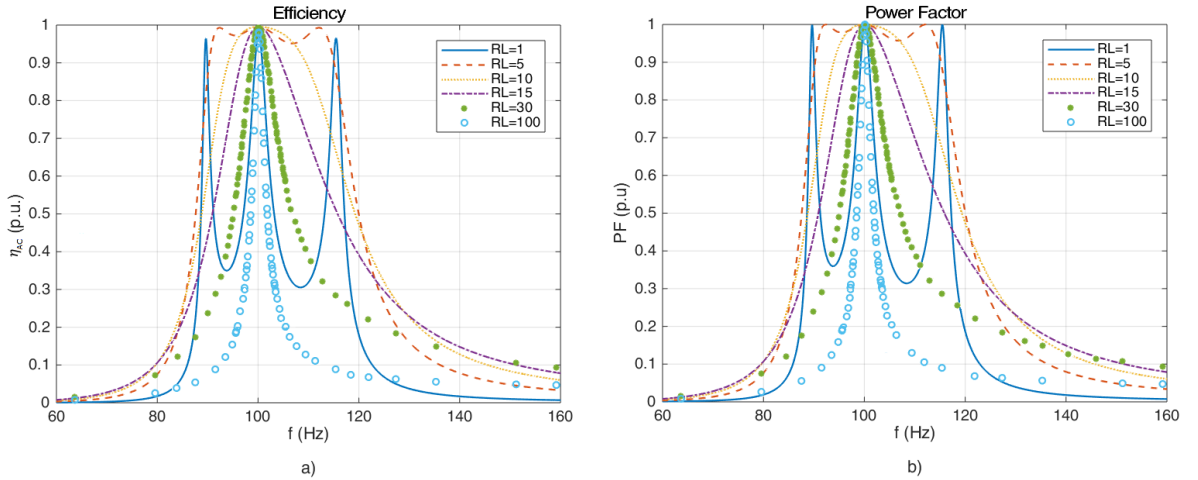


Figure 3.13: a) Efficiency p.u., b) Power factor (PF) of the wireless power transfer at  $k=0.25$  for different values of  $R_L$ .



### 3.3.5. Discussion of the results

In Section 3.3 the characteristics of the S-S compensation network for the e-bike WPT charging system are analyzed, and a consistent model from the equivalent circuit is built and verified via simulations. However, few considerations need to be pointed out.

Firstly, the AC analysis on the S-S compensation network in Figure 3.4 is done imposing as input voltage  $V_{AB}$  a sinusoidal source with an amplitude of  $\sqrt{2} \times 48$  V, which sends a frequency sweep from 10 kHz to 200 kHz. However, in case either a half-bridge or a full-bridge inverter is providing  $V_{AB}$ , the voltage source is not sinusoid, but it is a square wave. The AC analysis only takes into account the fundamental harmonic of  $V_{AB}$ , considering that it is the only parameter contributing to the power transfer. So, the analysis in Section 3.3 is a first harmonic approximation.

Secondly, the resistive load  $R_L$  in Figure 3.4 has AC voltage across it. However, in the real e-bike WPT charging system, there is a rectifier between the secondary resonant circuit and the load, such that it is supplied by DC voltage for charging the battery. Therefore, the dependence of the system on the variation of the load could be different in case of a DC load than the one observed in the analysis of Section 3.3. As an example, considering a diode-bridge rectifier, the equivalent  $R_L$  is going to be different because it also depends on the conduction of the diodes. Moreover, the diode-bridge distorts  $i_2$  making it not sinusoidal. The waveforms in the secondary circuit are shown in Figure 3.14 a) in case there is AC voltage across  $R_L$ , and in Figure 3.14 b) in case there is the diode-bridge rectifier.

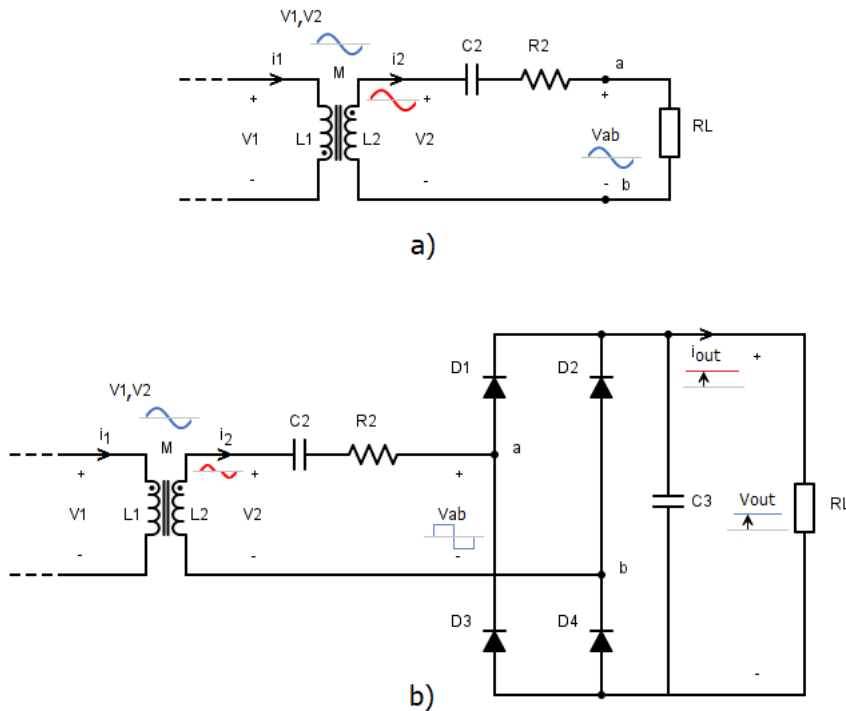


Figure 3.14: Secondary circuit: a) used for the theoretical model with only AC voltages and currents, b) of the e-bike WPT charging system, with a DC voltage across  $R_L$ .

The analysis of the basic S-S compensation network in Figure 3.14 a) is useful for understanding its main characteristics. A secondary circuit more coherent to the e-bike WPT charging system in Figure 3.14 b) is analyzed in Section 5.1.

### 3.4. Double-sided LCC compensation

The basic compensation networks are explained in Section 3.2 and, starting from them, these can be modified for realizing more complex compensations. As an example, starting from the S-S compensation network in Figure 3.4, two LC filters can be added to both the primary and the secondary circuits, as shown in Figure 3.15. These extra components are placed between the inverter output and the primary circuit, and between the secondary circuit and the rectifier.

Adding these two filters gives five main advantages. Firstly, the current through the primary coil  $L_1$  becomes constant, such that it can work at the maximum rated power without going into saturation. Secondly, the power level of the circuit can be easily influenced by changing the filter inductances  $L_{f1}$  and  $L_{f2}$ , without modifying the main coupled coils  $L_1$  and  $L_2$ . Thirdly, if the circuit is operating at the design frequency  $f_0$ , at both the primary and secondary circuits the voltages and current are in phase (PF=1). Fourthly, the secondary current is directly proportional to  $k$ . Therefore, the secondary circuit is intrinsically protected in case the coupling is low. Finally, assuming that an inverter powers the primary circuit, the zero voltage switching (ZVS) operation can be achieved simply by changing the secondary capacitor  $C_2$ . The first four advantages are explained in this Section, and the fifth one is explained in Section 4.3.1. This compensation network is called double-sided LCC compensation.

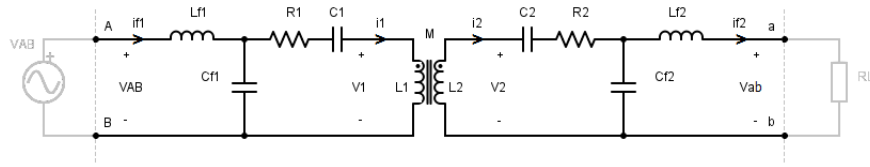


Figure 3.15: Equivalent circuit of the double-sided LCC compensation network.

As previously discussed, in the S-S compensation network, the resonant frequency  $f_0$  only depends on the primary and secondary circuit parameters, and it is independent of  $k$  and  $R_L$ . However, the primary current in the system is highly dependent on  $k$  and  $R_L$  making the control of the primary circuit difficult. In fact,  $i_1$  could reach high values because of the bifurcation phenomenon, that could easily make the primary coil saturate. Having  $i_1$  constant would considerably simplify the control of the system, this is possible by adding an LC filter before the primary S-S compensation. According to [4], the Norton equivalent circuit of the primary LC filter in Figure 3.16 shows that, at  $f = f_0$ , the circuit behaves as a current source. Therefore,  $i_1$  is independent from  $k$  and  $R_L$ .

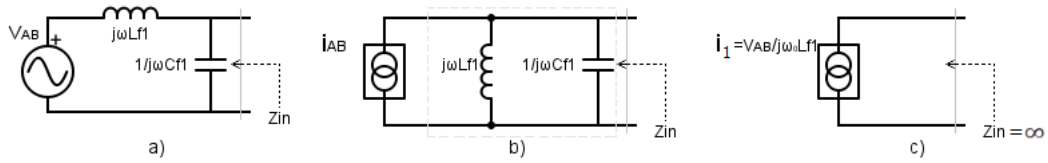


Figure 3.16: a) Primary LC filter. b) Norton equivalent circuit. c) Norton equivalent circuit at the resonant frequency  $f_0$ .

The whole system is designed to resonate at the chosen resonant frequency  $f_0$ . So, the LC filters' values need to be tuned to the same resonant frequency. As explained in [12], this can be achieved if the LC circuit parameters satisfy (3.24), (3.25), (3.26) and (3.27).

$$L_1 - L_{f1} = \frac{1}{\omega_0^2 C_1} \quad (3.24)$$

$$L_2 - L_{f2} = \frac{1}{\omega_0^2 C_2} \quad (3.25)$$

$$L_{f1} C_{f1} = \frac{1}{\omega_0^2} \quad (3.26)$$

$$L_{f2}C_{f2} = \frac{1}{\omega_0^2} \quad (3.27)$$

To achieve a real power transfer, the PF of both the primary and the secondary circuit must be equal to one. This means that at the primary circuit  $V_{AB}$  must be in phase with  $I_{L_{f2}}$  and at the secondary circuit  $V_{ab}$  must be in phase with  $I_{L_{f1}}$ .

It is possible to verify if the voltage and current at both the primary and secondary are in phase, analyzing the equivalent circuit through the principle of superposition. This consists in operating the circuit in Figure 3.15 in two configurations. Firstly, applying a voltage  $V_{AB}$  at the input and short-circuiting the output voltage  $V_{ab}$ . Secondly, applying a voltage  $V_{ab}$  at the output and short-circuiting the input voltage  $V_{AB}$ . The currents resulting from the two configurations are then summed, and the final results are

$$V_{AB} = V_{AB}/0^\circ \quad (3.28)$$

$$I_{L_{f1}} = \frac{k\sqrt{L_1L_2}V_{ab}}{\omega_0L_{f1}L_{f2}}/0^\circ \quad (3.29)$$

$$I_1 = \frac{V_{AB}}{\omega_0L_{f1}}/-90^\circ \quad (3.30)$$

$$V_{ab} = V_{ab}/-90^\circ \quad (3.31)$$

$$I_2 = \frac{V_{ab}}{\omega_0L_{f2}}/0^\circ \quad (3.32)$$

$$I_{L_{f2}} = \frac{k\sqrt{L_1L_2}V_{AB}}{\omega_0L_{f1}L_{f2}}/-90^\circ \quad (3.33)$$

The resulting (3.29), (3.30), (3.31), (3.32) and (3.33) have been verified through simulations of the circuit. The calculations that lead to these results are reported in Appendix B.

(3.28), (3.29), (3.31) and (3.33) show that the condition PF=1 is valid at both the primary and secondary circuit and this does not depend neither on  $k$  nor on  $R_L$ . On the other hand, (3.30) shows that the primary coil current  $I_1$  is constant because it depends on the inverter output voltage  $V_{AB}$ , on the resonant frequency  $\omega_0$  and on the primary filter inductance  $L_{f2}$ . So, the current rating of the primary coil can be set by choosing the proper value of  $L_{f2}$  and, since the current is constant, it can work at rated power. Moreover, (3.33) shows that the output current  $I_{L_{f2}}$  of the secondary compensation circuit depends on constant variables but it is directly proportional to the coupling factor  $k$ . So, the output current decreases as the misalignment of the coils increases and the maximum output current at the maximum coupling can be set choosing the proper values for  $L_{f1}$  and  $L_{f2}$ . The system is then naturally protected and there is no need for extra safety measurements for limiting the output current. These safety issues becomes critical in the S-S compensation topology and this is explained in Section 5.1. In the LCC compensated system the circuit acts as a current source at each coupling condition.

Starting from (3.28) and (3.29) the transferred power can be expressed as

$$P = V_{AB} \cdot I_{L_{f1}} = \frac{k\sqrt{L_1L_2}V_{AB}V_{ab}}{\omega_0L_{f1}L_{f2}} \quad (3.34)$$

Therefore, the transferred power is directly proportional to the input voltage  $V_{AB}$ , the output voltage  $V_{ab}$  and the coupling factor  $k$ . The filter inductances  $L_{f1}$  and  $L_{f2}$  allows setting the rated power without changing the main coil inductances  $L_1$  and  $L_2$ . It is possible to add a buck/boost converter either at the input of the primary inverter or after the rectification stage for having a constant power transfer.

In Chapter 5, the two compensation networks S-S and double-sided LCC are analyzed and compared for the e-bike WPT charging system, and the most suitable one is chosen.



# Power electronics topologies

Power electronics topologies for both the transmitter and receiver of the e-bike WPT charging system are discussed, referring to Figure 4.1.

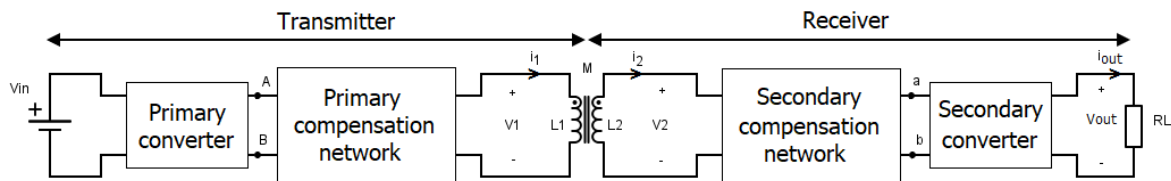


Figure 4.1: Block diagram of the e-bike WPT charging system, pointing out the converters and the compensation networks.

The secondary converter is considered to be a diode-bridge rectifier in all the following chapters, as shown in Figure 4.2.

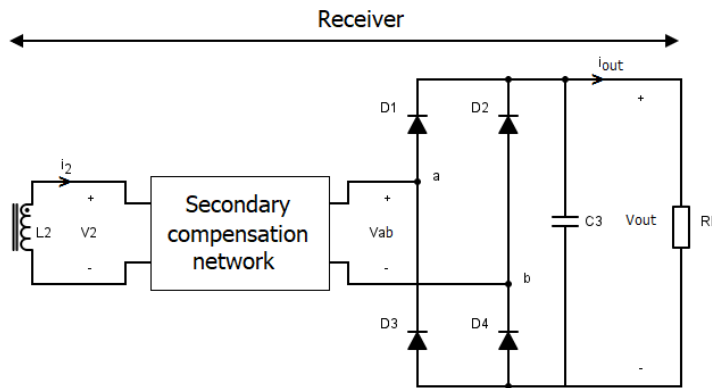


Figure 4.2: The secondary converter in its simplest topology: a diode-bridge rectifier. This topology is used in all the further analysis.

In this Chapter, topologies for the primary converter are explained, and distinguished them in two types: single-ended (Section 4.1) and double-ended (Section 4.2). These are analyzed and classified according to their number of components, the complexity of the driving circuit, voltage and current stress, electromagnetic interference (EMI), feasibility of the practical realization, then the most suitable one for the e-bike WPT charging system is chosen. Finally, in Section 4.3, two possible inverter operations are discussed and compared: the fixed frequency, and auto-resonant frequency operation, and the most appropriate one is chosen.

## 4.1. Single-ended topologies

According to [13], a single-ended converter is characterized by a magnetic flux that swings only in the first quadrant of the  $B$ - $H$  curve. Therefore, the magnetic flux in the transformer is not symmetric, which means that it is not going to zero during normal operation. Therefore, a reset winding and additional electronics are necessary. Moreover, at the same required  $\Delta B$ , a bigger magnetic core is required since the magnetic flux is only positive.

In this section, two single-ended inverters are analyzed: the Zero Voltage Switching - Voltage Source (ZVS-VS) inverter, and the Zero Current Switching - Voltage Source (ZCS-VS) inverter.

### 4.1.1. ZVS-VS inverter

The ZVS-VS inverter in Figure 4.3 is a topology widely used in induction cooking for its simplicity, since it requires only one switch and one gate driver with a relatively simple control.

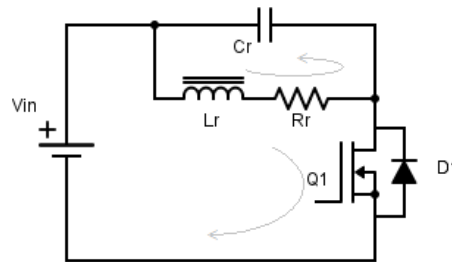


Figure 4.3: Single-ended ZVS-VS inverter schematic.

The operating cycle of the ZVS-VS inverter can be divided into 4 intervals. In Figure 4.5, the parts of the circuit that are conducting are pointed out for each interval. The dashed parts are not conducting. Moreover, the waveforms of the circuit are plotted in Figure 4.4. The waveforms are simulated in a circuit simulator using the parameter values in Table 4.1.

$t_0 - t_1$

The first interval starts as the switch is turned on. A current starts flowing through the switch and the inductor  $L_r$ , increasing and charging  $L_r$ . The capacitor  $C_r$  is blocking the input voltage and the anti-parallel diode  $D_1$  is blocked. The conducting parts of the circuit are shown in Figure 4.5 a).

$t_1 - t_2$

The second interval starts when the switch is turned off. The inductor starts charging the capacitor with the stored current, making only the resonant circuit conducting. At the same time, the voltage drop on the switch starts increasing. The voltage blocked by the switch is equal to the sum of the capacitor voltage and the input voltage. The conducting parts of the circuit are shown in Figure 4.5 b).

$t_2 - t_3$

The third interval starts when the inductor is fully discharged, and its current goes to zero. At this point, the charged capacitor starts discharging on the inductor with reverse current. This interval ends then the capacitor is fully discharged and its voltage reaches its initial value. The conducting parts of the circuit are shown in Figure 4.5 c).

$t_3 - t_4$

The fourth and last interval consists in the discharge of the negative current stored in the inductor, through the diode  $D_1$ . During this part, the gate voltage of the switch is set to the on-value, and this happens in correspondence of the small perturbation in the diode and capacitor current. However, the switches will only start conducting when the current reaches zero, and it becomes positive. The diode will not have reverse recovery losses because the current is naturally commuting from the diode to the switch. Moreover, since the anti-parallel diode is conducting immediately before the switch, it turns on at zero voltage. The conducting parts of the circuit are shown in Figure 4.5 d). At  $t = t_4$ , the same

operating cycle starts again.

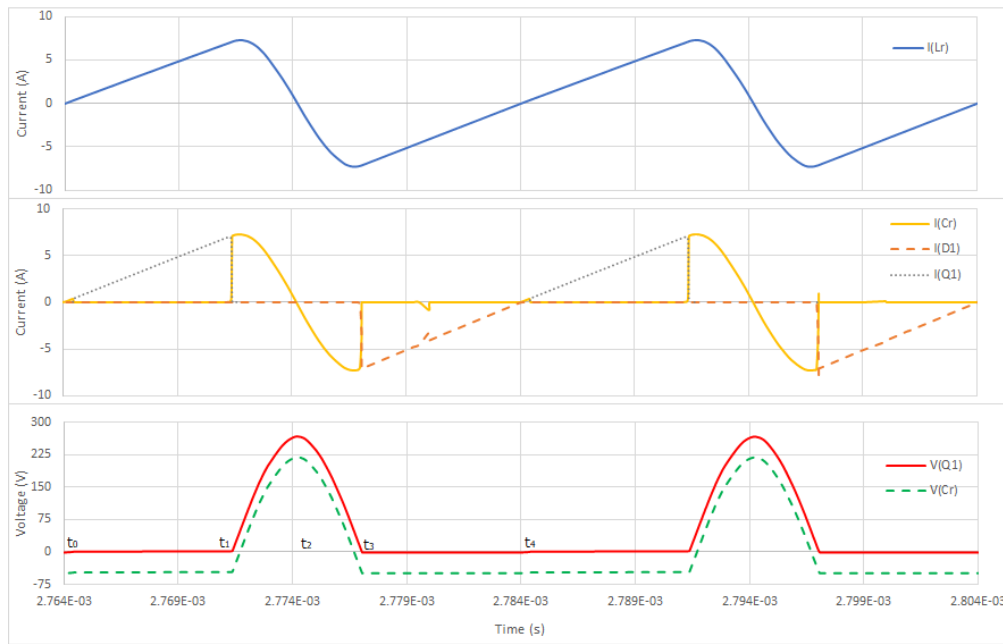


Figure 4.4: Waveforms of single-ended ZVS-VS inverter.

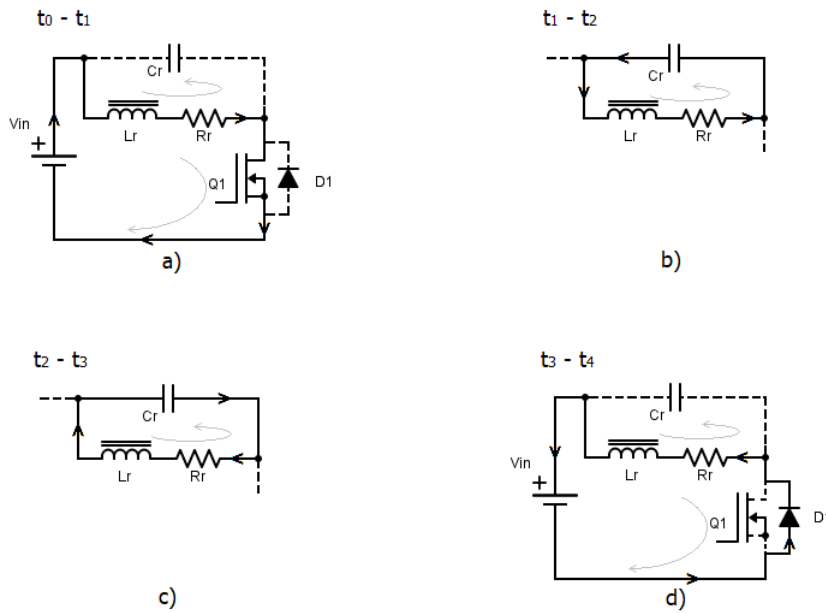


Figure 4.5: Single-ended ZVS-VS inverter during the interval: a)  $[t_0, t_1]$ , b)  $[t_1, t_2]$ , c)  $[t_2, t_3]$ , and d)  $[t_3, t_4]$ . The solid lines are conducting, and the dashed ones are not conducting.

This single-ended topology has ZVS at both turn-on and turn-off. However, the switch turns off at finite current, and the non-sinusoidal shape of  $i_{Lr}$  could also lead to EMI. Moreover, the switch needs to block 5-6 times the input voltage, which makes the use of MOSFETs not feasible. IGBTs are commonly used as switches in this topology for their high voltage capability and relatively high current rating. The anti-parallel diode should also have a high voltage blocking capability. The switching frequency is limited because the inductor needs to have time to store enough energy, such that the capacitor can charge and completely discharge, allowing the ZVS operation. So, this inverter topology is not suitable for the required frequency of 100 kHz.

Table 4.1: Value of the parameters used in the ZVS-VS inverter analysis.

Parameter	Value (Unit)
$f_0$	50 kHz
$d$	1/2
$V_{in}$	48 V
$L_r$	48 $\mu$ H
$C_r$	52 nF
$R_r$	20 m $\Omega$

#### 4.1.2. ZCS-VS inverter

The ZCS-VS inverter is another well-known topology used in induction cooking. As found in [14], Figures 4.6 a) and b) show two circuit typologies that have similar operation and allow ZCS. In the following analysis only the waveforms of the circuit in Figure 4.6 a) are discussed.

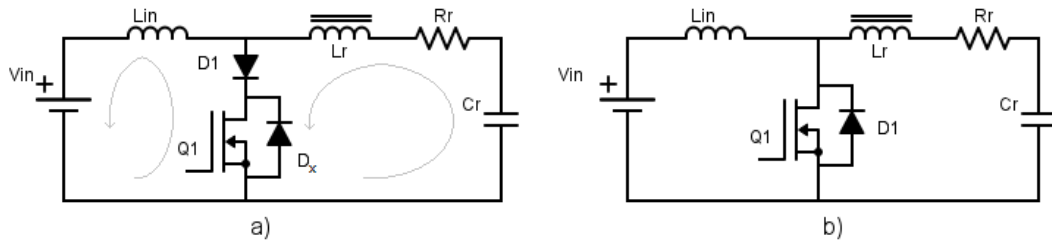


Figure 4.6: Single-ended ZCS-VS inverter schematics.

The operating cycle of the ZCS-VS inverter can be divided into four intervals according to [15]. In Figure 4.8, the parts of the circuit that are conducting are pointed out for each interval. The dashed parts are not conducting. Moreover, the waveforms of the circuit are plotted in Figure 4.7. The waveforms are simulated in a circuit simulator using the parameters value in Table 4.2.

$t_0 - t_1$

The first interval starts as the switch is turned on. The turn-on happens at zero current since the same current is flowing through  $L_{in}$  and  $L_r$  with negative sign respect to the current reference verse. However, the turn-on happens at a finite voltage, since the switch was blocking part of  $V_{C_r}$ . Then, a positive current starts flowing through the switch and  $L_r$ , while  $L_{in}$  stops conducting. At  $t_0$  the capacitor  $C_r$  is fully charged and, as the current reverses, it starts discharging. This interval ends at  $t_1$  when the voltage across  $C_r$  reaches zero, and the current is maximum. The conducting parts of the circuit are shown in Figure 4.8 a).

$t_1 - t_2$

The second interval begins when the voltage across  $C_r$  is reversed, and the current starts decreasing. The interval finishes when the current reaches zero. In both the first and the second intervals the voltage across  $C_r$  is completely balanced by  $L_r$ . In fact, during  $[t_0, t_1]$  the current is rising because  $V_{L_r}$  is greater than zero and, oppositely, during  $[t_1, t_2]$  the current is dropping since  $V_{L_r}$  is less than zero. The conducting parts of the circuit are shown in Figure 4.8 a).

$t_2 - t_3$

The third interval starts when the switch naturally stops conducting and the current reverses flowing through  $L_{in}$  and  $L_r$ . The diode  $D_1$  blocks the current from flowing in the switch. Moreover, since at  $t_3$  the gate voltage applied to the switch is still positive, the voltage drop on the switch is kept to zero and only diode  $D_1$  is blocking the reverse voltage across that leg. During this interval, the gate voltage is switched to its negative value, turning off the switch. Since the switch current was already zero at the beginning of this interval, there is ZCS also at the turn-off. This interval finishes when  $V_{C_r}$  completely discharges and it drops zero. The conducting parts of the circuit are shown in Figure 4.8 b).



$t_3 - t_4$ 

The fourth and last interval consists in the discharging of  $L_{in}$  and  $L_r$  through  $C_r$  and  $R_r$ , until instant  $t_4$  at which a positive gate signal is applied again and the switch starts conducting. At  $t_4$  the same operating cycle starts again. In this interval, the switch is reverse biased, and it blocks the reverse voltage. It also has to be noticed that in the fourth and the third intervals  $V_{C_r}$  is counteracted by the sum of the voltage across the diode-switch series and  $V_{L_r}$ . Therefore,  $V_{L_r}$  in the last two intervals is lower than in the first two ones, and that is why the current slope is less steep in this final part. The conducting parts of the circuit are shown in Figure 4.8 b). At  $t = t_4$ , the same operating cycle starts again.

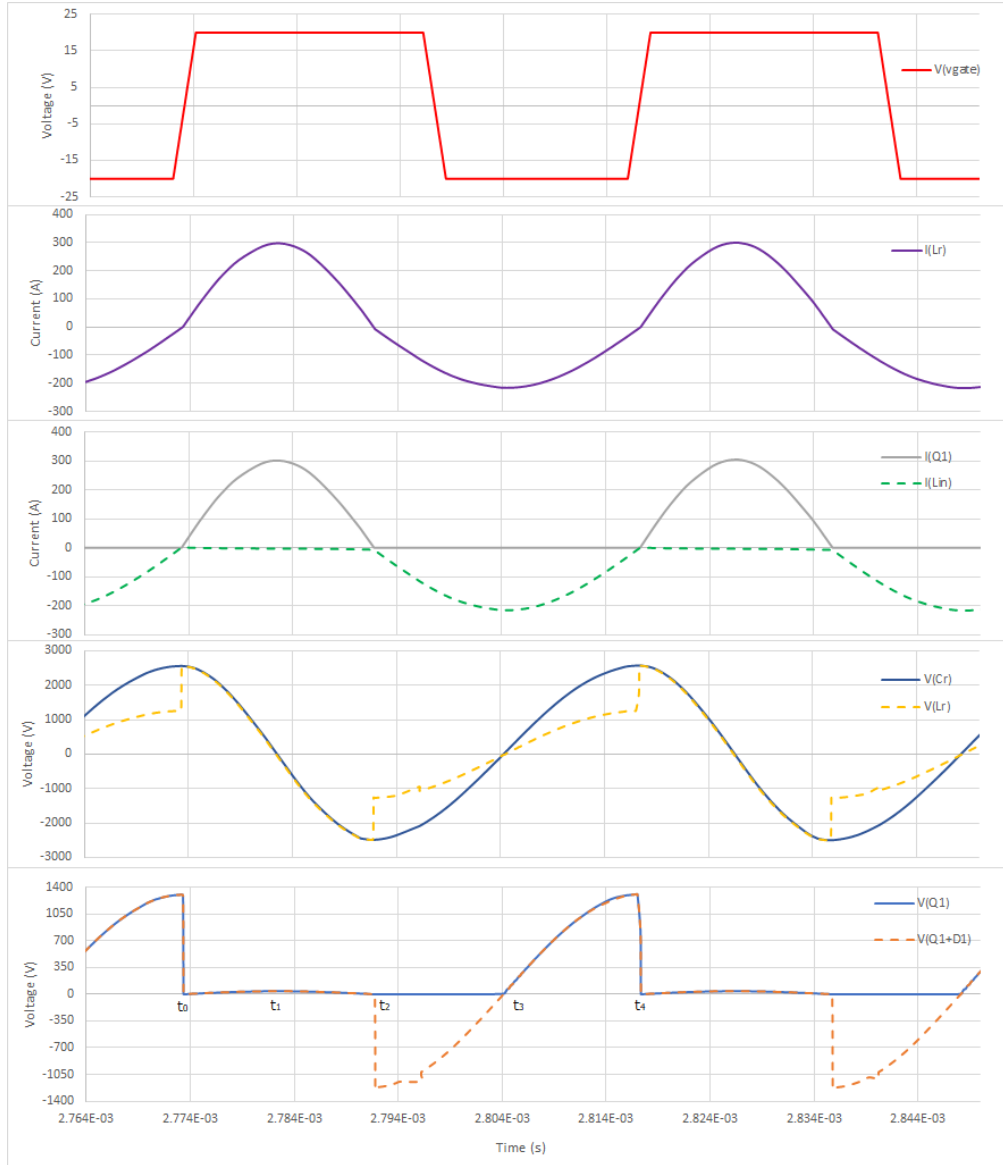


Figure 4.7: Waveforms of single-ended ZCS-VS inverter.

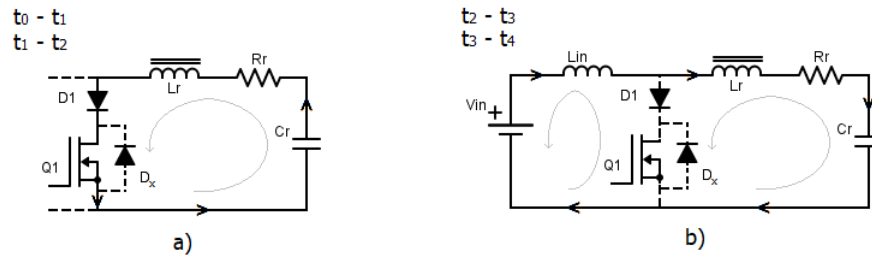


Figure 4.8: Single-ended ZCS-VS inverter during the interval: a)  $[t_0, t_1]$ , and  $[t_1, t_2]$ , b)  $[t_2, t_3]$ , and  $[t_3, t_4]$ . The solid lines are conducting, and the dashed ones are not conducting.

This single-ended topology has ZVC at both turn-on and turn-off. However, the switch turn-on at a finite voltage that is several times larger than  $V_{in}$ . This can cause huge losses in the switching components since the stored charge in its internal capacitances will be completely dissipated inside them. This is a reason why normally the ZVS is preferable than ZCS. Moreover, the switch has to stand high reverse voltages and relatively high currents, that make more feasible the use of IGBTs instead of MOSFETs. In the shown example, the waveforms have extremely high peak values because the circuit parameters are not optimized and tuned properly because this simulation is used just for having a general understanding of the circuit operation. As for the ZVS-VS inverter, also in this case, the current is not perfectly sinusoidal. However, since this operation is ZCS, the EMI would be less than in the ZVS one. Moreover, the switching frequency cannot be as high as the required one of 100 kHz, because the resonant inductor should store enough energy such that the current falls to zero before the switch gate voltage is set to its negative value. However, at the same time, the frequency cannot also be low, because in that case the current will resonate several times and the ZCS will not be achieved anymore.

According to [14], the ZCS circuit in Figure 4.6 b) has a similar conduction cycle to the one described in detail in Figure 4.6 a). The main difference consists in the conduction interval of the switch. In fact, when the switch current drops to zero, the anti-parallel diode  $D_1$  takes the negative current, and the conduction interval ends when this current goes to zero again. Then, the current starts flowing through the input inductor  $L_{in}$  and the switch leg stops conducting.

Table 4.2: Value of the parameters used in the ZVS-VS inverter analysis.

Parameter	Value (Unit)
$f_0$	22.7 kHz
$d$	1/2
$V_{in}$	48 V
$L_r$	48 $\mu$ H
$C_r$	700 nF
$R_r$	20 m $\Omega$

## 4.2. Double-ended topologies

According to [13], a double-ended converter is characterized by a magnetic flux that swings in both first and third quadrant of the  $B$ - $H$  curve. Therefore, the magnetic flux in the transformer is symmetric, and since it is going to zero during normal operation a reset winding is not necessary. Moreover, for the same required  $\Delta B$ , a smaller magnetic core is required than in a single-ended converter. In this section, three double-ended inverters are analyzed: the Royer inverter, the half-bridge (HB) and full-bridge (FB) inverter.

### 4.2.1. Royer Inverter

The Royer inverter is a self-oscillating double-ended push-pull converter for low power applications ( $\leq 2$  W), according to [16]. An example of this topology is shown in Figure 4.9.

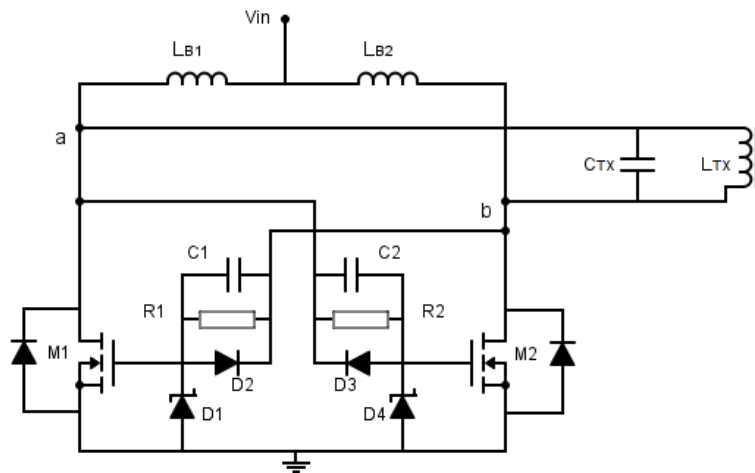


Figure 4.9: Self-oscillating Royer inverter schematic.

The input of the Royer inverter is composed of a DC voltage source  $V_{in}$  in combination with two identical input inductors  $L_{B1}$  and  $L_{B2}$ , which make the inverter current-fed. There are only two MOSFETs M1 and M2 which are directly driven by the circuit voltages  $V_a$  and  $V_b$ , respectively. Between each node voltage  $a$ ,  $b$  and the gate connection of the opposite switch, there is the parallel of a resistor, a capacitor and a diode ( $R_1$ ,  $C_1$ ,  $D_2$  for M1 and  $R_2$ ,  $C_2$ ,  $D_3$  for M2). The resistor limits the current flowing through the gate at the turn-on. On the other hand, the capacitor and the diode make the turn-off of faster, increasing the  $dv_{gs}/dt$  rate. In fact, when the switch turns off, the diode bypasses the gate resistance and the capacitor is connected to the ground, considering that the other switch is turned on. So, that capacitor is now in parallel with the internal gate-source capacitance of the switch, which can discharge faster. Moreover, there is a Zener diode connected between the gate and the source of each switch ( $D_1$  for M1 and  $D_4$  for M2), which blocks the over-voltage across the switch during its conducting interval. Finally, the parallel of the transmitting coil  $L_{TX}$  and the compensating capacitor  $C_{TX}$  is connected between the circuit nodes  $a$  and  $b$ .

The operating cycle of this inverter is relatively simple and its waveforms, simulated with a circuit simulator, are shown in Figure 4.10 using the parameter values in Table 4.3 found in [16]. Moreover, in the simulation the transmitter coil  $L_{TX}$  is coupled with a receiver coil  $L_{RX}(= L_{TX})$ , which is connected in parallel with a compensating capacitor  $C_{RX}(= C_{TX})$  and a resistive load  $R_L = 10 \Omega$ .

The operating cycle can be divided into two intervals.

$t_0 - t_1$

In the first interval, the voltage  $V_{ab}$  across the primary compensation capacitor  $C_{TX}$  swings in the positive half-wave. The switch M2 starts conducting since it is supplied with the positive gate voltage  $V_a$ . The voltage  $V_b$  goes to zero because M2 is conducting. The gate voltage applied to M1 is zero and it starts blocking the voltage  $V_a$ . This interval ends when  $C_{TX}$  discharges completely and  $V_{ab}$  drops to zero again.

$t_1 - t_2$

In the second and final interval, the voltage  $V_{ab}$  across the primary compensation capacitor  $C_{Tx}$  swings in the negative half-wave and the opposite situation of the first interval happens. The switch M1 starts conducting since it is supplied with the positive gate voltage  $V_b$ . The voltage  $V_a$  goes to zero because M2 is conducting. So, the gate voltage applied to M1 is zero and it starts blocking the voltage  $V_b$ . This interval ends when  $C_{Tx}$  discharges completely and  $V_{ab}$  drops to zero again. At  $t = t_2$ , the same operating cycle starts again.

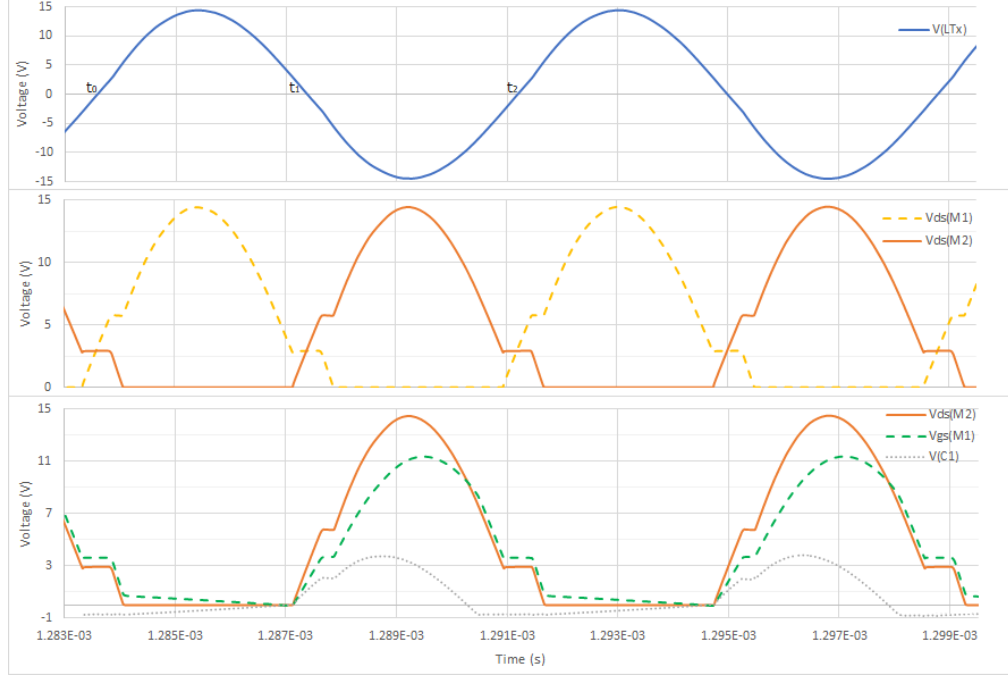


Figure 4.10: Waveforms of the double-ended Royer inverter.

So, the two switches are naturally switched on and off by the voltage  $V_{ab}$  across the compensation capacitor  $C_{Tx}$ . From the simulated waveforms in Figure 4.10,  $V_{ds}$  shows a flat plateau at two different voltage levels for both turn-on and turn-off. The reason of this can be found in (4.1).

$$V_{ab} = V_a - V_b = V_{ds,M1} - V_{ds,M2} = \underbrace{(V_{gs,M2} + V_{C2})}_{V_{ds,M1}} - \underbrace{(V_{gs,M1} + V_{C1})}_{V_{ds,M2}} \quad (4.1)$$

Therefore, the flat portions of  $V_{ds}$  are caused by the ones of the opposite switch  $V_{gs}$ , in correspondence of the gate threshold voltage. However,  $V_{ds}$  has two asymmetrical flat plateau voltage levels, because it is equal to the sum of the opposite switch's  $V_{gs}$  and the voltage across the capacitor connected to the opposite switch.

Table 4.3: Value of the parameters used in the circuit analysis of the Royer inverter.

Parameter	Value (Unit)
$V_{in}$	5 V
$L_{B1}, L_{B2}$	68 $\mu$ H
$L_{Tx}$	5 $\mu$ H
$C_{Tx}$	300 nF
$C_1, C_2$	10 nF
$R_1, R_2$	100 $\Omega$

The Royer inverter is a double-ended topology composed of two switches which are driven directly by the circuit voltage of the nodes  $a$  and  $b$  and so, they do not require a gate driver circuit. The described system is suitable for low power applications ( $\leq 2\text{ W}$ ) in which the input voltage is  $5\text{ V}$ , such that the gate voltage swings naturally between  $0$  and  $15\text{ V}$ . However, in the e-bike wireless charging system  $V_{in}$  is  $48\text{ V}$  that would not make any more the resonant voltage swing between  $-15$  and  $15\text{ V}$ . Therefore, a gate driver for each switch is needed and it could easily control the switch by comparing the sign of the resonant voltage.

Moreover, the primary compensation capacitor is placed in parallel to the primary coil for making the system self-oscillating. However, in case of parallel compensation at the primary, the compensation capacitance choice is dependent on  $k$  and  $R_L$  for having  $\text{PF}=1$ , as shown in Table 3.1. Since in the e-bike WPT charging system the coils' position is not fixed, and the load is changing as the battery is charging, a parallel compensation at the primary is not desirable for having a good power transfer.

#### 4.2.2. Half-bridge

The Half-bridge inverter is a well-known double-ended topology, composed of a switch leg of two series switches with their anti-parallel diode and two series capacitors in parallel to the switch leg, as shown in Figure 4.11. The capacitors must be large enough to keep a constant voltage equal to half the input voltage  $V_{in}$ .

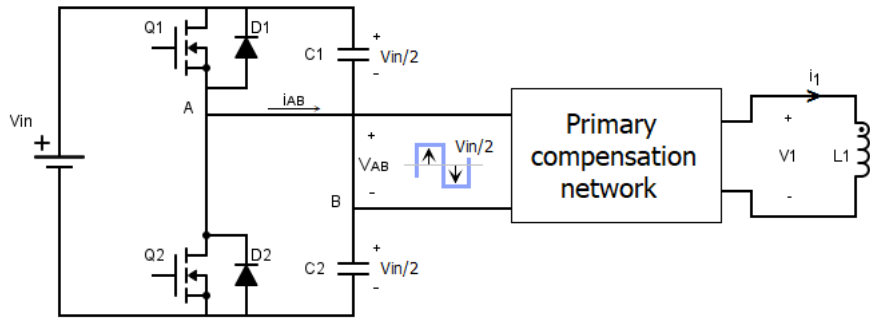


Figure 4.11: Half-bridge inverter schematic.

The output of this inverter is the square wave voltage  $V_{AB}$  that varies between  $-V_{in}/2$  and  $+V_{in}/2$ . In particular,  $V_{AB} = -V_{in}/2$  when  $Q1$  is off and  $Q2$  is on, and  $V_{AB} = +V_{in}/2$  when  $Q1$  is on and  $Q2$  is off. Unity PF at the primary circuit can be achieved by controlling and setting the proper switching frequency and duty cycle. The operating frequency of the inverter is explained in detail in Section 4.3.

According to [17], the voltage and current stress on each switch is

$$V_Q \equiv V_{in} \quad (4.2)$$

$$I_Q \equiv i_{AB,peak} \quad (4.3)$$

Therefore, the switch voltage blocking capability depends only on the input voltage and not on the resonant voltage, that could be in the order of  $\text{kV}$ . However, since the whole resonant current flows through the switches, it has to be within the maximum rating limit.

The half-bridge inverter is widely used because it requires only two switches and consequently two gate drivers, making the control of the inverter relatively easy.

### 4.2.3. Full-bridge

The Full-bridge inverter is a well-known double-ended topology, composed of two switch legs as shown in Figure 4.12. Therefore, the inverter has four switches and four gate drivers in total.

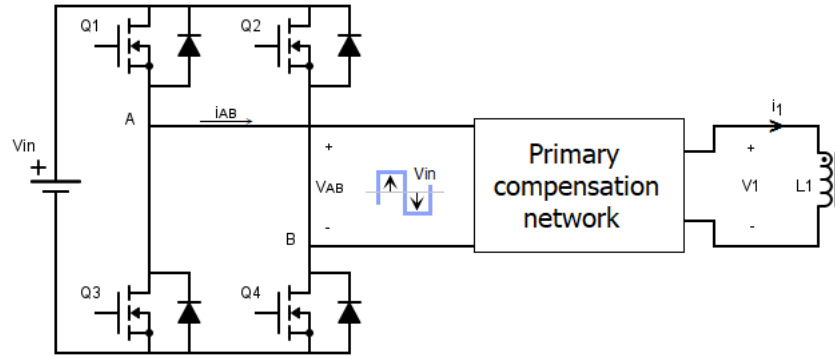


Figure 4.12: Full-bridge inverter schematic.

The output of this inverter is the square wave voltage  $V_{AB}$  that varies between  $-V_{in}$  and  $+V_{in}$ . In particular,  $V_{AB} = -V_{in}$  when Q1, Q4 are off and Q2, Q3 are on and  $V_{AB} = +V_{in}$  when Q1, Q4 are on and Q2, Q3 are off. Similarly to the half-bridge inverter, unity PF at the primary circuit can be achieved by controlling and setting the proper switching frequency and duty cycle. The operating frequency of the inverter is explained in detail in Section 4.3.

According to [17], the voltage and current stress on each switch is

$$V_Q \equiv V_{in} \quad (4.4)$$

$$I_Q \equiv i_{AB,peak} \quad (4.5)$$

Therefore, the stress on each switch is the same as in the half-bridge inverter.

This inverter involves double the switches and the gate drivers than in the half-bridge inverter. Therefore, the control is more complex, and its cost is higher than in the half-bridge. However, it reverses the input voltage fully while the half-bridge inverter reverses just half of it. Therefore, for the same power rating  $P$  and constant  $V_{in}$ , the output current of the half-bridge inverter will be double than the full-bridge one. So, the full-bridge topology is preferable in applications with large resonant output current. In terms of equations:

*Half-bridge*

$$\begin{cases} P = V_{AB,HB} I_{AB,HB} \\ V_{AB,HB} = \frac{V_{in}}{2} \end{cases} \rightarrow I_{AB,HB} = \frac{P}{\frac{V_{in}}{2}} = \frac{2P}{V_{in}} \quad (4.6)$$

*Full-bridge*

$$\begin{cases} P = V_{AB,FB} I_{AB,FB} \\ V_{AB,FB} = V_{in} \end{cases} \rightarrow I_{AB,FB} = \frac{P}{V_{in}} = \frac{I_{AB,HB}}{2} \quad (4.7)$$

The full-bridge inverter is chosen for the e-bike WPT charging system, because it reverses the full input voltage  $V_{in}$ .

### 4.3. Comparison between fixed frequency and auto-resonant frequency operation

The full-bridge inverter is chosen for the e-bike WPT charging system, and the further analysis is focused on its operation, that can be either at fixed frequency or auto-resonant frequency.

Most of the papers on wireless charging consider the fixed frequency operation for the inverter, in which the controller sets the gate drivers to work at that frequency that generally is the chosen resonant frequency  $f_0$ . However, in a real application, the parameters differ from the design ones, and the resonance happens at a frequency slightly different from the chosen one. Moreover, the bifurcation phenomenon introduces extra resonant frequencies in the system, which depend on both  $k$  and  $R_L$ . Therefore, an AC frequency sweep is sent periodically from the controller and the input DC power is measured at the primary circuit for each frequency. Then, the frequency at which corresponds the maximum is chosen as the operating frequency  $f_{res}$  of the inverter. This fixed frequency control of the inverter is shown in Figure 4.13 a). However, this method involves considerable digital control, and it takes some time to detect the proper operating frequency. Besides, the AC frequency sweep has to be repeated often during the charging process, because some changes in the system could change the optimal working point. Additionally, the positive and the negative resonant current half-wave could be not completely symmetrical, and it would be better to have more freedom in setting the duty cycle, instead of assuming that is 50% by default.

On the other hand, in case the system is working at auto-resonant frequency, it is possible to reach the ZCS by commutating the switch leg when the current crosses zero. So, considering the full-bridge inverter in Figure 4.12, when  $i_{AB}$  is greater than zero the switches Q1, Q4 conduct and the switches Q2, Q3 are blocked, such that  $V_{AB} = +V_{in}$ . Once  $i_{AB}$  drops to zero and reverses, the switches Q1, Q4 are blocked and the switches Q2, Q3 conduct such that  $V_{AB} = -V_{in}$ . In this operation, the control is naturally following the proper resonant frequency of the system, bringing soft-switching and unity PF, since the current  $i_{AB}$  is in phase with  $V_{AB}$ . This auto-resonant frequency control of the inverter is shown in Figure 4.13 b). The zero-crossing detection circuit is relatively easy to implement using comparators. The duty cycle control could be flexible, treating the positive and the negative resonant current half-wave separately. The system is still acting as a current source, but the output current can vary because, in the case of bifurcation, the system could have multiple resonant frequencies. In that case, the control circuit needs to be able to handle the bifurcation effects without compromising the inverter operation. So, some circuit protections could be necessary.

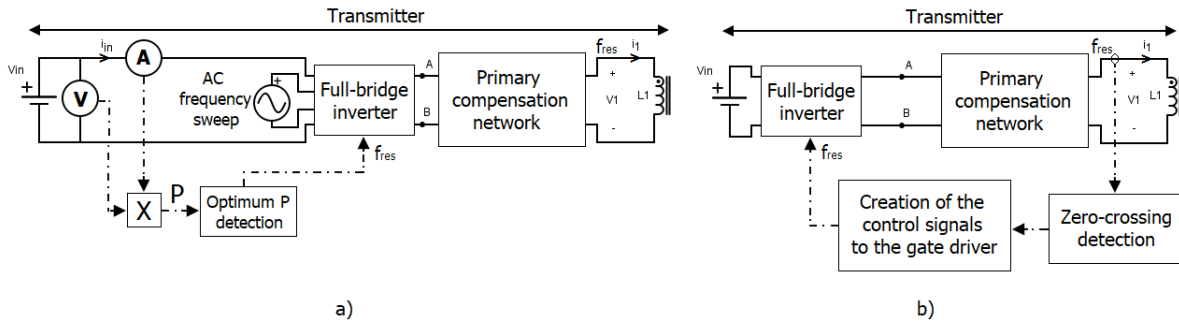


Figure 4.13: Transmitter circuit of the e-bike WPT charging system, in which the full-bridge inverter is operating at: a) fixed frequency, and b) auto-resonant frequency.

### 4.3.1. Zero Voltage Switching operation

The double-sided LCC system operating at  $f_0$  is naturally working at ZCS since  $V_{ab}$  and  $I_{L_{f1}}$  are in phase, as shown in section 3.4. At turn-off, the losses are limited because the voltage drop across the switch is low ( $\approx 2$  V). However, at the turn-on, the charge stored in the output capacitance  $C_{oss}$  of the switch is dissipated internally, and this highly affects the switching losses. So, it is preferable realizing ZVS operation for improving the switching performance.

As stated in [12] and [18], ZVS can be achieved when  $I_{L_{f1}}$  lags  $V_{AB}$ , and this happens when the input impedance  $Z_{in}$  is slightly inductive. During the commutations, each switch will turn-off at finite current and turn-on at zero-current and zero-voltage, because its anti-parallel diode conducts a negative current before the switch itself starts conducting the positive current. It is possible to make  $Z_{in}$  inductive adding a certain  $\Delta C_2$  to the secondary capacitor  $C_2$ , as shown in Figure 4.14. This quantity is chosen such that the turn-off current  $I_{off}$  value is high enough for discharging the switch output capacitance  $C_{oss}$  in the dead time, at any coupling and load condition. However, it is also preferable to keep  $I_{off}$  low, for having as small as possible hard-switching at the turn-off. Therefore, a trade-off between ZCS and ZVS must be found for optimizing the switching losses in the primary inverter.

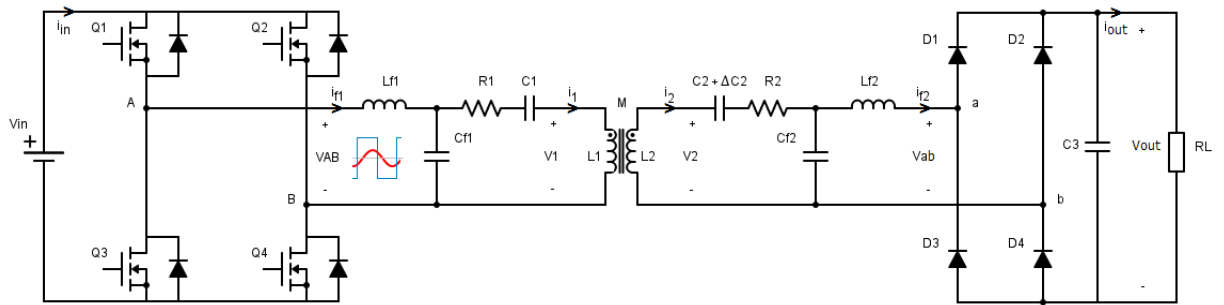


Figure 4.14: Full-bridge inverter working at ZVS in combination of a double-sided LCC compensation network.



### 4.3.2. Summary of the comparison between fixed frequency and auto-resonant frequency operation

In Section 4.3, the fixed frequency and auto-resonant frequency operation of the full-bridge inverter are compared. Table 4.4 summarizes the positive and negative attributes of these two operations. Each attribute is classified with either a +, - or 0. The + indicates a positive attribute, The - indicates a negative attribute, and the 0 indicates a neutral attribute.

Table 4.4: Comparison between fixed frequency and auto-resonant frequency operation. Each attribute is classified with either a +, - or 0. The + indicates a positive attribute, The - indicates a negative attribute, and the 0 indicates a neutral attribute.

	Inverter operation	
	Fixed frequency	Auto-resonant frequency
ZCS	0	+
ZVS using LCC compensation	+	-
Following naturally the resonant frequency $f_{ref}$ of the circuit	-	+
No need to stop the power transfer for finding the proper $f$ , such that $f = f_{ref}$	-	+
Simplicity of the control	-	+
Communication through the power line	0	0
Foreign Object Detection (Section 7.2.4)	0	0
Maximum power transfer with the varying of $k$ and $R_L$	-	+
Maximum efficiency with the varying of $k$ and $R_L$	-	+

In Chapter 5, two configurations for the e-bike WPT charging system are analyzed and compared: a full-bridge inverter working at auto-resonant frequency in combination of a S-S compensation network and a full-bridge inverter working at fixed frequency in combination of a double-sided LCC compensation network. The most suitable compensation network and operating strategy for the inverter are then chosen.



## Comparison between S-S and LCC compensations in the charging system

In this Chapter, two configurations for the e-bike wireless charging system are analyzed and compared: a full-bridge inverter working at auto-resonant frequency with an S-S compensation network in Section 5.1, and a full-bridge inverter working at fixed frequency with a double-sided LCC compensation network in Section 5.2. Both have a diode-bridge rectifier between the output of the secondary compensated network and the resistive load. Finally, the most suitable configuration is chosen in Section 5.3.

### 5.1. Series-series compensation in the charging system

The analysis of the basic S-S compensation network in Section 3.3 is executed applying an AC frequency sweep at the input voltage terminals A, B and having an AC voltage across the load  $R_L$ . However, in the real WPT charging system, a square wave voltage is applied at the input terminals A, B which is provided by a full-bridge inverter. The voltage source  $V_{in}$  is a DC voltage applied at the input of the inverter. The phasors' analysis of Section 3.3 is still valid in first approximation, considering the first harmonic component of the square wave voltage. Moreover, since the  $R_L$  is a battery, it needs to be charged with DC voltage. So, the power picked-up from the secondary compensation network is rectified by a diode-bridge such that there is DC power through the equivalent load  $R_L$ . Therefore, the e-bike WPT charging system is composed of a full-bridge inverter, a series-series compensation network and a diode-bridge rectifier as shown in Figure 5.1.

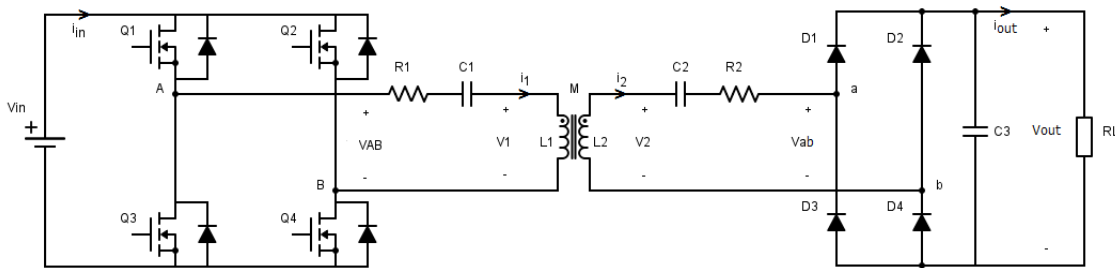


Figure 5.1: S-S compensation schematic in the e-bike wireless charging system.

The operation of the full-bridge inverter could be either at fixed or at auto-resonant frequency, as explained in Section 4.3. In case it would work at fixed frequency, the operating frequency is found by sending periodically a AC sweep of frequency and choosing the one at which the maximum power at the primary is measured. However, the auto-resonant frequency operation is more interesting for this charging system because, if the primary inverter follows the natural resonance of the circuit, any change in the frequency is automatically tracked and there is no need of a complex digital control for sending the AC sweep. These two operations of the inverter are shown schematically in Figure 4.13. The configuration with the S-S compensation network is analyzed only at auto-resonant frequency.

According to Kirchhoff voltage law in (3.7) and neglecting the parasitic resistance  $R_1$ , at  $f_0$  the system is acting as a current source with a secondary current  $I_2$  equal to

$$|I_2| = \frac{V_{AB}}{\omega_0 M} = \frac{V_{in}}{2\pi f_0 k \sqrt{L_1 L_2}} \quad (5.1)$$

The output current is then directly proportional to  $V_{in}$  because the input DC voltage is fully inverted by the full-bridge, and inversely proportional to  $f_0$  and  $k$ . This means that the output current increases as the coils misalignment increases. So, according to [12], the secondary circuit has to be provided of a position detection system for making sure that the two coils are not too far apart, such that the secondary current will not increase over the limit.

### 5.1.1. Analysis at variable load $R_L$ and coupling factor $k$

The WPT charging system is characterized by a variable load as the battery is charging during the process and by a variable mutual inductance between the two coils depending on their position. So, for analyzing the system behavior at steady-state, the schematic in Figure 5.1 is simulated at three values of coupling factor  $k = 0.1, 0.17, 0.25$  and at six values of the resistive load  $R_L = 2, 5, 10, 15, 30, 60, 100 \Omega$ . The value of all the other parameters in the circuit is shown in Table 3.2. This analysis is focused on the input and output power at the DC side, on the efficiency of the total system and on the current and voltage stress on the resonant components. According to Figure 5.1, the DC input and output power are defined as

$$P_{in(out)} = V_{in(out)} I_{in(out)} \quad (5.2)$$

and consequently, the efficiency of the entire system is

$$\eta_{DC} = \frac{P_{out}}{P_{in}} = \frac{V_{out} I_{out}}{V_{in} I_{in}} \quad (5.3)$$

$\eta_{DC}$  includes also the losses of the inverter and the rectifier. However, the MOSFETs in the simulations are considered ideal making the power loss in the inverter  $\approx 0$  W. On the other hand, the diodes in the rectifier-bridge are also ideal, but with a voltage drop during the conduction of 0.6 V.

Figure 5.2 shows the results for the lowest coupling  $k=0.1$ . Figure 5.3 shows the results for  $k=0.17$ . Finally, Figure 5.4 shows the results for the highest coupling  $k=0.25$ .

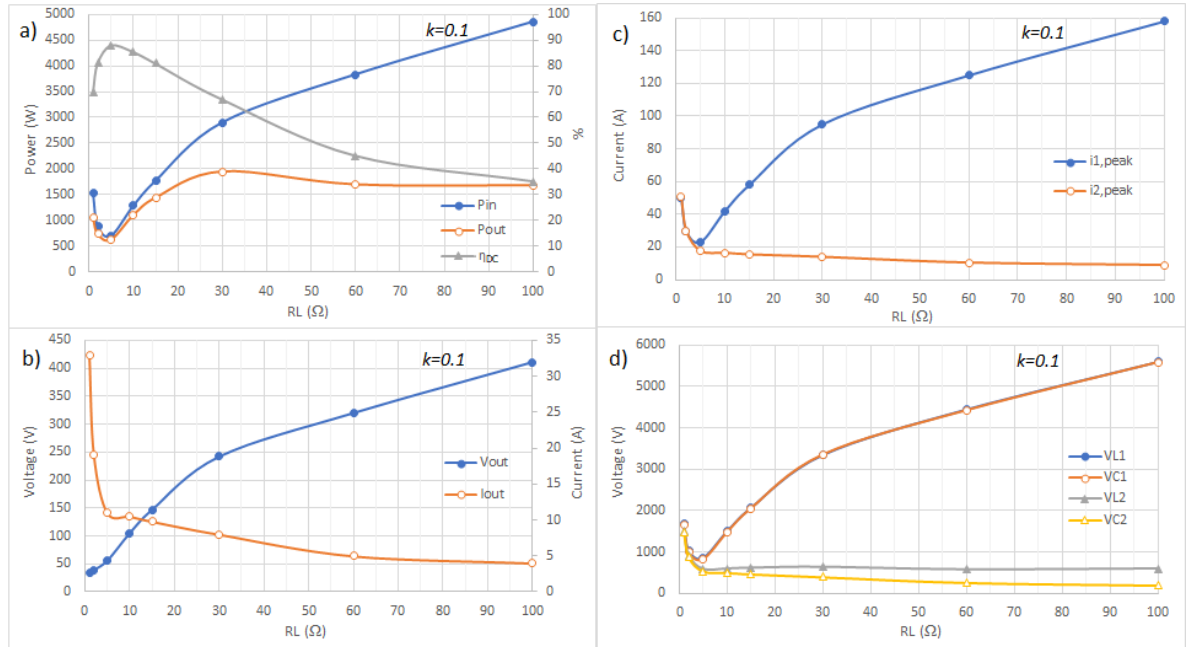


Figure 5.2: Simulation results of S-S compensated system at  $k=0.1$ , depending on the load resistance  $R_L$ . Plot of a) DC input power  $P_{in}$ , DC output power  $P_{out}$  and efficiency  $\eta_{DC}$ , b) output voltage  $V_{out}$  and current  $I_{out}$  across  $R_L$ , c) peak current through  $L_1$  and  $L_2$ , d) peak voltage across  $L_1$ ,  $C_1$ ,  $L_2$  and  $C_2$ .

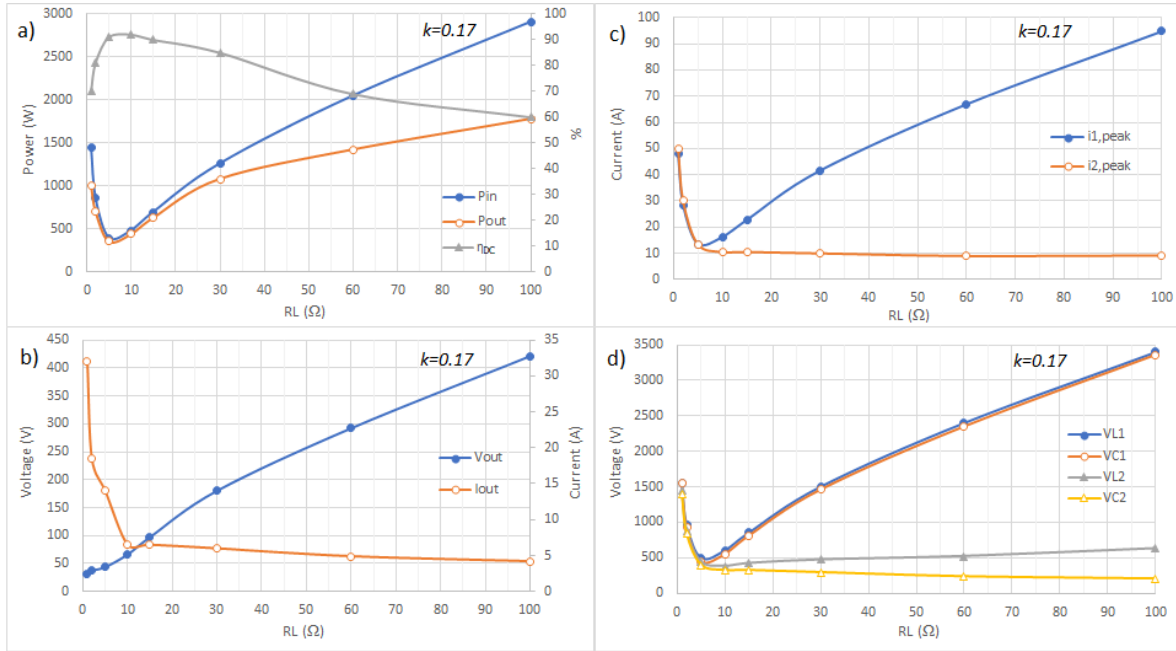


Figure 5.3: Simulation results of S-S compensated system at  $k=0.17$ , depending on the load resistance  $R_L$ . Plot of a) DC input power  $P_{in}$ , DC output power  $P_{out}$  and efficiency  $\eta_{DC}$ , b) output voltage  $V_{out}$  and current  $I_{out}$  across  $R_L$ , c) peak current through  $L_1$  and  $L_2$ , d) peak voltage across  $L_1$ ,  $C_1$ ,  $L_2$  and  $C_2$ .

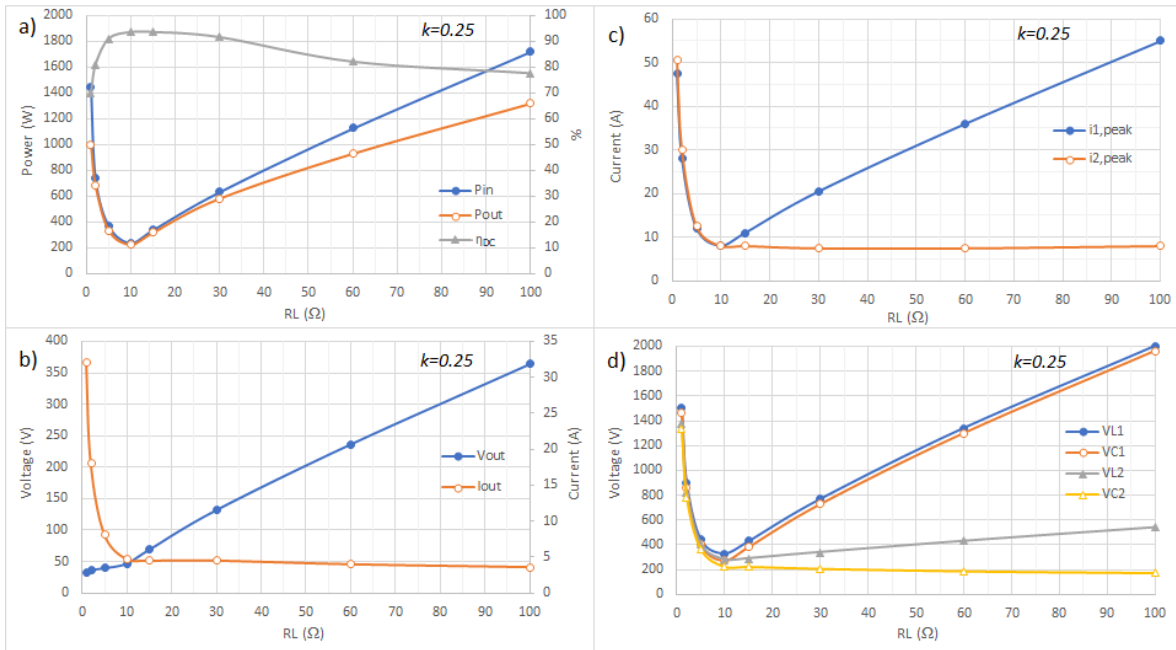


Figure 5.4: Simulation results of S-S compensated system at  $k=0.25$ , depending on the load resistance  $R_L$ . Plot of a) DC input power  $P_{in}$ , DC output power  $P_{out}$  and efficiency  $\eta_{DC}$ , b) output voltage  $V_{out}$  and current  $I_{out}$  across  $R_L$ , c) peak current through  $L_1$  and  $L_2$ , d) peak voltage across  $L_1$ ,  $C_1$ ,  $L_2$  and  $C_2$ .

### 5.1.2. Results discussion of S-S compensation

The steady-state behavior of the WPT charging system with S-S compensation has been simulated at three different values of  $k$  and the results are shown in Figure 5.2, 5.3 and 5.4, depending on  $R_L$ . Three main considerations must be pointed out.

Firstly, as the coupling factor decreases, the required input power  $P_{in}$  for having a certain output power  $P_{out}$  increases. Especially at low coupling and higher resistive loads ( $R_L > 30 \Omega$ ) the difference between  $P_{in}$  and  $P_{out}$  becomes relevant. The reason for this increase of  $P_{in}$  is the increase in the primary current at higher loads. In fact, from (3.8) the primary current  $I_1$  at  $f_0$  can be written as

$$|I_1| = \frac{R_L}{\omega_0 M} I_2 = \frac{R_L}{2\pi f_0 k \sqrt{L_1 L_2}} I_2 \quad (5.4)$$

$I_1$  is directly proportional to  $R_L$  and inversely proportional to  $k$ . So,  $I_1$  increases as the resistive load increases and the coupling decreases, causing a higher  $P_{in}$ . This behavior of  $I_1$  also matches the result of the AC analysis in Figure 3.6 a), where  $I_1$  peak is increasing as  $R_L$  increases. Another reason for this power loss is that the diodes in the bridge rectifier are not conducting the all-time at higher values of  $R_L$ , because the operation is in discontinuous conduction mode (DCM). This means that all four diodes are reversed biased when  $I_{out} = 0$  A. It also has to be noticed that the first harmonic approximation is not valid in DCM.

Consequently, the efficiency is also highly affected by this increase in  $I_1$ , and it drops significantly at higher loads. The minimum efficiency achieved is  $\eta_{DC} = 35\%$  at  $k = 0.1$  and  $R_L = 100 \Omega$ . As  $k$  increases, the efficiency is higher and with a more constant trend. The maximum efficiency achieved is  $\eta_{DC} = 93.5\%$  at  $k = 0.25$  and  $R_L = 10 \Omega$ .

Secondly, for lower resistive load values ( $R_L < 10 \Omega$ ), the results agree with ones the AC analysis in Section 3.3.2 about the effects of the bifurcation phenomenon. In fact, for a lower  $R_L$ , the system has two extra resonant frequencies apart from the designed one. The operating frequency is chosen detecting the zero crossing of  $i_1$ . Since the operation starts from 0 Hz, it stops naturally to the first resonant frequency found, which is the lowest one. Therefore, since  $I_1$  and  $I_2$  are inversely proportional to the operating frequency, they increase considerably in case bifurcation happens. The same behavior can be found in the AC analysis in Figure 3.6 and 3.8. When  $R_L$  increases, the two-extra resonant frequencies are gradually getting closer to the design frequency until the bifurcation completely disappears and the system has just one resonant frequency. According to these results, the minimum value of  $R_L$  at which the bifurcation stops is lower for smaller values of  $k$ . This characteristic also agrees with (3.19).

Thirdly, the voltage and current stress on the  $L$ ,  $C$  resonant components are also investigated. High oscillating voltages and currents characterize both the primary and secondary resonant circuits. In particular, the increase of  $I_1$  at low  $k$  and high  $R_L$  values causes high current and voltage stress on components in the primary circuit, that is up to three times more than in the case of maximum  $k$ . These stress values must be taken into account when the component chosen, making sure that they can stand these conditions.

## 5.2. LCC compensation in the charging system

The double-sided LCC compensation network is analyzed in Section 3.4 according to Figure 3.15, where the input voltage  $V_{AB}$  and the output voltage  $V_{ab}$  are sinusoid. However, in the e-bike WPT charging system the input voltage  $V_{AB}$  is a square wave voltage provided by a full-bridge inverter. The inverter is supplied by a DC voltage  $V_{in}$ . The analysis using phasors in Section 3.4 is still valid in first approximation, which means that only the first harmonic component of the square wave voltages  $V_{AB}$  and  $V_{ab}$  is considered. Moreover, since the real load is a battery, it needs to be charged with DC voltage. So, the power picked-up from the secondary compensation network is rectified by a diode-bridge such that there is DC power through the equivalent load  $R_L$ . Therefore, the e-bike WPT charging system is composed of a full-bridge inverter, a double-sided LCC compensation network and a diode-bridge rectifier as shown in Figure 5.5.

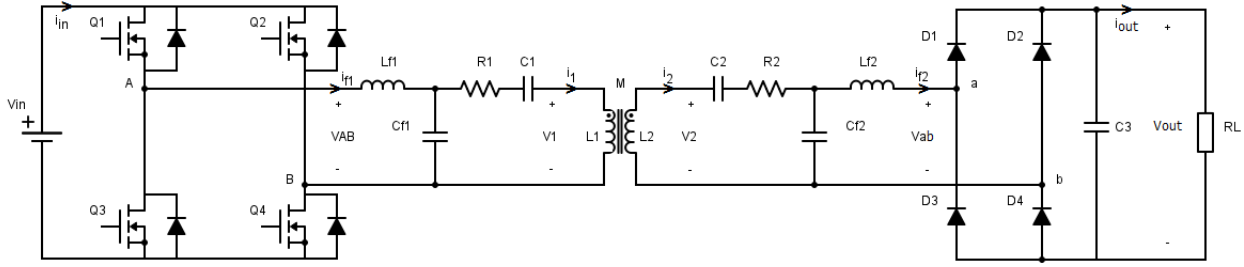


Figure 5.5: Double-sided LCC compensation schematic in the e-bike WPT charging system.

The operation of the full-bridge inverter could be either at fixed frequency or at auto-resonant frequency, as explained in Section 4.3. However, in this case only the operation at fixed frequency is considered, because the primary circuit resonates just at the design frequency  $f_0$ . The combination of the series  $L_1$ ,  $C_1$  and the extra filter composed of  $L_{f1}$  and  $C_{f1}$  is tuned at  $f_0$  and the whole analysis done in the Appendix B would not be valid. The fixed frequency operation of the inverter is shown schematically in Figure 4.13 a).

### 5.2.1. Analysis at variable load $R_L$ and coupling factor $k$

The WPT charging system is characterized by a variable load as the battery is charging during the process and by a variable mutual inductance between the two coils depending on their position. So, for analyzing the system behavior at steady-state, the schematic in Figure 3.15 is simulated at three values of coupling factor  $k = 0.1, 0.17, 0.25$ , at six values of the resistive load  $R_L = 2, 5, 10, 15, 30, 60, 100 \Omega$ . The value of all the other parameters in the circuit is shown in Table 5.1. As discussed before, choosing the filter inductances  $L_{f1}$  and  $L_{f2}$  allows to set the rated power without changing the main coil inductances. In fact,  $L_1$  and  $L_2$  in table 5.1 have the same value as in Table 3.2.  $L_{f1}$  and  $L_{f2}$  are chosen such that

$$L_{f1} = L_{f2} \quad (5.5)$$

for having a symmetric system, and

$$I_{L_{f2}} = 5 \text{ A} \quad \text{at} \quad k = 0.1 \quad (5.6)$$

for ensuring a certain amount of output current at the minimum coupling condition.

$L_{f1}$  and  $L_{f2}$  are then calculated from (3.33), (5.5) and (5.6). The capacitances  $C_{f1}$ ,  $C_{f2}$ ,  $C_1$  and  $C_2$  are consequently computed using (3.24), (3.25), (3.26) and (3.27). This analysis is focused on the input and output power at the DC side, on the efficiency of the total system and on the current and voltage stress on the resonant components. According to Figure 5.5, the DC input and output power  $P_{in(out)}$ , and the efficiency  $\eta_{DC}$  is defined as in (5.7) and (5.8), respectively.

$$P_{in(out)} = V_{in(out)} I_{in(out)} \quad (5.7)$$

$$\eta_{DC} = \frac{P_{out}}{P_{in}} = \frac{V_{out} I_{out}}{V_{in} I_{in}} \quad (5.8)$$

$\eta_{DC}$  includes also the losses of the inverter and the rectifier. However, the MOSFETs in the simulations are considered ideal making the power loss in the inverter  $\approx 0$  W. On the other hand, the diodes in the rectifier-bridge are also ideal, but with a voltage drop during the conduction of 0.6 V. Figure 5.6 shows the results for the lowest coupling  $k=0.1$ .

Figure 5.7 shows the results for  $k=0.17$ . Finally, Figure 5.8 shows the results for the highest coupling  $k=0.25$ .

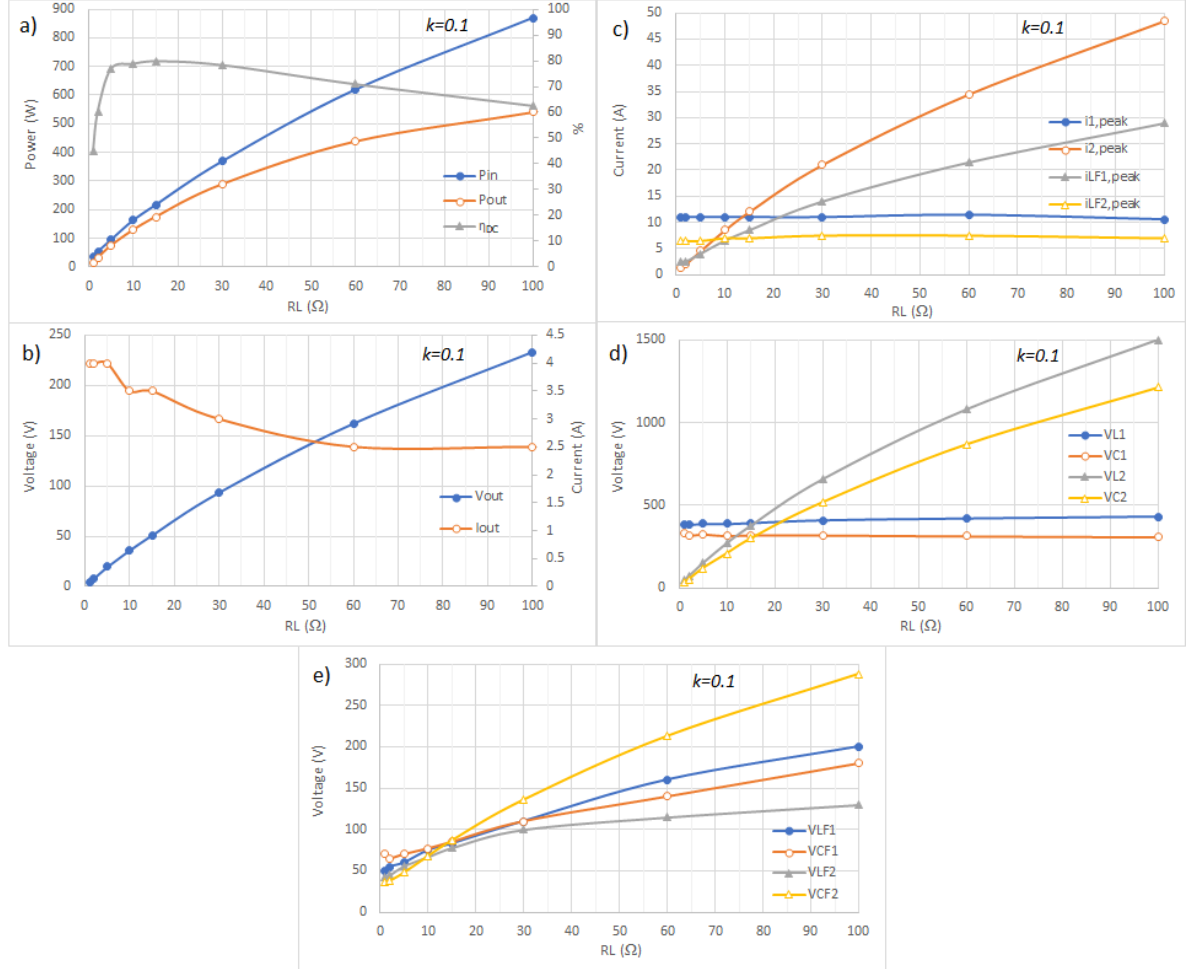


Figure 5.6: Simulation results of double-sided LCC system at  $k=0.1$ , depending on the load resistance  $R_L$ . Plot of a) DC input power  $P_{in}$ , DC output power  $P_{out}$  and efficiency  $\eta_{DC}$ , b) output voltage  $V_{out}$  and current  $I_{out}$  across  $R_L$ , c) peak current through  $L_1$ ,  $L_2$ ,  $L_{f1}$  and  $L_{f2}$ , d) peak voltage across  $L_1$ ,  $C_1$ ,  $L_2$  and  $C_2$ , e) peak voltage across  $L_{f1}$ ,  $C_{f1}$ ,  $L_{f2}$  and  $C_{f2}$ .



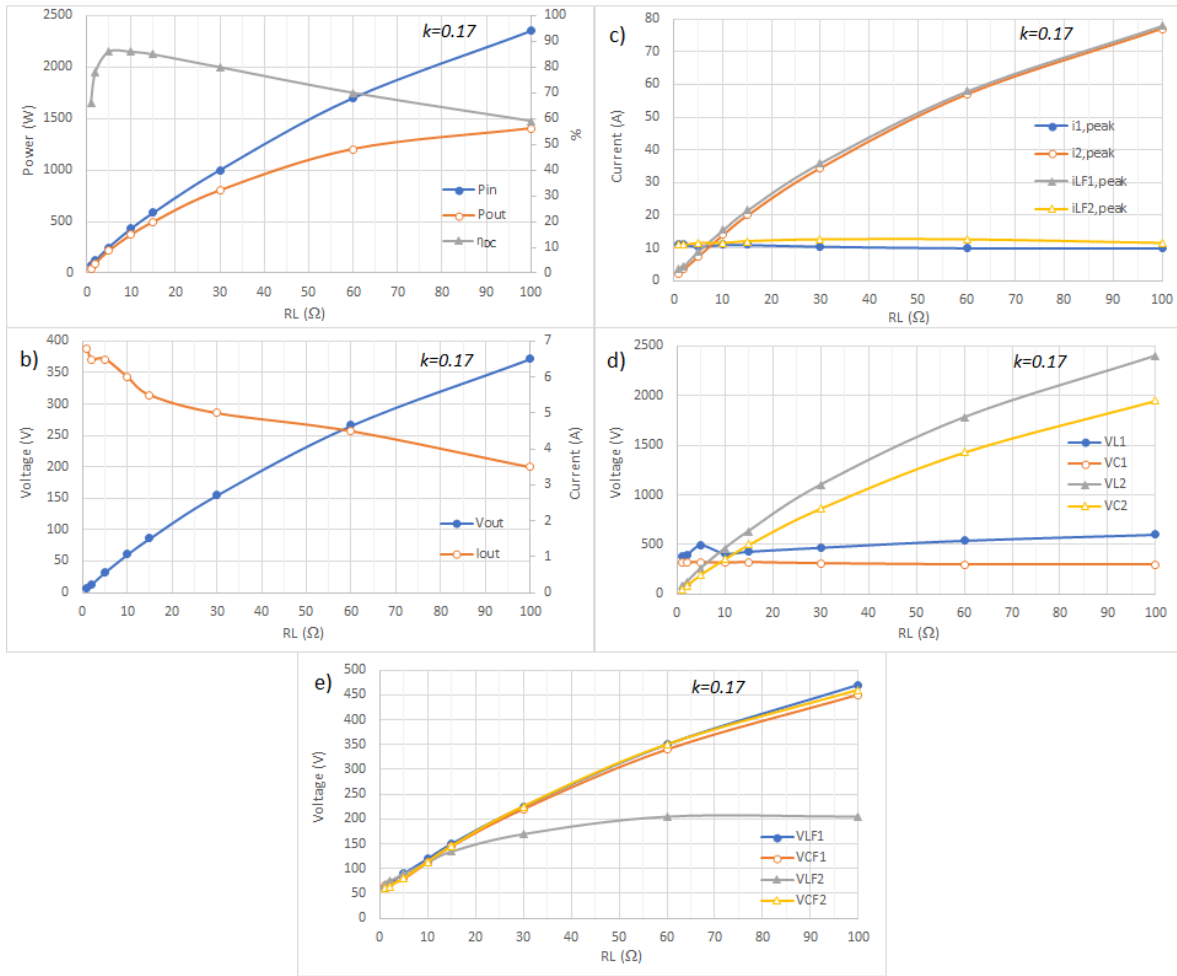


Figure 5.7: Simulation results of double-sided LCC system at  $k=0.17$ , depending on the load resistance  $R_L$ . Plot of a) DC input power  $P_{in}$ , DC output power  $P_{out}$  and efficiency  $\eta_{DC}$ , b) output voltage  $V_{out}$  and current  $I_{out}$  across  $R_L$ , c) peak current through  $L_1$ ,  $L_2$ ,  $L_{f1}$  and  $L_{f2}$ , d) peak voltage across  $L_1$ ,  $C_1$ ,  $L_2$  and  $C_2$ , e) peak voltage across  $L_{f1}$ ,  $C_{f1}$ ,  $L_{f2}$  and  $C_{f2}$ .

Table 5.1: Value of the parameters used in the circuit analysis.

Parameter	Value (Unit)
$f_0$	100 kHz
$V_{in}$	48 V
$R_1$	13 mΩ
$L_1$	55.6 μH
$C_1$	54.3 nF
$L_{f1}$	8.9 μH
$C_{f1}$	284.2 nF
$R_2$	24 mΩ
$L_2$	48.6 μH
$C_2$	63.8 nF
$L_{f2}$	8.9 μH
$C_{f2}$	284.2 nF

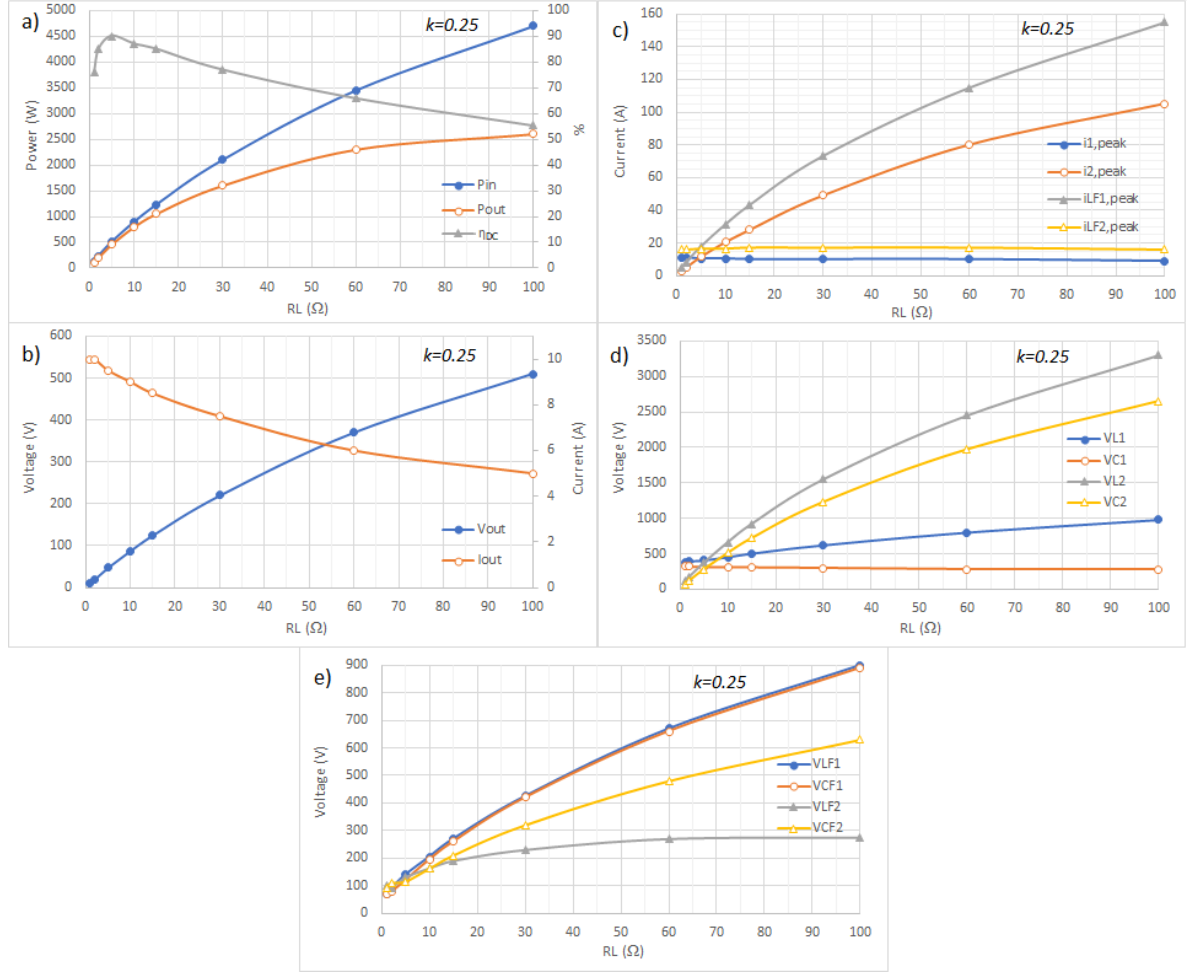


Figure 5.8: Simulation results of double-sided LCC system at  $k=0.25$ , depending on the load resistance  $R_L$ . Plot of a) DC input power  $P_{in}$ , DC output power  $P_{out}$  and efficiency  $\eta_{DC}$ , b) output voltage  $V_{out}$  and current  $I_{out}$  across  $R_L$ , c) peak current through  $L_1$ ,  $L_2$ ,  $L_{f1}$  and  $L_{f2}$ , d) peak voltage across  $L_1$ ,  $C_1$ ,  $L_2$  and  $C_2$ , e) peak voltage across  $L_{f1}$ ,  $C_{f1}$ ,  $L_{f2}$  and  $C_{f2}$ .

### 5.2.2. Results discussion of double-sided LCC compensation

The steady-state behavior of the WPT charging system with double-sided LCC compensation has been simulated at three different values of  $k$  and the results are shown in Figure 5.6, 5.7 and 5.8, depending on  $R_L$ . Three main considerations must be pointed out.

Firstly, the results show that this compensation circuit is acting as a current source as expected from the calculations. In fact,  $I_{Lf2}$  is constant at each coupling value. This fact makes the output voltage  $V_{ab}$  and  $V_{out}$  being directly proportional only to  $R_L$ . According to (3.29) and (3.32),  $I_{Lf1}$  and  $I_{L2}$  are also increasing when  $R_L$  increases, because they are directly dependent on  $V_{ab}$ . Therefore, for lower  $R_L$  values, the output power is low and it increases when  $R_L$  increases. The efficiency is not as high as with the S-S compensation, because extra components are added. The maximum efficiency achieved is  $\eta_{DC} = 90\%$  at  $k=0.25$  and  $R_L = 5 \Omega$ . The minimum efficiency achieved is  $\eta_{DC} = 55.5\%$  at  $k = 0.25$  and  $R_L = 100 \Omega$ . However, in this configuration the efficiency is not dropping too much at low  $k$  and high  $R_L$  values and overall it is more stable than in the S-S compensation.

Secondly, this system is working at fixed frequency and it could happen that it is not working at its required power level. In fact, plots of  $i_{1,peak}$  and  $i_{2,peak}$  in Figure 5.6, 5.7 and 5.8 do not show the effects of the bifurcation phenomenon for low values of  $R_L$ . However, in those points the power level of the system is much lower than the nominal one of 200 W, especially when the  $k$  is also low. So, even if the efficiency is higher than in the S-S compensation, the lower power level is a drawback.

Thirdly, the voltage and current stress on the  $L$ ,  $C$  resonant components are also investigated. In this system  $I_{L_{f1}}$  and  $I_{L_{f2}}$  are directly proportional to the coupling factor, so the voltage and current stress on the components increases as  $k$  increases. The filter inductances can be dimensioned according to the physical maximum  $k$  of the system, making the circuit intrinsically safe and a position detection system is not needed. The current stress on the component is similar to the one in the S-S compensation, but the voltage stress is almost half. However, in case the load is suddenly disconnected from the charging station,  $I_{L_{f2}}$  becomes zero but the rest of the circuit would still resonate as explained in [18]. So, there could be a considerable over voltage across  $C_{f2}$  and the capacitor could break down. To avoid this, an open-circuit protection is needed at the output of the secondary circuit, protecting  $C_{f2}$  from possible over voltages.

### 5.3. Comparison between LCC and S-S compensation

Finally, the double-sided LCC compensation is compared with the S-S compensation in Table 5.2, considering their performance in the e-bike WPT charging system.

The double-sided LCC compensation network cannot work at auto-resonant frequency, and the overall efficiency is also lowered, because of the extra component involved. Therefore, the S-S compensation network is chosen for the e-bike WPT charging system, since it can work at auto-resonant frequency, following naturally the resonance of the primary circuit for achieving ZCS operation.

Table 5.2: Comparison between double-sided LCC and S-S compensation circuits, in the e-bike WPT charging system.

		<b>LCC</b> (Figure 5.5)	<b>S-S</b> (Figure 5.1)
Frequency		Fixed	Auto-resonant
Inverter Control		AC frequency sweep	Zero-crossing detection
Dependency of $L$ , $C$ on $k$ and $R_L$ <sup>1</sup>		NO	NO
Number of $L$ and $C$ components		8	4
Stress on $L, C$ components	$I_L$ <sup>2</sup>	Moderate	Moderate
	$V_C$ <sup>3</sup>	Moderate	High
	$k \rightarrow 0$ <sup>4</sup>	$i_1, i_2 \rightarrow 0$ A	$i_1, i_2 \uparrow\uparrow$
	$R_L \rightarrow \infty$ <sup>5</sup>	$i_1, i_{L_{F2}} \uparrow\uparrow$ ; $i_{L_{F1}}, i_2 \downarrow$ $V_{L_{F2}}, V_{C_2}, V_{C_{F2}} \uparrow\uparrow\uparrow$	$i_1 \uparrow\uparrow$ ; $i_2 \downarrow$ $V_{L_1}, V_{C_1} \uparrow\uparrow$
$\eta_{DC}$ <sup>6</sup>		Lower, because of the extra $L, C$ components	Higher, because less $L, C$ components are used
Safety features needed <sup>7</sup>		Open-circuit protection	Position detection

<sup>1</sup> Referring to (3.3), (3.4), (3.24), (3.25), (3.26) and (3.27).

<sup>2</sup> Current stress on the inductors.

<sup>3</sup> Voltage stress on the capacitors.

<sup>4</sup> The coupling is lower than the allowed value, because of a large misalignment.

<sup>5</sup> The receiver is suddenly removed from the transmitter surface, causing the equivalent resistive load to be extremely large.

<sup>6</sup> The efficiency is calculated as in (5.8), at both the primary and secondary DC sides.

<sup>7</sup> **LCC**: in case the receiver is suddenly removed from the transmitter surface,  $I_{L_{F2}}$  drops to zero, but there would be still a resonant current flowing in the series  $L_2$ ,  $C_2$  and  $C_{F2}$  and causing a huge overvoltage across  $C_{F2}$ . An open-circuit detection system is needed, such that  $C_{F2}$  would not brake-down. **S-S**: In case  $k$  is lower than the minimum allowed value  $k_{min}$ , the primary and secondary current can increase considerably over their rated value, as shown in (5.1) and (5.4). A position detection system is needed, such that the power transfer does not start in case  $k < k_{min}$ .

## Power transfer control

In this Chapter, it is explained how the power transfer control can be realized through both the inner and outer control loops shown in Figure 6.1. Firstly, an introduction to the power transfer control is given in Section 6.1. Secondly, Section 6.2 discusses how the power transfer control is done at the nominal operating conditions. Thirdly, the inner control loop is explained in Section 6.3, showing in detail how the inverter works at auto-resonant frequency. Finally, several methods for realizing the outer control loop are explained in Section 6.4, which consist in adjusting the primary converter operation depending on the measured output power.

### 6.1. Power transfer control: introduction

The e-bike WPT charging system is divided into two main parts: the transmitter and the receiver, as shown in Figure 6.1. The transmitter is composed of the primary converters and the primary coil which is compensated in series by the primary capacitor. The receiver is composed of the secondary coil coupled to the primary coil and compensated in series by the secondary capacitor, the secondary converters, and the e-bike's battery. In Chapter 5, the operation of the primary full-bridge inverter has been chosen to be at auto-resonant frequency. This means that the inner control loop has to control the inverter such that it commutates the switching leg as the primary current crosses the zero. With this control strategy, unity PF and the ZCS operation are achieved. Moreover, the proper voltage level  $V_{in}$  at the inverter's input has to be set, such that the DC output power does not exceed its maximum rating. This control is called outer control loop.

The inner control loop is covered by the literature research, design and implementation, and the outer control loop by the literature research only, as it is shown by the red-dashed-line and green-double-line blocks in Figure 6.1.

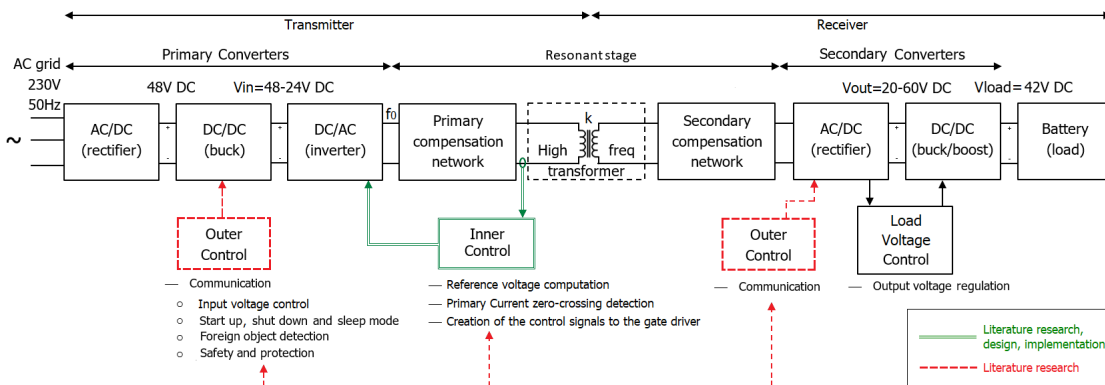


Figure 6.1: Block diagram of e-bike WPT charging system, highlighting the inner and outer control loops. The red-dashed-line blocks (outer control loop) are covered by literature research only and the green-double-line (inner control loop) blocks are covered by the literature research, design and implementation.

## 6.2. Nominal operating point

The nominal operating conditions of the e-bike WPT charging system must be known, such that the power transfer control can be design properly. Therefore, it is important that the inner and outer control loops can handle the operation at the nominal conditions without compromising the e-bike WPT charging system. These controls need to be able to handle the bifurcation in case it occurs. In [7] and [8], the bifurcation phenomenon is defined as the presence of multiple resonant frequencies in the circuit, which means that the imaginary part of  $Z_{in}$  is zero not only at the designed  $f_0$ , but also at those other frequencies. Since the primary inverter operates at auto-resonant frequency, the inner control loop would naturally follow the resonance and work at frequencies different than the design one  $f_0$ . However, because of the bifurcation phenomenon, the set operating point could have currents higher than the rated ones, making the power level exceed the nominal one. In this case, the outer control loop should change the input voltage of the primary inverter, such that the power level returns into the allowed range. The reason for the increase in the currents can be found from the equations of  $I_1$  and  $I_2$  at the resonant frequency  $f = f_0$ :

$$I_{2,peak} = \frac{\sqrt{2}V_{in}}{2\pi f_0 M} \quad (6.1)$$

$$I_{1,peak} = \frac{R_L}{2\pi f_0 M} I_2 = \frac{\sqrt{2}V_{in} R_L}{(2\pi f_0 M)^2} \quad (6.2)$$

Both  $I_1$  and  $I_2$  are inversely dependent on  $k$ . So, in case the coupling is low, the current value could increase significantly, but reducing the input voltage  $V_{in}$  could make  $I_1$  and  $I_2$  be within their rated values. Therefore, the inner control loop working at auto-resonant frequency needs to be combined with a outer control loop, that lowers  $V_{in}$  in case the measured power level is too high. A numerical example on the e-bike WPT charging system is present in Section 6.2.1.

### 6.2.1. Example on the e-bike WPT charging system

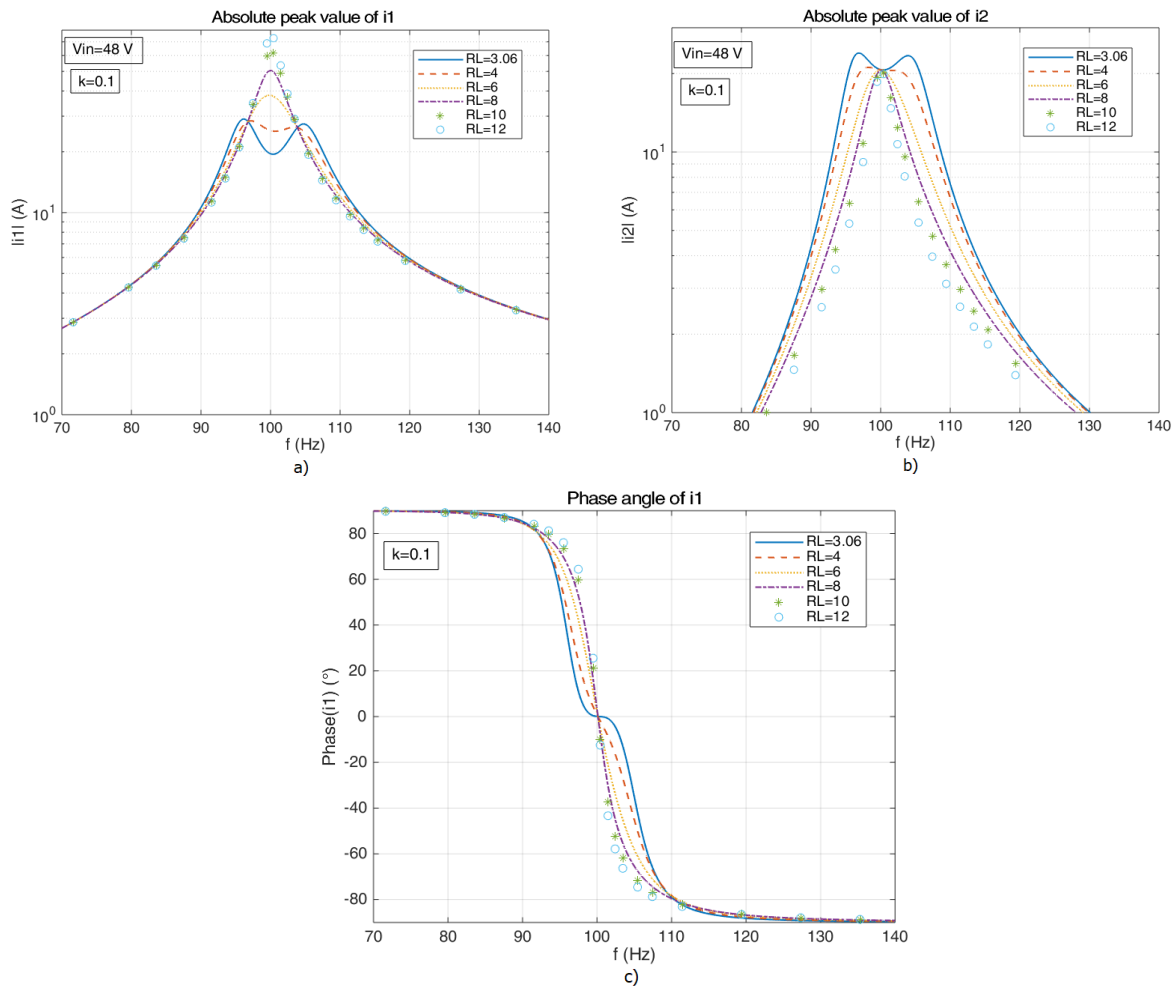
In the e-bike WPT charging system, the nominal load power is  $P_{load}^{(nom)} = 200$  W, with a nominal load voltage  $V_{load}^{(nom)} = 40$  V and a nominal load current  $I_{load}^{(nom)} = 5$  A. However, while the battery is charging the equivalent load is changing over the time and this makes  $V_{load}$  and  $I_{load}$  not constant. For this reason, a buck/boost converter is placed after the rectifying diode-bridge for regulating rectified voltage  $V_{out}$ , such that  $V_{load}$  is constant. Moreover, supposing that  $V_{out}^{(nom)}$  is allowed to swing in the range 20-60 V for having always enough voltage to power the buck/boost gate driver and that  $I_{out}^{(nom)} = 5$  A, the equivalent load at the nominal operation is  $R_L^{(nom)} = 4-20 \Omega$ .

The inner and outer control loops must be able to work in the nominal load range  $R_L^{(nom)} = 4-20 \Omega$  and at the allowed coupling factor range  $k = 0.1-0.25$ . For understanding these nominal operating conditions, an AC analysis of  $i_1$  and  $i_2$  is executed in the load range  $R_L^{(nom)} = 4-20 \Omega$  and at  $k = 0.1, 0.17, 0.25$ . Figure 6.2, 6.3 and 6.4 show the plots of  $I_1$ ,  $I_2$  absolute value and the phase angle of  $i_1$  at  $k = 0.1, 0.17$  and  $0.25$ , respectively. According to the definition of bifurcation found in [7], the minimum resistive load which gives a bifurcation-free operation can be calculated through equation 3.19. The resulting  $R_{L,min}$  at each  $k$  are reported in Table 6.1. The plots of Figure 6.2, 6.3 and 6.4 contain the calculated  $R_{L,min}$ . Table 6.1 shows that the bifurcation phenomenon is present at the nominal load range  $R_L = 4-20 \Omega$  when the coupling is high. In fact, at the minimum coupling factor  $k = 0.1$ ,  $R_{L,min} = 3.06 \Omega < 4 \Omega$  which means that there is no bifurcation. On the other hand, at the maximum coupling factor  $k = 0.25$ ,  $4 \Omega < R_{L,min} = 7.7 \Omega < 20 \Omega$ . The boundary of the bifurcation is inside the nominal operating conditions.

Considering the case with the highest  $k$  and  $V_{in} = 48$  V the nominal condition, the maximum peak values of  $I_1$  and  $I_2$  in that case are taken as references, and they are compared to the ones with  $k = 0.1$  and  $0.17$ , in Table 6.2. The maximum peak values of  $I_1$  and  $I_2$  are considered at both bifurcation and bifurcation-free operation. The values at  $V_{in} = 48$  V are taken according to Figure 6.2, 6.3 and 6.4. The values at  $V_{in} < 48$  V are reported for lower  $k$ , but the plots are not shown in this report.

Table 6.1: The resulting  $R_{L,min}$  boundary of the bifurcation, at each  $k$  are reported.

$k$	$R_{L,min}$
0.1	$3.06 \Omega$
0.17	$5.22 \Omega$
0.25	$7.7 \Omega$

Figure 6.2: AC analysis at  $V_{in} = 48 \text{ V}$ ,  $k=0.1$  of: a) absolute peak value of  $I_1$ , b) absolute peak value of  $I_2$ , c) phase angle of  $I_1$ .

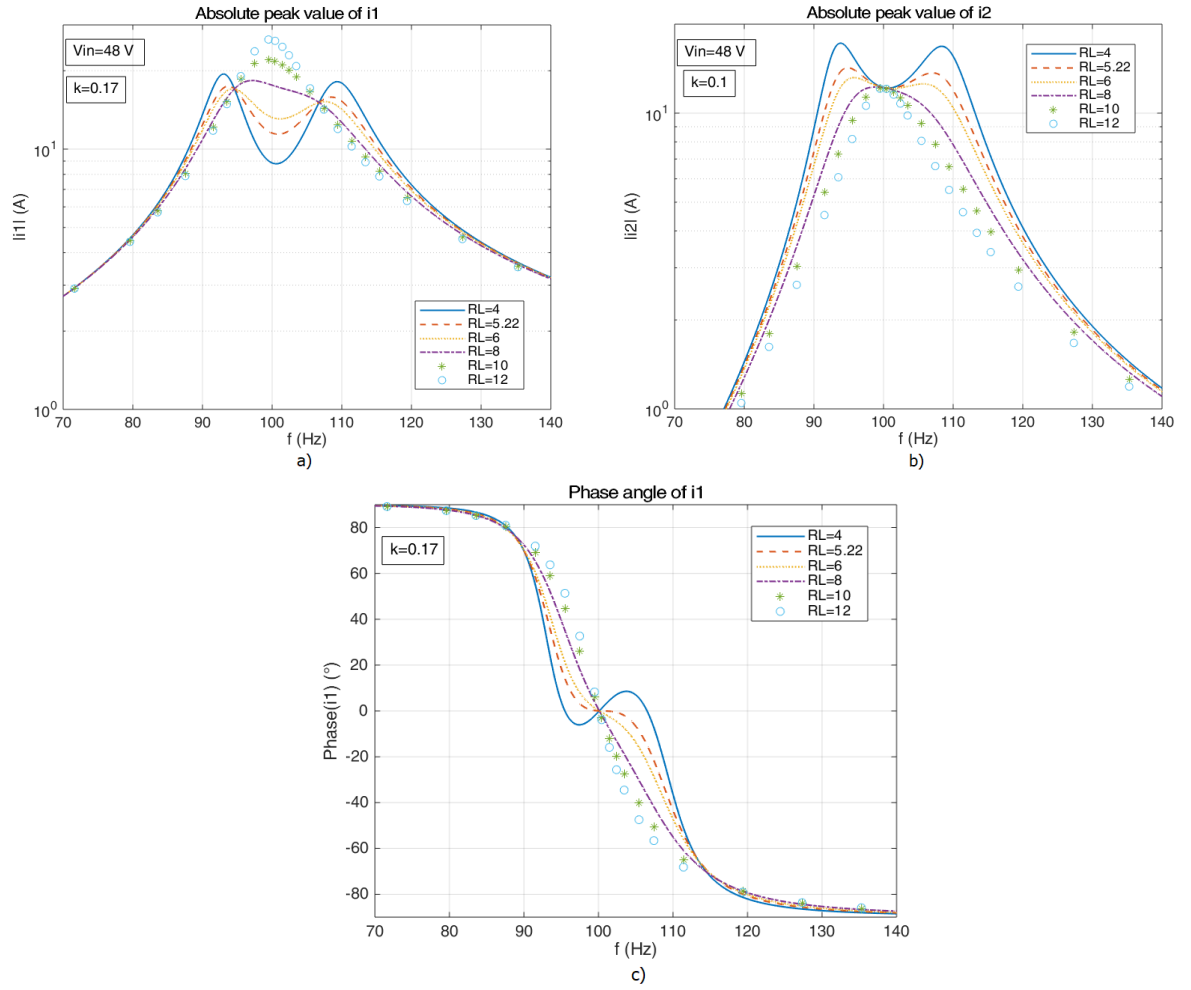


Figure 6.3: AC analysis at  $V_{in} = 48\text{ V}$ ,  $k = 0.17$  of: a) absolute peak value of  $I_1$ , b) absolute peak value of  $I_2$ , c) phase angle of  $I_1$ .



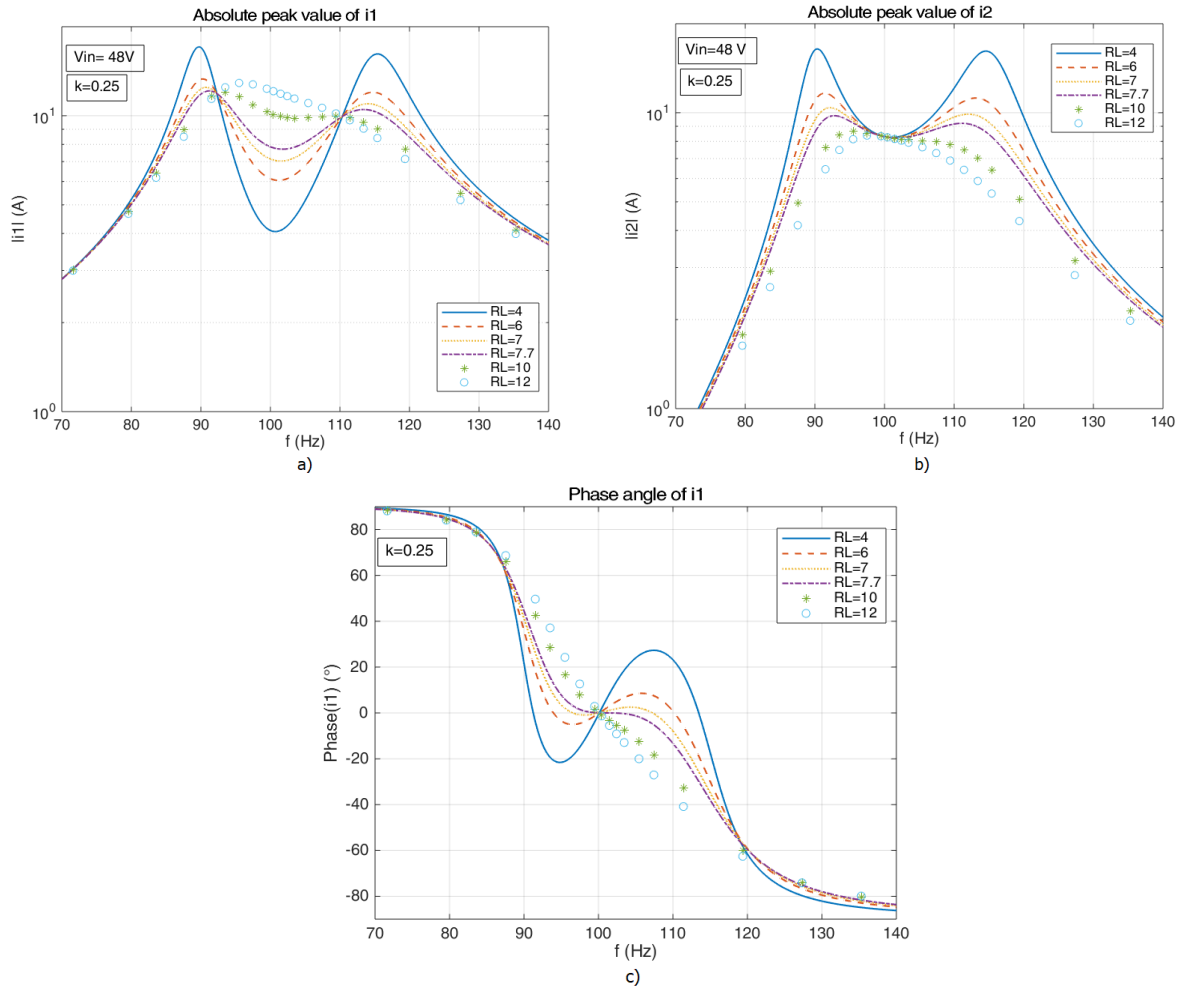


Figure 6.4: AC analysis at  $V_{in} = 48\text{ V}$ ,  $k=0.25$  of: a) absolute peak value of  $I_1$ , b) absolute peak value of  $I_2$ , c) phase angle of  $I_1$ .

Table 6.2:  $I_{1,max}$  and  $I_{2,max}$  peak values at  $k=0.1$ ,  $0.17$  and  $0.25$ , distinguishing the cases with bifurcation and with a bifurcation-free operation. The nominal operation at the highest  $k$  and  $V_{in} = 48\text{ V}$  is taken as reference.

$k$	$V_{in}$ (V)	$I_{1,max}$		$I_{2,max}$	
0.25	48	$I_{1,max,bif}^{(nom)} = a$	$I_{1,max,bif-free}^{(nom)} = b$	$I_{2,max,bif}^{(nom)} = c$	$I_{2,max,bif-free}^{(nom)} = d$
0.17	48	$a$	$1.7 \cdot b$	$1.4 \cdot c$	$1.5 \cdot d$
0.17	32	$0.7 \cdot a$	$0.7 \cdot b$	$1.3 \cdot c$	$d$
0.1	48	-	$4.6 \cdot b$	-	$2.5 \cdot d$
0.1	18	-	$1.7 \cdot b$	-	$d$
0.1	10	-	$b$	-	$0.5 \cdot d$

Even though the bifurcation phenomenon is not present at low value of  $k$ , the maximum peak value

of  $I_1$  and  $I_2$  becomes respectively 4.6 and 2.5 times higher than in the case of maximum  $k$ . Therefore, both the bifurcation and the low coupling factor increase the power level, and the outer control loop must work in combination with the inner control loop for lowering the input voltage  $V_{in}$  of the inverter. This is a qualitative description of the inner control loop, its detailed design is present in Chapter 8.

### 6.3. The inner control loop

The inner control loop consists in the control for achieving the operation with auto-resonant frequency of the full-bridge inverter, such that it is working at ZCS following the resonance of the primary circuit. The inner control loop is composed of three main blocks as shown in Figure 6.5: the reference voltage computation block, the  $i_1$  zero-crossing detection block and the creation of the gating control signals  $Q$  and  $\bar{Q}$  block, which are explained in Section 6.3.1, 6.3.2 and 6.3.3, respectively. Moreover, the inner control loop is covered by the literature research, design and implementation. The literature research is done in this section, the design is explained in Section 8 and the verification of the theoretical model using a developed prototype is in Chapter 9.

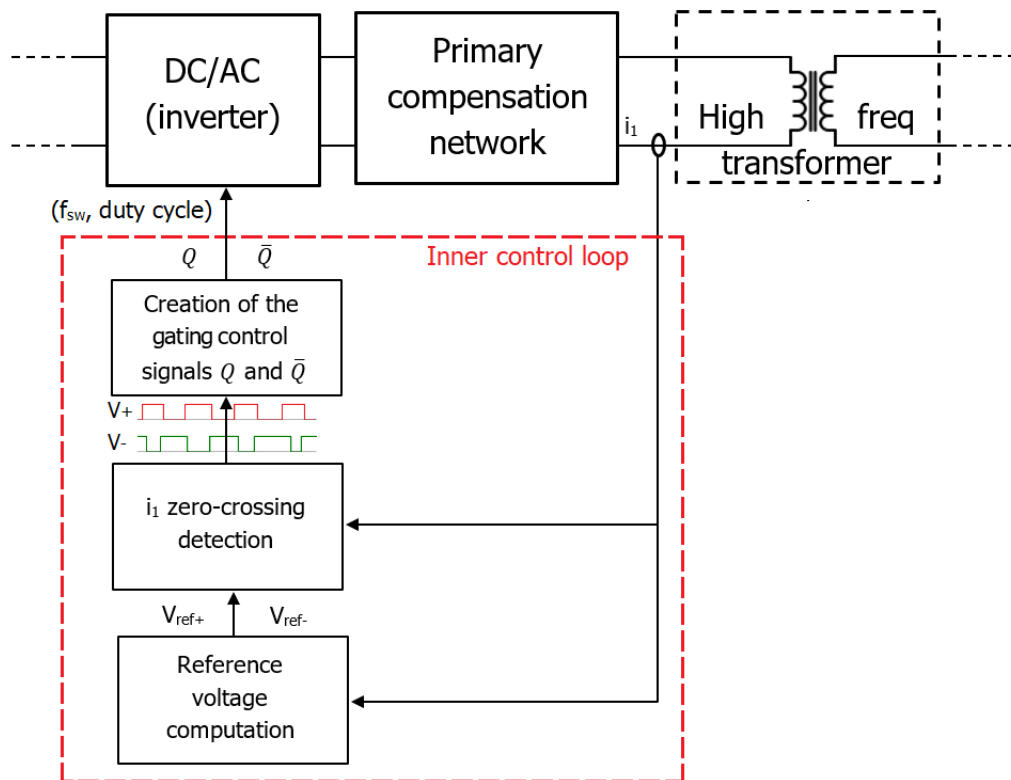


Figure 6.5: Comparator for zero-current detection.

#### 6.3.1. Reference voltage computation block

The first block of the inner control loop is the reference voltage computation block. In this block, the reference voltages  $V_{ref+}$  and  $V_{ref-}$  are computed for detecting the zero-crossing of  $i_1$ .

Ideally the zero-crossing of  $i_1$  could be detected comparing the current waveform to the ground (0 V reference) and commutating at that moment the switch leg of the inverter. However, in a real circuit, all the ICs and the gate driver introduce some delay in the control signal, which would make the commutation happen at finite current. As an example, the delay in the zero-crossing detection is shown qualitatively in Figure 6.6.  $\Delta t$  represents the total time delay, and it can be expressed as the sum of three main delays in the inner control loop:

$$\Delta t = \Delta t_1 + \Delta t_2 + \Delta t_3 \quad (6.3)$$

in which  $\Delta t_1$  is the delay caused by the opamps,  $\Delta t_2$  is the delay caused by the comparators and  $\Delta t_3$  is the delay caused by the gate driver. Therefore,  $\Delta t$  is mainly constant and it depends on the design of the control loop. The inner control loop of the e-bike WPT charging system has a  $\Delta t \approx 800 \mu\text{s}$ .

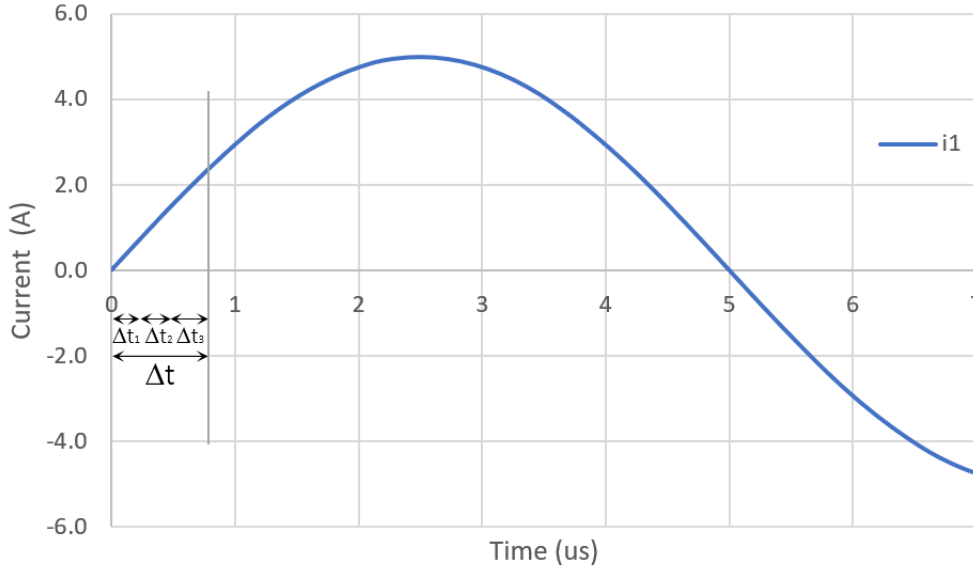


Figure 6.6: Delay in the zero-crossing detection due to the ICs and gate driver delays.

According to Figure 6.6, in case the ground is taken as a reference voltage the actual commutation would happen at  $t = \Delta t$  and the operation would not be at ZCS. Therefore, for having the commutation at exactly the zero-crossing of  $i_1$ , the reference voltage should have a negative value. In this way, it is possible to compensate for the delay time  $\Delta t$  and having the commutation at  $t = 0$  s. Moreover, since the resonant oscillations are not exactly sinusoidal, the positive and negative half-wave of  $i_1$  could be not symmetrical. So, it is preferable having two independent reference voltages, one for the positive slope and the other one for the negative slope of  $i_1$ , which are called  $V_{ref+}$  and  $V_{ref-}$  respectively.

The reference voltage computation block computes the reference voltages  $V_{ref+}$  and  $V_{ref-}$  for detecting the zero-crossing of  $i_1$ . The main idea is to find a relation between the slope of  $i_1$  at the zero-crossing and the  $V_{ref}$  that gives ZCS. The slope of  $i_1$  is described by its time derivative  $di_1/dt$ , and it is not constant. In fact, it depends on the amplitude of  $i_1$  and on the operating frequency  $f_0$ . An example of  $di_1/dt$  depending on the  $i_1$  amplitude is shown in Figure 6.7, where  $i_1$  is a sinusoid and the operating frequency is constant at  $f_0 = 100$  kHz. The current is varying from 1 to 4 A and also the  $di_1/dt$  is varying sensibly. Moreover, the part of  $i_1$  close to the zero-crossing can be considered linear and consequently its derivative is a constant value, which depend on the slope of that line. In case the operating frequency is fixed,  $V_{ref}$  could be simply depending on the amplitude of  $i_1$ . However, since the inner control loop is working at auto-resonant frequency, the operating frequency is not fixed and, for the same amplitude, the slope at the zero-crossing could be completely different depending on the duration of the period. Therefore, it is chosen to find the dependence of  $V_{ref}$  on  $di_1/dt$  at the zero-crossing; in particular, the dependence of  $V_{ref+}$  on  $i_1$  positive slope ( $di_1/dt > 0$ ), and  $V_{ref-}$  on  $i_1$  negative slope ( $di_1/dt < 0$ ).

For this purpose, this block is composed of three main sub-blocks as shown in Figure 6.8. The first sub-block consists in the  $i_1$  measurement and its conditioning, which gives as output the voltage  $V_{i1,B}$ . The voltage  $V_{i1,B}$  goes through the second sub-block, which consists in its differentiation at the zero-crossing for both the positive and negative slopes, called  $(dV_{i1,B}/dt)_+$  and  $(dV_{i1,B}/dt)_-$  respectively. The third sub-block is the function that has  $(dV_{i1,B}/dt)$  as input and gives  $V_{ref}$  as output, which is implemented independently for both the positive and negative slope of  $i_1$ . The gain and the offset of this function are discussed in detail in Section 8.1.

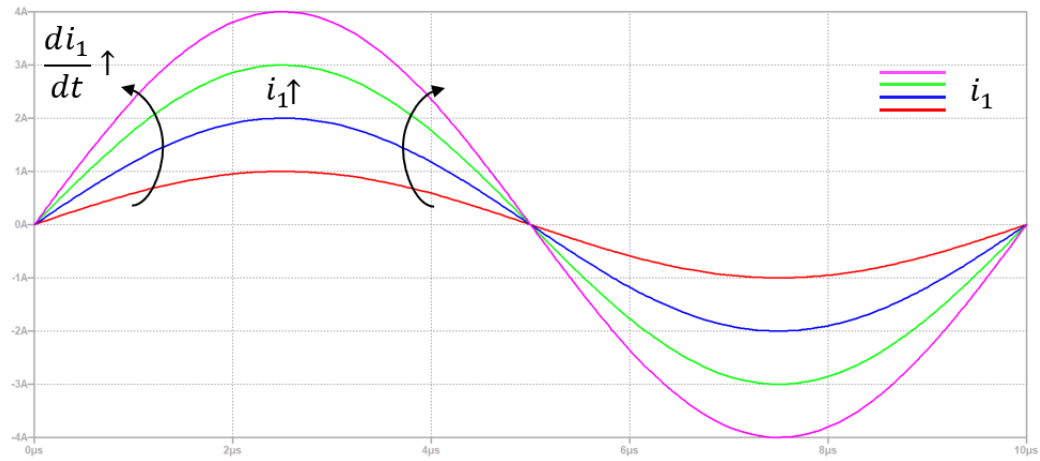


Figure 6.7: Example of different  $\frac{di_1}{dt}$ , in which the frequency is fixed and the parameter changing is the current amplitude. However, the frequency could also change because of the auto-resonant frequency operation.

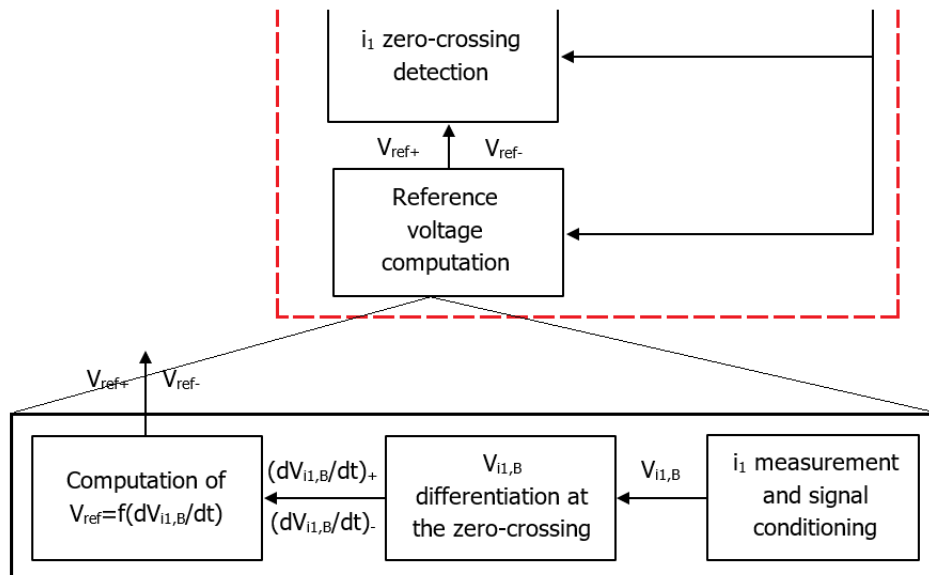
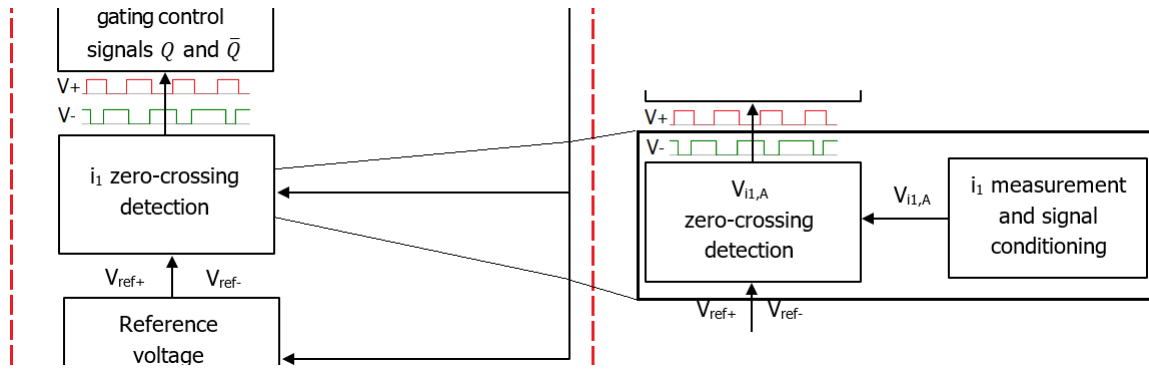


Figure 6.8: Sub-blocks of the reference voltage computation block.

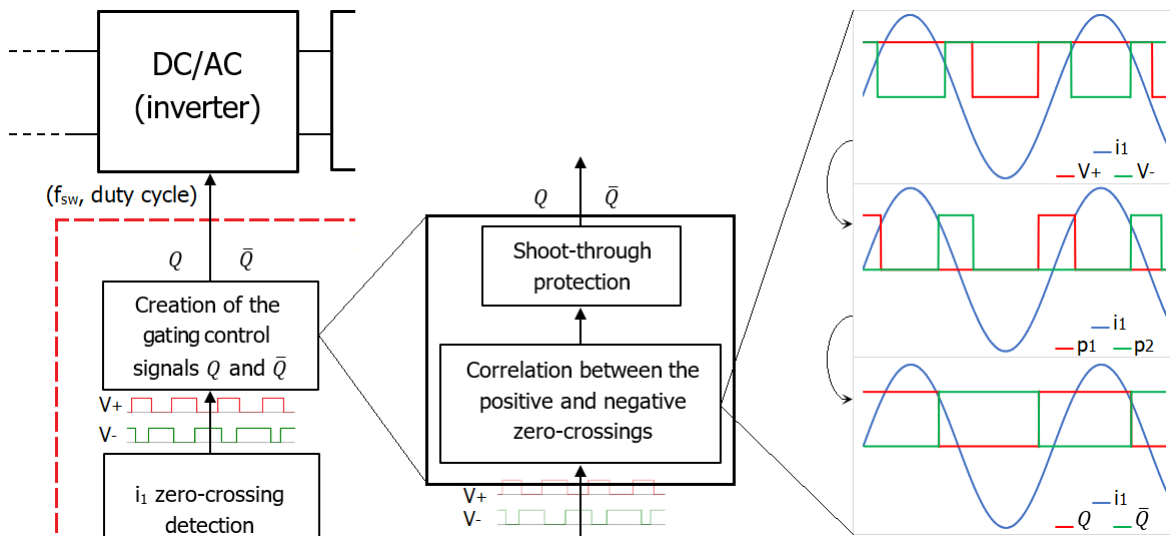
### 6.3.2. $i_1$ zero-crossing detection block

The second block of the inner control loop is the  $i_1$  zero-crossing detection block. This block compares the  $i_1$  with the input reference values and gives a high output (+5 V) when  $i_1$  is greater than the reference. Otherwise, it gives a low output (0 V). This block is composed of two main sub-blocks as shown in Figure 6.9. The first sub-block consists in the  $i_1$  measurement and its conditioning, which includes a second-order low-pass filter and it gives as output the voltage  $V_{i1,A}$ . Then,  $V_{i1,A}$  goes through the zero-crossing detection block, which is the second sub-block. This block compares the positive slope of  $V_{i1,A}$  with  $V_{ref+}$  and the negative slope of  $V_{i1,A}$  with  $V_{ref-}$ , that give respectively the square wave outputs  $V_+$  and  $V_-$ . The two square wave outputs are completely independent of each other, and they are the inputs of the third block of the inner control loop.

Figure 6.9: Sub-blocks of the  $i_1$  zero-crossing detection block.

### 6.3.3. Creation of the gating control signals $Q$ and $\bar{Q}$ block

The third block of the inner control loop is the creation of the gating control signals  $Q$  and  $\bar{Q}$  block. This block is composed of two main sub-blocks as shown in Figure 6.10. The first sub-block correlates the two square wave signals  $V_+$  and  $V_-$  coming from the positive and the negative zero-crossing detection, such that the control signal to the gate driver is unique. The right part of Figure 6.10 shows qualitatively how  $V_+$  and  $V_-$  can be correlated to each other. At first,  $V_+$  and  $V_-$  are independent of each other, and they overlap in some parts. However, since  $V_+$  control the positive zero-crossing and  $V_-$  controls the negative zero-crossing, the short pulses  $p_1$  and  $p_2$  are created from  $V_+$  and  $V_-$ , which are focused just on the zero crossing of  $i_1$ . Then, the high value of  $p_1$  and  $p_2$  are extended, such that both of them switch to the low value as soon as the other one goes to the high value. The second sub-block is the shoot-through protection that makes sure that the controls sent to the two switching legs are not overlapping such that there are no short circuits in the full-bridge inverter. Finally, the outputs of this block are  $Q$  and  $\bar{Q}$ , which control the gate driver of the full-bridge.

Figure 6.10: Sub-blocks of the creation of the gating control signals  $Q$  and  $\bar{Q}$  block.

## 6.4. Outer control loop

The outer control loop consists in adapting the input power at the primary side, depending on the measured output power as shown in Figure 6.1. In fact, in Section 6.2 it is discussed that the secondary current could be high causing an output power greater than the rated one, because of either the bifurcation phenomenon or low values of  $k$ .

In this section some methods for controlling the output power level are discussed, compared, and the most suitable one for the charging application is chosen. As it is explained in [15], the control of the output power can be done either by phase shifting the primary current or changing the DC-link voltage at the inverter input or commuting the inverter legs any other 3/5 zero crossing of the primary current. All these methods are discussed singularly in Section 6.4.1, 6.4.2 and 6.4.3, respectively. Moreover, the outer control loop is covered only by the literature research in this section. The design and implementation of the outer control loop are not part of this project.

### 6.4.1. Phase shifting

The output power level can be controlled by changing either the duty cycle or the operating frequency of the primary inverter. This can be done by commuting the inverter's leg at finite current, reducing the average input power. However, this method does not provide ZCS operation, and the hard switching could cause considerable losses in the switches if the turn-off current is high. Moreover, the PF at the primary side is not unity, since the primary voltage and current are not in phase.

Considering that the operation of the inverter is chosen to be at auto-resonant frequency and ZCS, this method is not suitable for this application, but it could be applicable to fixed-frequency operations.

### 6.4.2. Input DC-link voltage control

The output power level can be controlled by changing the DC-link input voltage. Considering the basic S-S compensated circuit at the resonant frequency, the secondary current is directly dependent on the square wave voltage  $V_{AB}$ , such that

$$I_2 = \frac{V_{AB}}{2\pi f_0 M} \quad (6.4)$$

where  $V_{AB}$  is just the inverted DC input voltage  $V_{in}$ . So, if the secondary current is higher than its rated value,  $V_{in}$  can be stepped-down for decreasing the output power.

The most straightforward way to lower  $V_{in}$  is inserting at the input of the full-bridge inverter a buck converter as shown in Figure 6.11. In this way, the square wave voltage  $V_{AB}$  at the output of the full-bridge can be adapted in a wide range to achieved the desired output current.

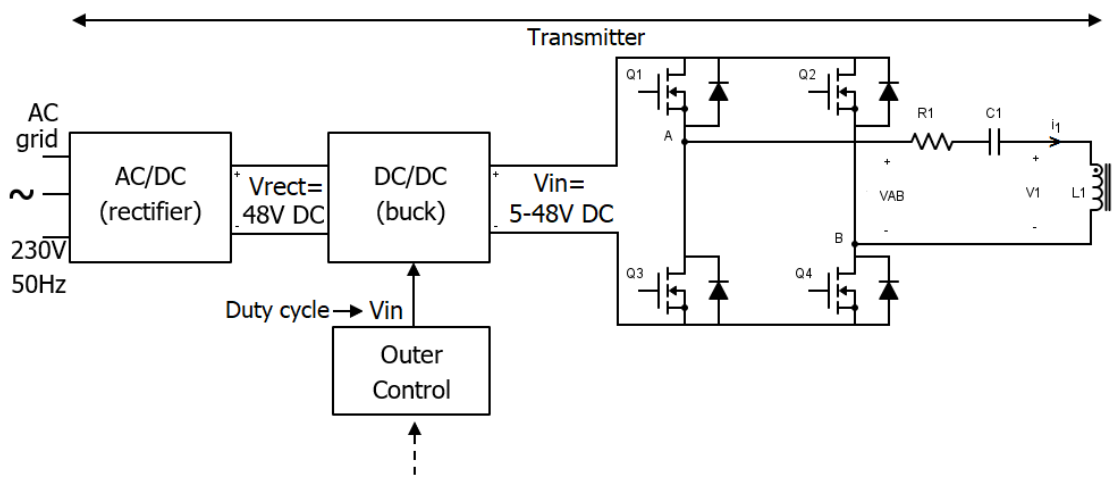


Figure 6.11: DC/DC buck converter that changes the input voltage  $V_{in}$  of the inverter.

For lowering  $V_{in}$ , the full-bridge and the half-bridge topologies could be combined in one inverter. The inverter could work as a full-bridge when the maximum full  $V_{in}$  is needed, and as an half-bridge

when less power is required and just half of  $V_{in}$  is need. This combined full/half-bridge inverter can be realized introducing in a full-bridge two input capacitors  $C_{in}$  that keep constant half of  $V_{in}$  and adding one switch between the mid-voltage point and B, as shown in Figure 6.12.

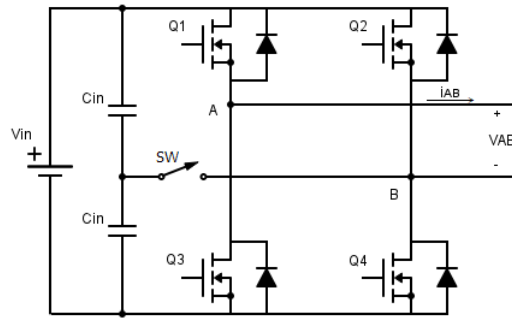


Figure 6.12: Combination of HB and FB inverter.

Moreover, the control strategy for this inverter is reported in Table 6.3.

Table 6.3: Switching table of the HB/FB combined inverter, in Figure 6.12.

$V_{AB}$	FB $\pm 48$					HB $\pm 24$				
	$SW$	$Q_1$	$Q_2$	$Q_3$	$Q_4$	$SW$	$Q_1$	$Q_2$	$Q_3$	$Q_4$
$i_{AB} > 0$	0	1	0	0	1	1	1	0	0	0
$i_{AB} < 0$	0	0	1	1	0	1	0	0	1	0

1=Switch close 0=Switch open

This solution introduces less components than the one using the buck converter. However, programming the control is definitely more complex because it involves all independent gate drivers. This full-bridge half-bridge combined inverter allows to invert either the full or half input voltage and not voltage levels in between. One example of this input voltage control strategy is shown in the waveforms of Figure 6.13, in which are plotted the absolute value of the inverted voltage  $|V_{AB}|$ ,  $V_{out}$  and  $I_{out}$  at  $k = 0.25$  and  $R_L = 4 \Omega$ . During the first  $250 \mu s$  the inverter working in the start-up mode. Therefore, it is operating at fixed frequency and in the full-bridge configuration, giving  $|V_{AB}| = V_{in} = 48 V$ . Then, it starts the operation at auto-resonant frequency and  $I_{out}$  jumps from 5 to 10 A because of the bifurcation phenomenon. At  $t = 700 \mu s$ ,  $I_{out}$  is measured and the inverter starts working in the half-bridge configuration  $V_{AB}$  giving  $|V_{AB}| = V_{in}/2 = 24 V$ , because  $I_{out}$  its rated value. With the inverter working in half-bridge configuration  $V_{out}$  and  $I_{out}$  reach values in the permitted range 20-60 V and 2-8 A.

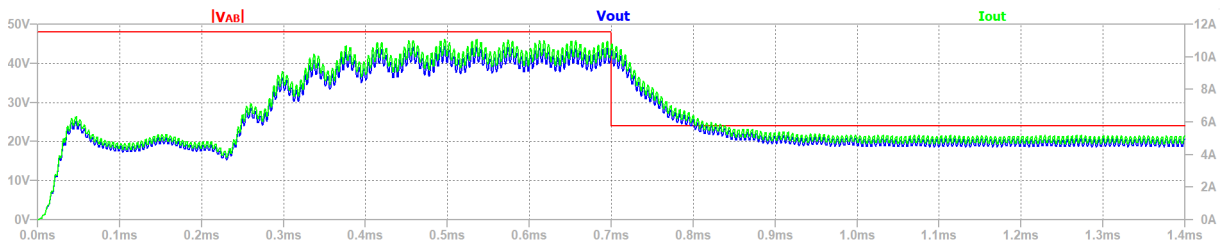


Figure 6.13: Start-up simulated waveforms for  $V_{in} = 48 V$ ,  $k = 0.25$  and  $R_L = 4 \Omega$ , using the combined HB/FB inverter.

### 6.4.3. Switching at a multiple of the resonant frequency

The output power level can be lowered by commuting the switching leg of the full-bridge inverter any other three oscillations of the resonant current instead of at every zero crossing. The switching losses are reduced to 1/3, simply because the switching is happening every other three oscillations. Then, the primary current produces real power with the third harmonic of the inverted voltage, which is three times lower than  $V_{AB}$ . Therefore, the power level at the primary circuit is also reduced to 1/3 of its original value. Depending on the desired voltage level, it can be decided to switch every 3, 5 or any odd number of oscillations. However, it must be taken into account that if the damping of the oscillations is high, the resonance could be damped to zero before the next commutation and power transfer would be lost. One example of this outer control strategy is shown in Figure 6.14, in which  $V_{AB}$  and  $I_1$  are plotted at the top and  $V_{out}$  and  $I_{out}$  are plotted at the bottom, for  $V_{in}$ ,  $k = 0.1$  and  $R_L = 12 \Omega$ .

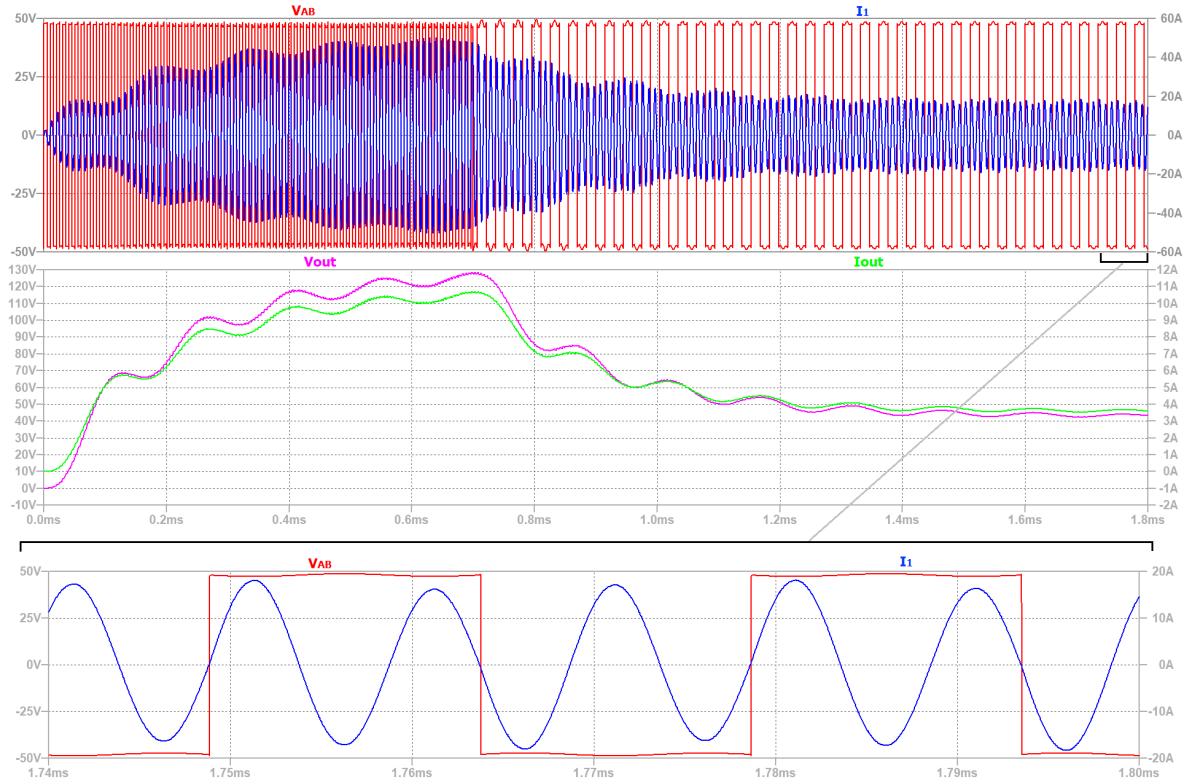


Figure 6.14: Simulated waveforms at the inverter start-up for  $V_{in} = 48 \text{ V}$ ,  $k = 0.1$  and  $R_L = 12 \Omega$ , commuting the inverter any other 3 primary current oscillations for reducing the output power.

During the first  $250 \mu\text{s}$ , the start-up at fixed-frequency and at  $|V_{AB}| = 48 \text{ V}$  is shown. Then, it starts the operation at auto-resonant frequency and  $I_{out}$  jumps to 10 A because of the effect of the low coupling on  $i_2$  as shown in Figure 6.2 b). At  $t = 700 \mu\text{s}$ ,  $I_{out}$  is measured and, since it exceeds the rated value of 8 A, the inverter starts commuting switch leg every 3 oscillations of  $I_1$ . In this way,  $V_{out}$  and  $I_{out}$  start decreasing, reaching values in the permitted range 20-60 V and 2-8 A.

### 6.4.4. Outer control loop selection

The outer control loop for regulating the output power can be made either by phase shifting the primary current or changing the DC-link voltage at the inverter input or commuting the inverter legs any other 3/5 zero crossing of the primary current. Considering that the inverter is operating at auto-resonant frequency and ZCS following the primary circuit resonance, the most suitable solutions are either changing the DC-link voltage at the inverter input or commuting the inverter legs any other 3/5 zero crossing of the primary current. However, in this project, only the literature study is executed on the outer control loop, and there is no design or implementation of it



## Communication between primary and secondary converters

This Chapter covers the literature research on the communication between the primary and secondary converter of the e-bike WPT charging system, via the outer control loop as shown in Figure 7.1. Firstly, an overview of the existing communication standard for WPT is given in Section 7.1. Secondly, the general characteristics of the Qi specification are explained in Section 7.2. Finally, the useful features of the Qi specification for the e-bike WPT charging system are discussed in Section 7.3.

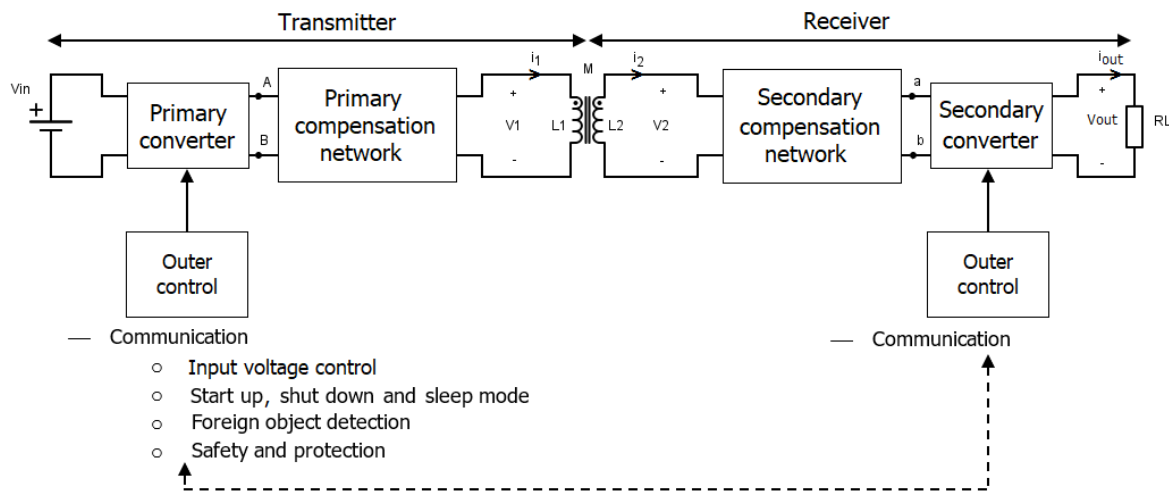


Figure 7.1: Communication between the primary and secondary converter of the e-bike WPT charging system, via the outer control loop.

### 7.1. WPT communication standards

In the last decade, the WPT has become interesting for charging electronics consumer products, causing the need for a standard for WPT. In 2008, the first WPT standard organization was founded, with the name of Wireless Power Consortium (WPC), which provides the Qi specification. In 2012, other two WPT standard organizations were born as an alternative to the Qi specification: Power Matters Alliance (PMA) and Alliance for Wireless Power (A4WP). In 2015 PMA and A4WP were merged, and now they are part of the same organization, called AirFuel Alliance. Nowadays, both organizations develop standards for both resonant and inductive WPT. According to [19], a comparison between the specifications is reported in Table 7.1.

Most of the consumer products found on the market use the Qi specification, but so far it can be applied to power levels  $\leq 15$  W. However, because the WPT charging is gaining more and more popularity,

the next version of the Qi specification (v1.3) is going to threat resonant power transfer and probably higher power levels, as stated in [20].

The Qi specification is the most suitable for the e-bike WPT charging system, even if its power level is 200 W, that is more than ten times higher than the one of the Qi specification. The two main reasons are that the operating frequency  $f_0 = 100$  kHz is within the range of 87-205 kHz and that it supports communication through the power line, which is the best for the e-bike WPT charging system in Figure 7.1. Therefore, just the Qi specification is covered in the following sections of this chapter.

Table 7.1: Comparison between WPT standards.

	WPC	Air Fuel Alliance	
Standard	Qi v1.2	PMA	(A4WP) Rezence
Since	2008	2012	2012
Technique	Inductive coupling	Inductive coupling	Resonant coupling
Operating Freq	87~ 205 kHz	201~ 304 kHz	6.78 MHz
Maximum Power	15 W	5 W	50 W
Communication	ASK/FSK	ASK	Bluetooth 2.4 GHz
Coupling	Tightly	Tightly	Loosely
Z-distance	$\leq 7$ mm	$\leq 5$ mm	$\leq 50$ mm
Charging Device	Single	Single	Multiple
System Eff (%)	60~ 80 %	60~ 80 %	40~ 70 %
Key Members	NXP, Bosch, ROM, Samsung, LG, Nokia, Panasonic, Philips, Qualcomm, RICHTEK, Apple Inc. MediaTek, Google ConvenientPower, Texas Instrumets, Toshiba, ST, htc	Duracell Powermat, Qualcomm, Google, INTEL, DELL, AT&T, Broadcom, Starbucks, RICHTEK, Samsung Huawei Technologies Co., ST, Sony Mobile Communications, ON Semiconductor	

## 7.2. Qi version 1.2.3

The most recent standard of the WPC, available for public download, is the Qi version 1.2.3 of February 2017. This version of the specification extends the maximum power rating from 5 W to 15 W and it increases the sensitivity of the Foreign Object Detection (FOD).

The specification is composed of four documents, as described in [21]:

1. *Introduction to Power Class 0 Specification.*
2. *Parts 1 and 2: Interface Definitions:*
  - *Part 1: Primary Interface Definition;* the interface between the power transmitter and the power receiver, including mechanical, power, thermal, and information interfaces;
  - *Part 2: Secondary Interface Definition;* the interface between the system and its environment, including the external power source, object detection, and the user interface.
3. *Part 3: Compliance Testing;* tests required for Qi registration (restricted-access document);
4. *Part 4: Reference Designs;* power transmitter and power receiver design examples.

In this section, the main features of parts 1 and 2 are explained, according to [22].

### 7.2.1. Operation sequence

The Qi specification describes the operation sequence for the communication between the Power Transmitter (PTx) and the Power Receiver (PRx), such that the WPT is executed correctly.

In case the application supports the FOD feature (mandatory in case of power levels > 5 W), the complete operation sequence is divided in seven phases, which are shown schematically in Figure 7.2.

1. *Selection.* In this phase, the PTx is not delivering any power, but it is in standby/sleep mode. Once an object is detected on the surface of the PTx, it measures the actual quality factor  $Q_{meas}$  sending a small amount of power, such that the PRx is not activated. Then, the Ping phase starts.
2. *Ping.* In this phase, the PTx sends a digital pulse with enough energy to activate the PRx. In case either no response is sent by a PRx or no power is needed, the process is quit, and it goes back to the *Selection* phase. On the other hand, if a PRx is present, and it sends to the PTx a correct Signal Strength Packet, the process continues to the *Identification & Configuration* phase.
3. *Identification & Configuration.* In this phase, the PTx receives the Identification and Configuration Packets. In case these packets are both correct and in the right order, the PTx creates a temporary copy of the Power Transfer Contract, that contains: the Guaranteed Power, the Maximum Power, the Received Power Packet and the Modulation Depth. The PRx can also require the *Negotiation* phase, and in case the PTx accepts it, that is going to be the next phase. For a power level  $\leq 5$  W the *Negotiation* is not compulsory, and the process can continue directly to the *Power Transfer* phase. If some errors occur in this phase, the process is sent back to the *Selection* phase.
4. *Negotiation.* In this phase, the PRx can ask the PTx to update or change something in the Power Transfer Contract. The request packets can have different characteristics, and the most important one is the FOD Status Packet. In fact, in that packet, the PRx sends the reference value  $Q_{ref}$  to the PTx, which compares it with the measured  $Q_{meas}$ . In case the difference between the two values is greater than a certain threshold, a foreign object is present on the PTx surface, the process is quit and sent back to the *Selection* phase. On the other hand, if the two quality factors are similar, the process goes on to the *Calibration* phase.
5. *Calibration.* In this phase, the PTx receives information about the PRx, for improving the FOD during the Power Transfer, which is done via the power loss method. The PRx sends information of the typical output power at both light load (high equivalent resistance load) and connected load (low equivalent resistance load), such that, in any condition, the reference power can be interpolated between these two values. In case this packet is received correctly by the PTx, the *Power Transfer* phase is started. If there is no response from the PTx, the process goes back to the *Selection* phase.

6. *Power Transfer*. In this phase, the actual WPT is happening between the PTx and the PRx. During this phase, the PTx can receive several packets from the PRx, of which the most important ones are: the Control Error Packet, such that input power can be adjusted to the right value based on the measured output power, the Received Power packet for FOD, Charge Status packet, End Power Transfer packet and Renegotiate packet.
7. *Renegotiation*. This phase can be started at any moment of the *Power Transfer*, and it is similar to the Negotiation phase.

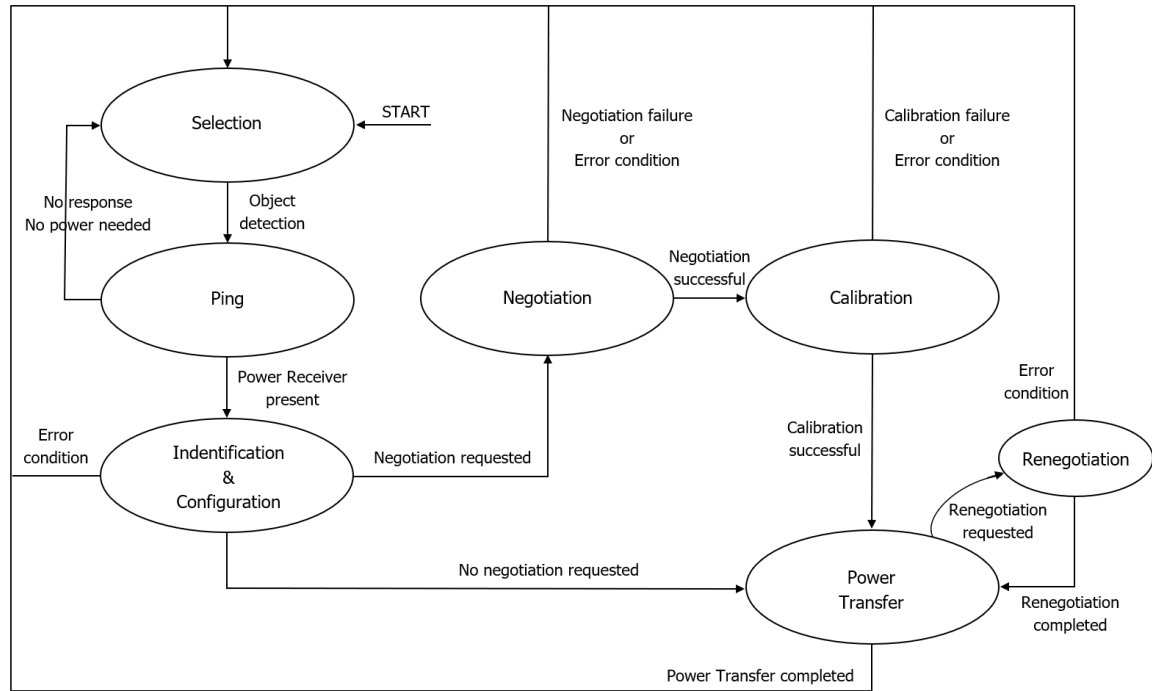


Figure 7.2: Operation sequence of the communication between the PTx and RTx, according to the Qi specification.

### 7.2.2. Amplitude Shift Keying (ASK) communication

The communication between the PTx and the PRx is realized through backscatter modulation. According to the Qi specification, the communication from the PRx to the PTx is Amplitude Shift Keying (ASK) modulated, and from the PTx to the PRx is Frequency Shift Keying (FSK) modulated because the primary inverter is generally operating at fixed frequency. However, since in the e-bike WPT charging system the primary inverter is chosen to be operating at auto-resonant frequency, the ASK modulation is also implemented in the communication from the PTx to the PRx.

ASK communication consists in modulating the power signal between a fixed low and high value, for reflecting an information from one side to the other. This ASK modulator can be realized placing at the DC side a resistor in series with a switch, that is closing and opening for modulating the power signal. Moreover, a demodulator is also needed in the communication system for encoding the messages received. The PRx structure, including the communication, is shown in Figure 7.3, and similar structure applies to the PTx. Both the communication and power lines are connected to the Communication & Control Unit, which manages the received messages and creates the ones to be sent to the other side. Moreover, voltages and currents are also measured and compared to their reference values.

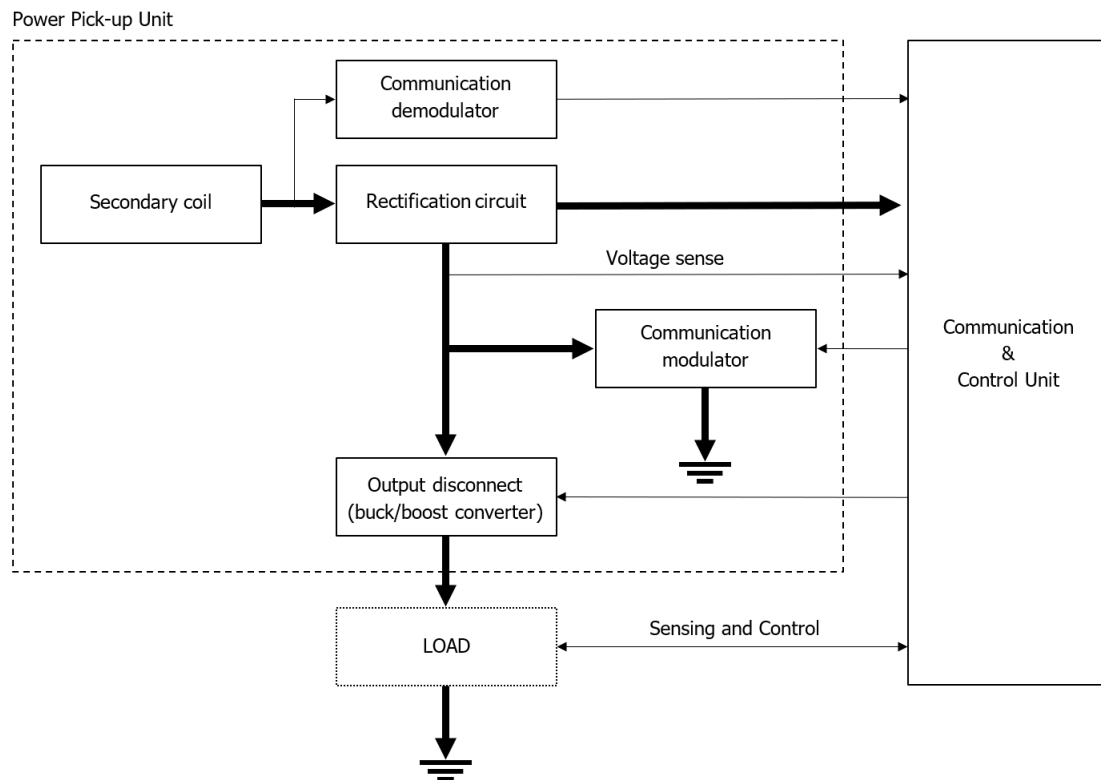


Figure 7.3: PRx structure, including the power and the communication stages. The thick arrows represents power signals and the thin arrows communication signals.

The ASK modulation has a frequency that is several times greater than the resonant frequency  $f_0$ , such that the message can be clearly recognized. Typically, the communication frequency is around 2 kHz. The messages are composed of bits, which can have either a high (=1) or a low (=0) state. The difference between high and low states must be at least 15 mA for currents and 200 mV for voltages. The created data bit must be aligned to an internal clock signal (CLK), such that a bit starts with the rising edge of the CLK. Then, a bit is 1 when at the falling edge of the CLK there is a status change in the communication signal. On the other hand, if at the falling edge of the CLK the communication signal stays constant at the same value, the bit is 0. Moreover, a byte consists of eleven asynchronous serial format bits, such that the Least Significant Bit (LSB) goes first. An example of a byte encoding is shown in Figure 7.4.

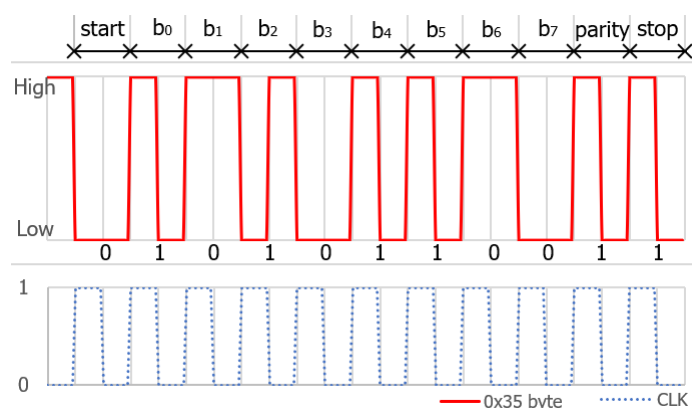


Figure 7.4: Byte encoding in ASK modulation.

The actual useful number of bit are eight, going from  $b_0$  to  $b_7$ . The Start bit is always 0 and the Stop

bit is always 1. The parity bit is 0, if the total number of 1s from  $b_0$  to  $b_7$  is odd, and it is 1 if the total number of 1s is even.

The actual communication between PTx and PRx is realized via data Packets. A Packet is composed of four main parts: a Preamble, Header, Message and Checksum, as shown in Figure 7.5. Each of these parts consists in one or more bytes.

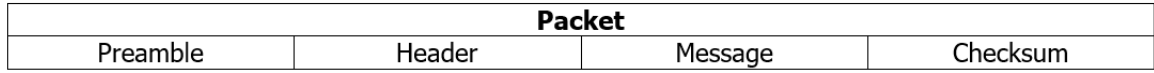


Figure 7.5: Packet structure in the ASK modulation.

The Preamble is a sequence of several 1 bits that allows the PTx to get synchronized before the actual message starts. The Header specifies the packet type. The Message contains the interesting bits, and it must be of the same type of the Header. The Checksum allows checking if any transmission error occurs. All the reference values for encoding the packets are reported in [22].

### 7.2.3. The object detection

The Object Detection (OD) stage happens during the *Selection* phase, when the PTx recognizes that an object is present on its surface. The Qi specification does not give precise instructions for realizing this detection, but it gives two main options.

The first option is called Resonant Shift, and it consists in sending short analog pulses at the resonance frequency of the primary circuit. The pulses are not digital, such that the communication is not involved in this stage. Then, the primary current is measured and, when a variation is detected, an object is present on the PTx surface.

The second option is called Capacitance Change, and it consists in connecting the primary coil to a capacitance sensing unit, disconnecting it from the driving circuit. Once a change in capacitance is sensed, the actual quality factor  $Q_{meas}$  is measured, and the process goes to the digital *Ping* phase. The sensibility of the sensing unit must be at least 100 fF. The energy consumption of this option is overall less than in the first one.

### 7.2.4. The FOD

The FOD consists in checking whether a foreign object is present on the PTx surface and making sure that it is not heated up by the magnetic field of the WPT. The FOD can be done in two different methods, either checking the quality factor before the start of the power transfer or through the power loss method during the power transfer.

The quality factor checking is used to recognize if a foreign object is placed on the PTx interface at the same time as the PRx. As described in Section 7.2.1, before entering the *Ping* phase the actual quality factor  $Q_{meas}$  is measured by sending a small amount of energy such that the receiver is not activated. The measurement circuit of the quality factor is shown in Figure 7.6. Then, in the *Negotiation* phase,  $Q_{ref}$  is compared with  $Q_{meas}$ . In case  $Q_{ref}$  is smaller than  $Q_{meas}$  over a certain threshold, taking into account the possible inaccuracy, the FO is detected, the PTx communicates it to the PRx, and the process is sent back to the *Selection* phase.

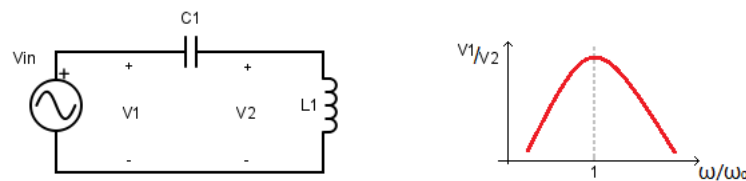


Figure 7.6: Measurement of the quality factor  $Q_{meas}$  for the FOD, before the start of the power transfer.

The power loss method is used for the FOD in case the power transfer is already in progress, such that it is quit in case a foreign object is positioned on the PTx surface. This method consists in measuring the power transmitted  $P_{PT}$  from the PTx, and the power received  $P_{PR}$  at the PRx in the same averaged time interval, such that the power loss  $P_{loss}$  can be computed as

$$P_{loss} = P_{PT} - P_{PR} \quad (7.1)$$

The calculated  $P_{loss}$  is compared to a threshold value  $P_{th}$  and, in case  $P_{loss}$  is greater than  $P_{th}$ , the power transfer is stopped and the operation is sent back to the *Selection* phase. The threshold  $P_{th}$  is calculated taking into account measurement errors.

Moreover, for improving the power loss method, the reference values of  $P_{PT}$  and  $P_{PR}$  at light load ( $P = 10\% \cdot P_{max}$ ) and connected load ( $P = P_{max}$ ) are communicated from the PRx to the PTx in the *Calibration* phase, such that bias errors in the measurements can be removed. In [22], it is explained how the  $P_{PT}$  and  $P_{PR}$  can be calibrated using the reference values at both a light and connected load.

### 7.2.5. Outer control loop

In Figure 7.7, the communication between the PTx and PRx is shown schematically, according to the Qi specification. The power is transferred from the PTx to the PRx, and the PRx determines the actual control point that is compared to the desired control point. From the difference between the two values, the control error value is computed, such that the necessary correction is sent to the PTx via a Control Error Packet. When the PTx receives the error packet, the new input voltage is calculated, and it is set starting from its present value. The new operating point is set, and the PTx will keep it until it receives a new Control error Packet from the PRx.

In e-bike WPT charging system, this communication between the PTx and PRx can be implemented through the outer control loop, using the ASK modulation.

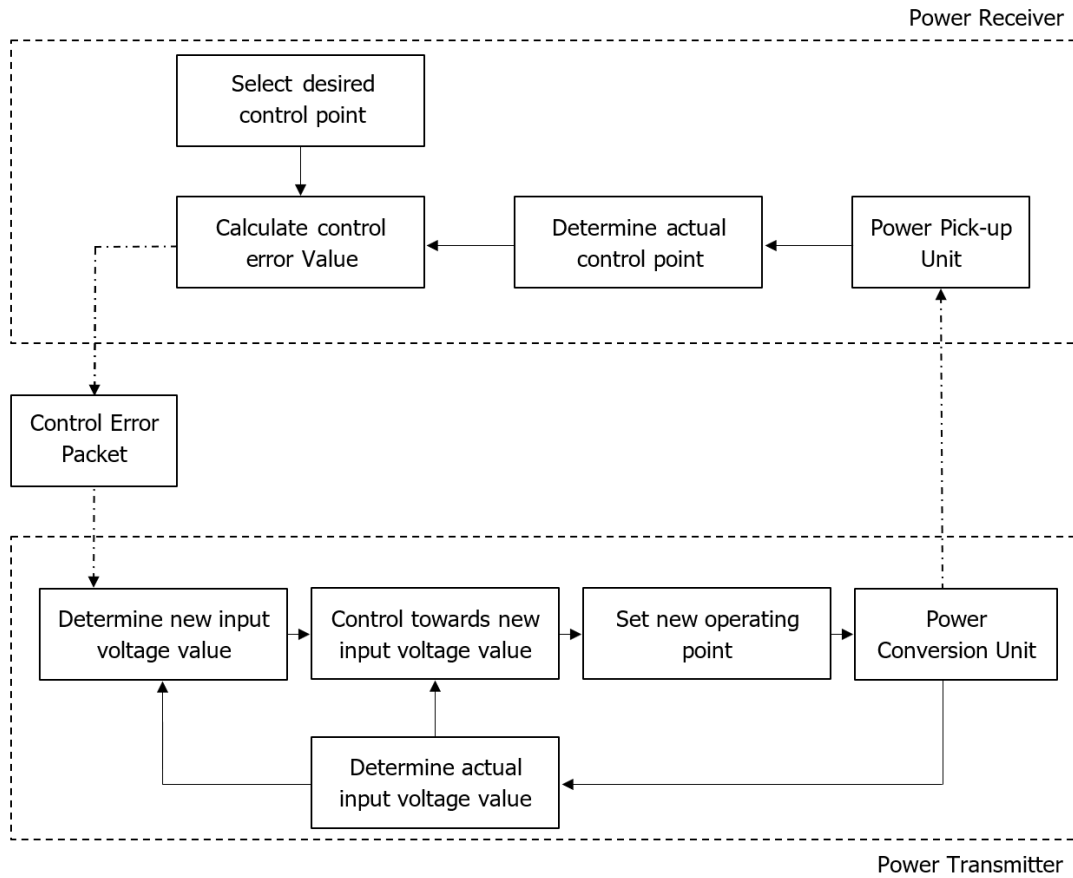


Figure 7.7: Power Transfer outer control loop between the PTx and the PRx.

### 7.2.6. Electromagnetic Compatibility (EMC)

In Annex A of [22], the EMC regulations are mentioned referring to existing standards, depending on the country in which the device is used. It is important that both the PTx and the PRx are compliant to the regulations, such that they are not interfering with other devices in the neighborhood, and they do not cause dangerous electric or magnetic fields to humans or animals.

For what concerns "Requirements for household appliances, electric tools, and similar apparatus", the European directives refer to EN 55014-1 and EN 55014-2.

On the other hand, for what concerns the user Exposure to Magnetic Fields (EMF), there are two independent organizations that provide limits based on scientific works, which are the International Commission on Non-Ionizing Radiation Protection (ICNIRP) and the IEEE. As basic restrictions for the general public, either IEEE C95.1 2005 or ICNIRP 1998 can be taken as references.

Two examples of applicable standards are IEC62311 "Assessment of electronic and electrical equipment related to human exposure restrictions for electromagnetic fields (0Hz -300GHz)", and IEC62233 "Measurement methods for electromagnetic fields of household appliances and similar apparatus with regards to human exposure".

## 7.3. Communication in the e-bike WPT charging system

The Qi specification is the most used for wireless charging portable devices, with a power rating up to 15 W. This specification also suits the e-bike WPT charging system for most characteristics, such as operating frequency range, compensation network, ASK modulation through the power line. However, since the e-bicycle charging system has a rated power of 200 W, the specification must be adapted to this power level.

### 7.3.1. Communication stage at the PRx circuit

A part of the PRx circuit, including its communication stage, is shown in Figure 7.8. In particular, the ASK modulator is realized at the DC side, and it consists of the resistor  $R_{CM}$  in series with the switch SW. Controlling the switch, it is possible to send message packets to the PTx.

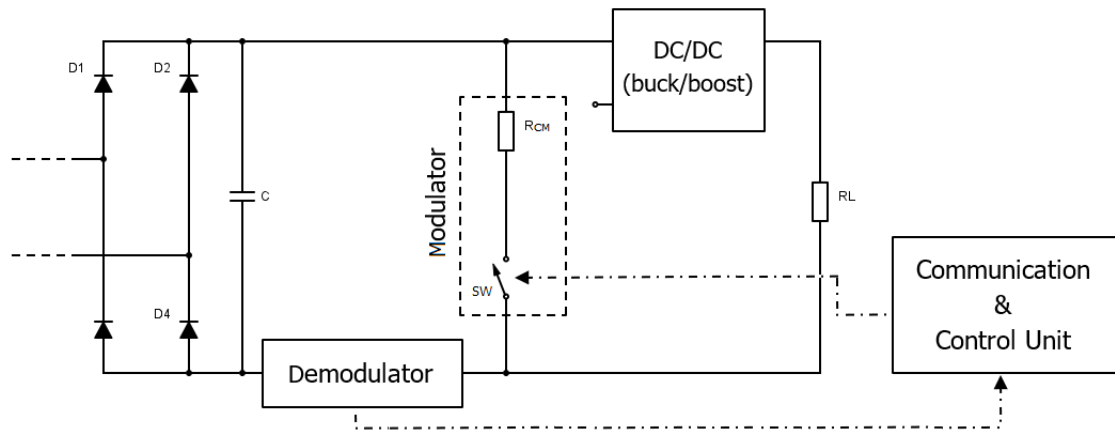


Figure 7.8: Communication stage at the DC side of the PRx, for ASK communication.

An example of simulated waveforms obtained through the ASK modulation is shown in Figure 7.9, taking as reference the PRx circuit in Figure 7.8. The top waveform is the voltage across a shunt resistor  $V_{shunt}$  in series with the primary coil, used to sense the voltage modulation at the PTx, and the bottom waveform is the gate-source voltage  $V_{gs}$  applied to the switch SW, supposing that the SW is a MOSFET. Therefore, the demodulator at the PTx can decrypt the message sent from the PRx, measuring the voltage difference  $\Delta V$  in the amplitude of  $V_{shunt}$ .



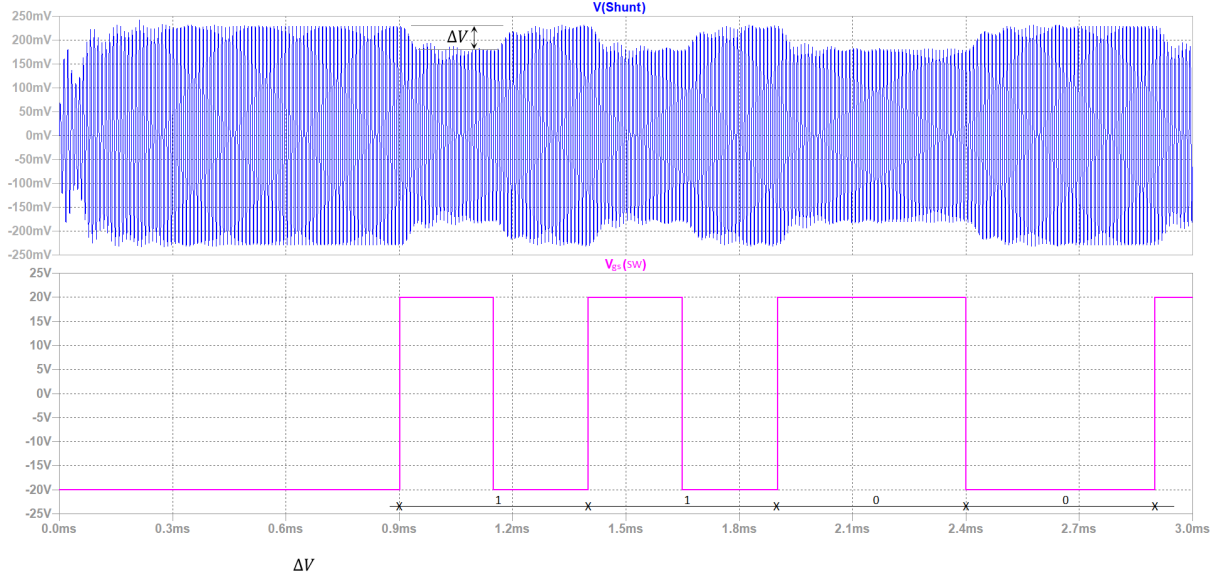


Figure 7.9: Example of modulated voltage for ASK communication, from the PRx to the PTx. In the simulation, the output capacitor  $C = 3 \mu\text{F}$ , the communication resistance  $R_{CM} = 40 \Omega$ , the coupling factor  $k = 0.25$  and the load resistance  $R_L = 12 \Omega$ . The top waveform is the voltage across a shunt resistor  $V_{shunt}$  in series with the primary coil, and the bottom waveform is the gate-source voltage  $V_{gs}$  applied to the switch SW.

### 7.3.2. FOD for measuring $k$

According to Section 7.2.4, before the start of the power transfer, the FOD is executed measuring the quality factor  $Q_{meas}$  of the primary coil. However, this method can also be used to measure the coupling factor  $k$  between the two coils and, in case that is smaller than the minimum allowed value ( $k = 0.1$ ), the power transfer is not started and a warning is sent to the user. Moreover, according to (6.2) and (6.1), the lower is  $k$  the higher would be both the primary and secondary currents, once the power transfer is started. So, at low values of  $k$ , the power transfer can be started at lower  $V_{in}$  rather than at its maximum rated value. In fact, if the system is started at the maximum  $V_{in}$  when the coupling factor is low, the output power would be higher than the rated one, and  $V_{in}$  needs to be decreased afterwards. So, it is reasonable to start the power transfer directly at a proper value of  $V_{in}$ , depending on the measured  $k$ .

As an example, referring to the PTx circuit in Figure 7.6, simulations are executed by imposing as  $V_{in}$  a 5 V square wave, with the fixed frequency of  $f = 100 \text{ kHz}$  for 20 cycles. Depending on different  $R_L$  and  $k$  values, the results are plotted in Figure 7.10 and in Figure 7.11.

Figure 7.10 shows the simulated points of  $V1/V2$  at  $k = 0.1, 0.17, 0.25$ , and for  $R_L = 1, 4, 8, 12, 20, 30, 60, 100 \Omega$ , to have a wide picture of the possibilities. In case the measured value of  $V1/V2$  exceeds the outer red-dashed rectangle, the  $k$  is lower than the minimum allowed value and the power transfer is not started.

On the other hand, Figure 7.11 shows the simulated points of  $V1/V2$  at  $k = 0.1, 0.17, 0.25$ , and only for  $R_L = 60, 100 \Omega$ , because before starting the power transfer the secondary circuit is not activated, and it is equivalent of having a  $R_L \rightarrow \infty$ . Therefore, only the points with the two higher  $R_L$  are actually considered, including their trend lines. Also in this case, if the measured value of  $V1/V2$  exceeds the outer red-dashed rectangle, the  $k$  is lower than the minimum allowed value and the power transfer is not started.

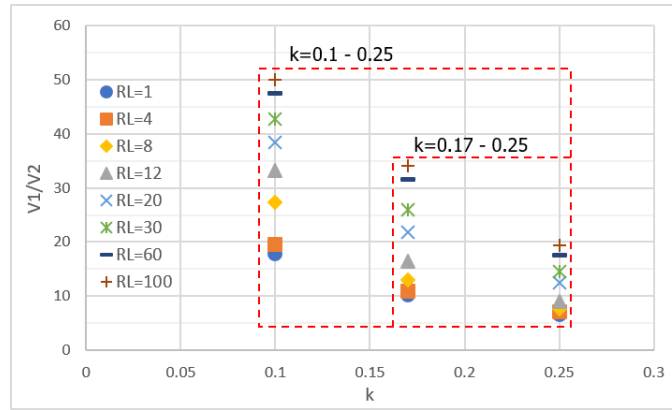


Figure 7.10: Plot of the simulated quality factors  $V1/V2$  depending on the coupling factor  $k$  and for different values of  $R_L$ , before the start of the power transfer.

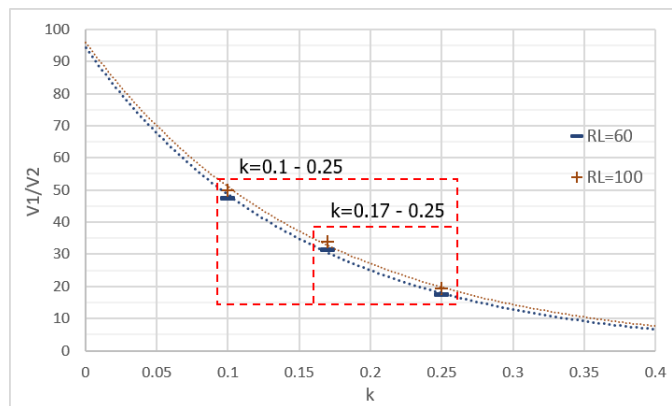
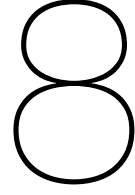


Figure 7.11: Plot of the simulated quality factors  $V1/V2$  depending on the coupling factor  $k$  and for different values of  $R_L = 60$  and  $100 \Omega$ , before the start of the power transfer. Trend lines between the points are also included.

Depending on the minimum chosen coupling factor  $k$ , the allowed range of  $V1/V2$  can be defined as shown in Figure 7.10 and 7.11 with the red dashed rectangles. The minimum allowed value of  $k$  is chosen to be 0.1, but, supposing that it is changed to 0.17, the outer red-dashed rectangle would be shrank to the inner one.

In case the measured  $V1/V2$  value is not within the defined range, it could be that either no PRx is present on the PTx surface, or only a foreign object is present, or a PRx and a foreign object are present at the same time or the  $k$  is too low, under the chosen limit.

On the other hand, in case the measured  $V1/V2$  value is within the allowed range, the operation moves to the digital *Ping* phase. If a PRx is actually present, the communication would begin correctly, and the *Power Transfer* phase can be started at the proper input voltage  $V_{in}$ , depending on the measured  $V1/V2$ .



## Design of the inner control loop

The laboratory setup of the e-bike WPT charging system is a simplified version of the complete system in Figure 2.2, that is used as a proof of concept for verifying the theoretical models and its functioning. The schematic of this setup is shown in Figure 8.1 a). The transmitter is composed of a DC power supply, a full-bridge inverter, the primary compensation network, and the primary coil. The receiver is composed of the secondary coil, the secondary compensation network, the diode-bridge rectifier, and the resistive load  $R_L$ . The setup is shown in 8.1 a) and it has been developed in previous works on this topic. During this project, two main contributions are given to the already existing setup, which are highlighted by the double-line parts in Figure 8.1 b). Firstly, the primary compensation capacitor has been implemented, such that it can stand the high resonant voltage, and that the proper capacitance is chosen according to Table 3.1. This first contribution is discussed in Section 9.1. Secondly, the main part of the design has been dedicated to the inner control loop circuit for the primary inverter.

This Chapter explains the explains in detail the second contribution, i.e., the design of the inner control loop circuit. The design process of the first breadboard prototype is explained in Section 8.1. The designed of the PCB is mentioned in Section 8.2. Finally, some important properties of the designed inner control loop are pointed out in Section 8.3.

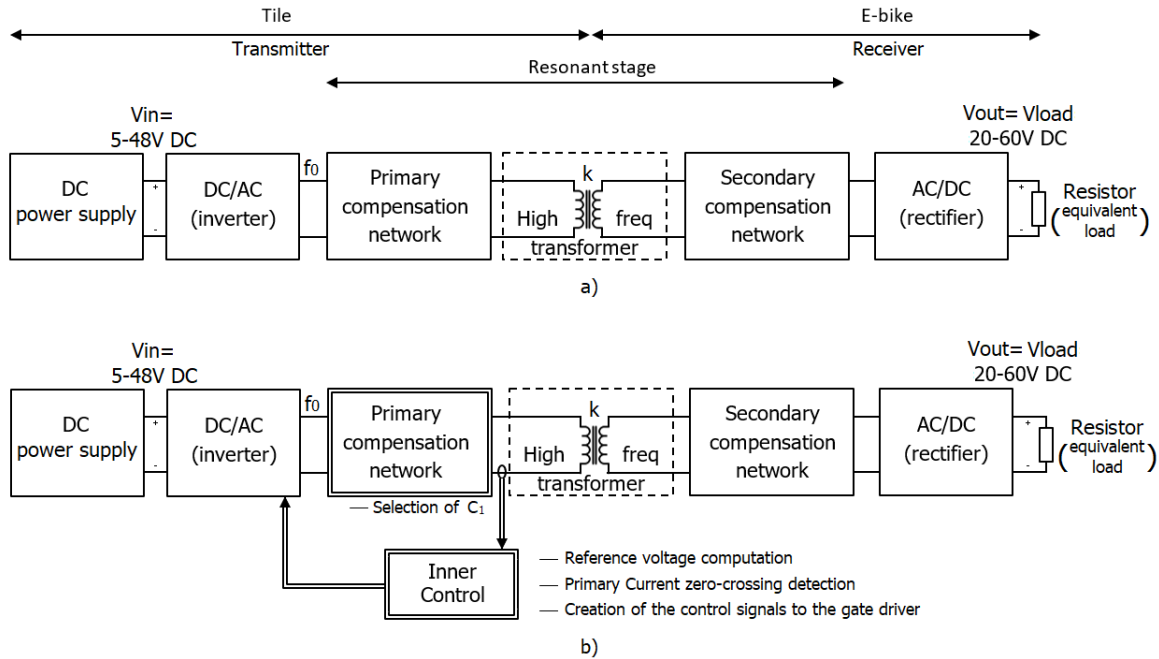


Figure 8.1: Laboratory setup of the e-bike WPT charging system: a) already-existing version, used as a start point; b) addition of the two main contributions of this project, that are the ones highlighted by the double-line.

## 8.1. Design process

The inner control loop takes as input the primary resonant current  $i_1$  and gives as output the control signal to the inverter's gate driver, such that ZCS operation can be achieved. It follows the resonance of the primary circuit, such that it adapts instantaneously to the new resonant frequencies. The control circuit is realized soldering the components on a breadboard with islands, making the connections as shown in the schematic in Figure 8.2. The designed control circuit is purely analog because it does not involve any digital signals.

The control board has three inputs: 5V DC voltage supply, the ground connection in common with the inverter board, and the primary resonant current  $i_1$ . The output signals are two:  $Q$  that controls the switches Q1, Q4 and  $\bar{Q}$  that controls the switches Q2, Q3, referring to the full-bridge inverter in Figure 4.12.

From the 5V DC voltage input, the -5V DC supply voltage is obtained through the DC voltage pump TC7662, as shown in the top left corner of Figure 8.2. Both the 5V and -5V are used for powering the opamps, comparators and the ICs in the board. However, the -5V DC is not purely a voltage source and therefore, if overloaded it could drop significantly. So, for keeping the +5/-5V as constant as possible, several capacitors are inserted between the supply voltages and the ground, in particular, close to their connections.

The primary current  $i_1$  is taken as input through a current transformer, of which primary side is placed in series with the primary coil. The transformer output is then filtered, and the signal is conditioned via the TL071 op-amp, in which the feedback network doubles the signal. The resulting scaling of this first stage is 0.1V/A.

The zero-crossing detection of  $V_{i_{1,A}}$  is executed by the two LM211 comparators. The reference voltage of the comparators is initially tuned manually, such that the ZCS operation is achieved, compensating for all the delays of the control and the gate driver that would make the bridge switch at finite current if the reference value is zero, as explained in Section 6.3.1. One comparator detects the zero-crossing at the positive slope of  $V_{i_1}$  and the other one at its negative slope. It is chosen to treat the two zero-crossings separately because the positive and the negative resonances could be not exactly symmetrical, and the two comparators could need different reference voltages to achieve the ZCS. The two reference voltages  $V_{ref+}$  and  $V_{ref-}$  are provided by the two voltage dividers shown at the bottom of Figure 8.2, which allow varying the voltage output by changing the resistance of a potentiometer manually. In this way, the correct reference value can be tuned. However, it needs to be noticed that, before starting the charging process, the reference values should be set close to 0V ( $\approx \pm 20$  mV) such that the initial transient current is higher than the reference levels and the comparators can start working, making the charging process starts.

The two comparators give square wave outputs that are independent to each other. The positive output  $V_+$  stays high when  $V_{i_1}$  is greater than  $V_{ref+}$ , the negative output  $V_-$  stays high when  $V_{i_{1,A}}$  is greater than  $V_{ref-}$ , and it is possible that the two waveforms overlap for a certain time. However, these outputs are interesting just in a small part of their entire period:  $V_+$  is detecting the positive slope zero-crossing and  $V_-$  the negative one. Therefore,  $V_+$  and  $V_-$  are shrunk in the following stage, such that only their relevant part is taken into account. Then, the outputs are the short pulses  $p_1$  and  $p_2$ .

Finally, the short pulses  $p_1$  and  $p_2$  need to be correlated to each other, to realize the control signal to be sent to the gate driver of the inverter. The NOR Latch phase extends the duration of each short pulse, keeping them high until the other one becomes high, and vice versa. Moreover, a shoot-through protection is inserted, which avoids short circuits in the same leg of the inverter (either Q1, Q4 or Q2, Q3 are on).

The simulated waveforms of the designed inner control loop are shown in Figure 8.3, in which are plotted all the intermediate outputs starting from  $V_{i_{1,A}}$ , to the final outputs to the gate driver  $Q$  and  $\bar{Q}$ .

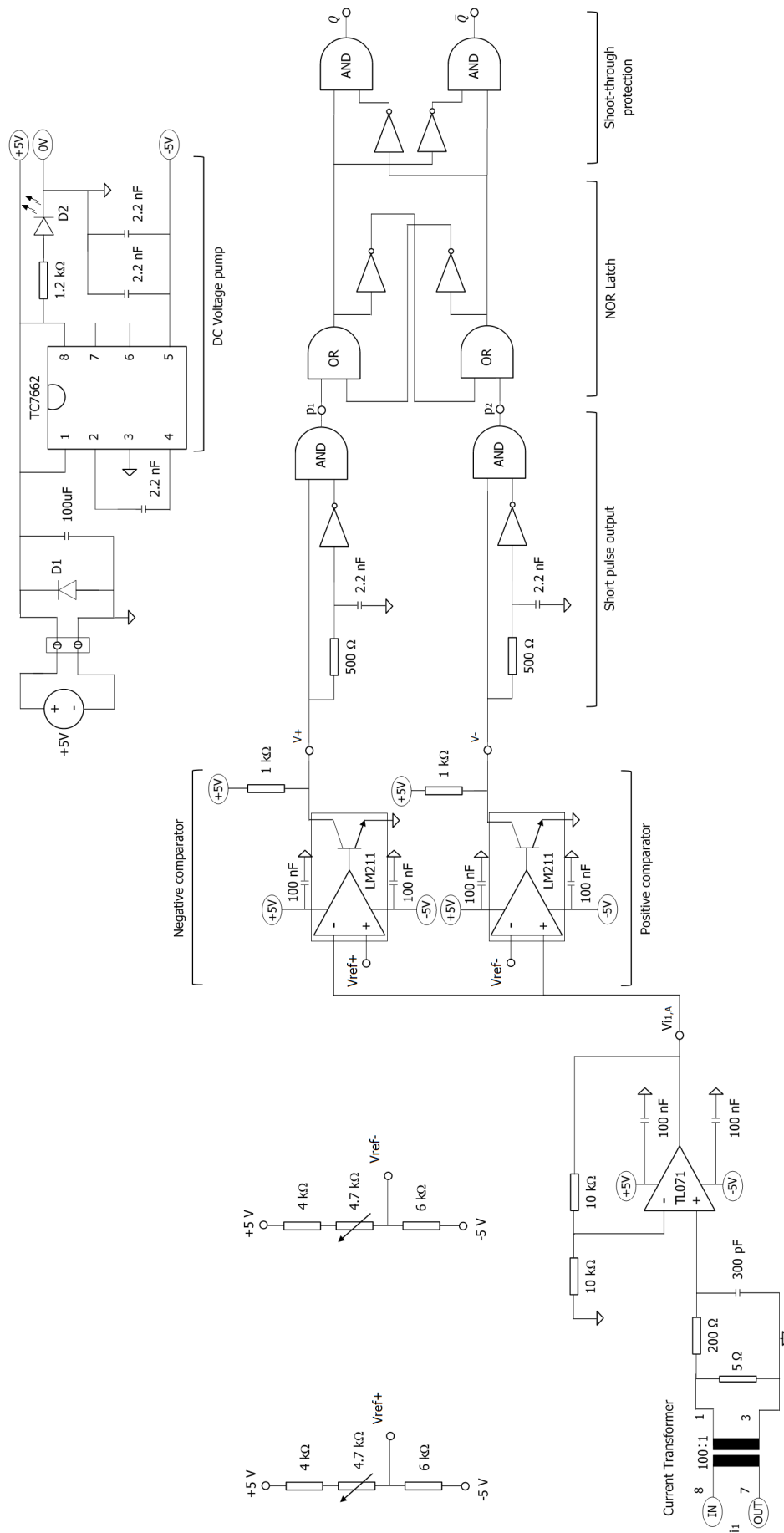


Figure 8.2: Schematic of the designed inner control loop.

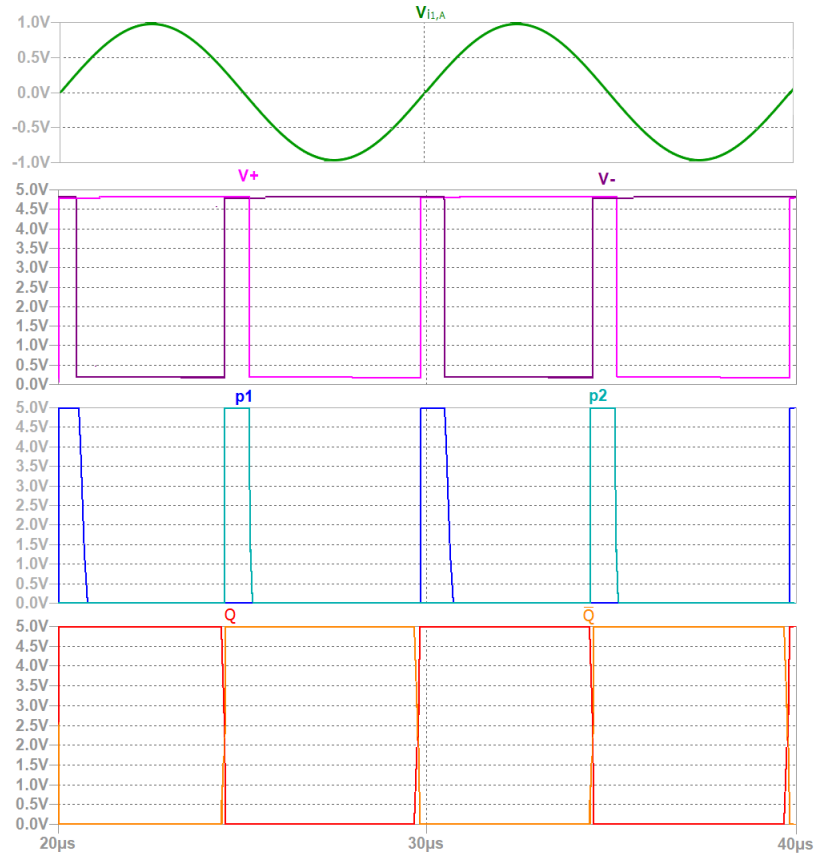


Figure 8.3: Simulated waveforms of the designed inner control loop in Figure 8.2.

For each comparator, the reference voltage  $V_{ref}$  is initially varied manually, changing the resistance value of a potentiometer via its rotating contact. However, the automatic adjustment of the reference level would be a considerable advantage in the control circuit. That could be possible finding the dependence of the reference voltage on another quantity in the power circuit, such that, measuring this quantity, the correct value of the reference voltage can be set automatically.

The dependence of on the derivative of  $V_{i1,B}$  is investigated at the zero-crossing of the current, for both the positive and negative slope. The differentiator circuit in Figure 8.4 is then added to the inner control circuit of Figure 8.2, which takes as input  $i_1$  and gives as output the rectified derivatives at the zero-crossing  $V_{diff+}$  and  $V_{diff-}$ , which are used to adapt  $V_{ref+}$  and  $V_{ref-}$ , respectively.

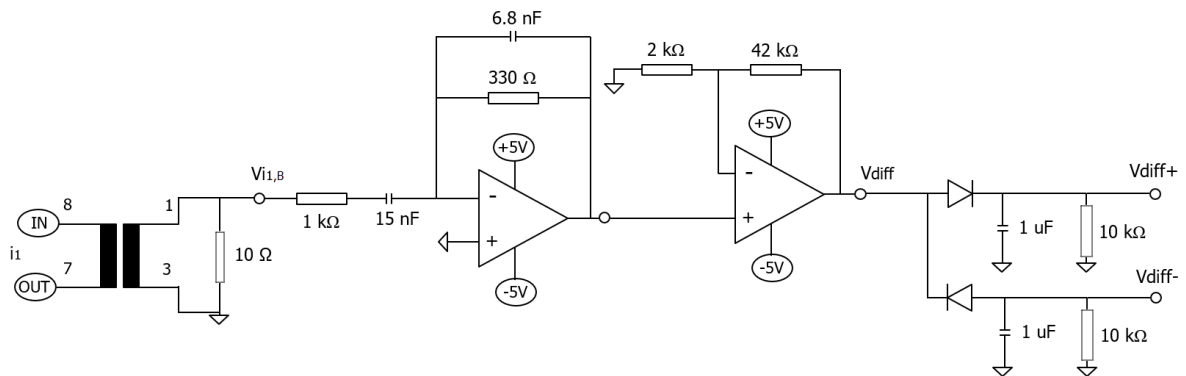


Figure 8.4: Differentiator circuit, which takes as input the primary current  $i_1$  and gives as output both the positive and negative rectified derivatives  $V_{diff+}$  and  $V_{diff-}$ , at the zero-crossing.

For finding the actual dependence of the reference voltage  $V_{ref+(-)}$  on  $V_{diff+(-)}$ , several measurements at different primary current values are executed. For each operating point, the value of  $V_{ref+}$  and  $V_{ref-}$  are tuned and measured, such that ZCS is achieved. Then, the average values of  $V_{diff}$  are measured while either the short pulse  $p_1$  or  $p_2$  is high. An example of measured waveforms is shown in Figure 8.5. It is possible to notice that, as expected, the derivative  $V_{diff}$  is leading the original signal  $V_{diff}$  of  $\pi/2$ . Moreover,  $V_{diff}$  is positive when  $V_{i_1}$  has a positive slope and it is negative when  $V_{i_1}$  has a negative slope. Zoomed overviews on these waveforms are shown in correspondence of the short pulses  $p_1$  and  $p_2$ , respectively, in Figure 8.6 a) and b). All the waveforms are plotted with a bandwidth of 10 MHz, because at full bandwidth the measurement disturbances make the waveforms not clear.

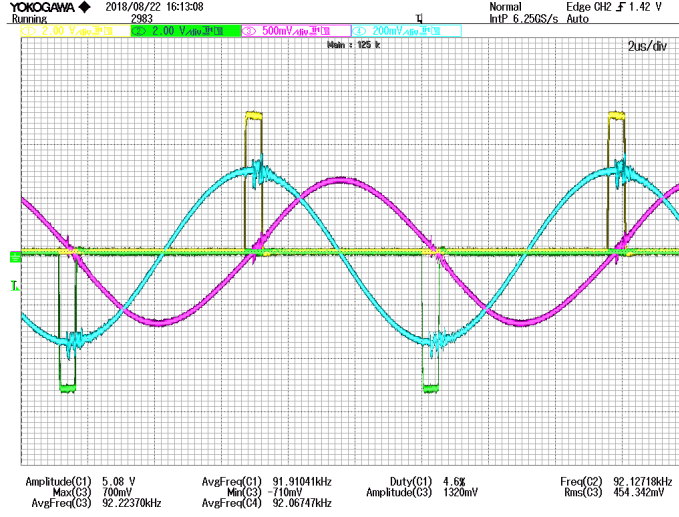


Figure 8.5: Example of measured  $v_{i_1}$  and  $v_{diff}$  for  $I_{1,RMS} = 4.5$  A. Channel 1 (yellow waveform) is the short pulse  $p_1$ . Channel 2 (green waveform) is the short pulse  $p_2$ , inverted. Channel 3 (pink waveform) is  $v_{i_1}$ . Channel 4 (blue waveform) is  $v_{diff}$ . All the waveforms are shown with a bandwidth of 10 MHz.

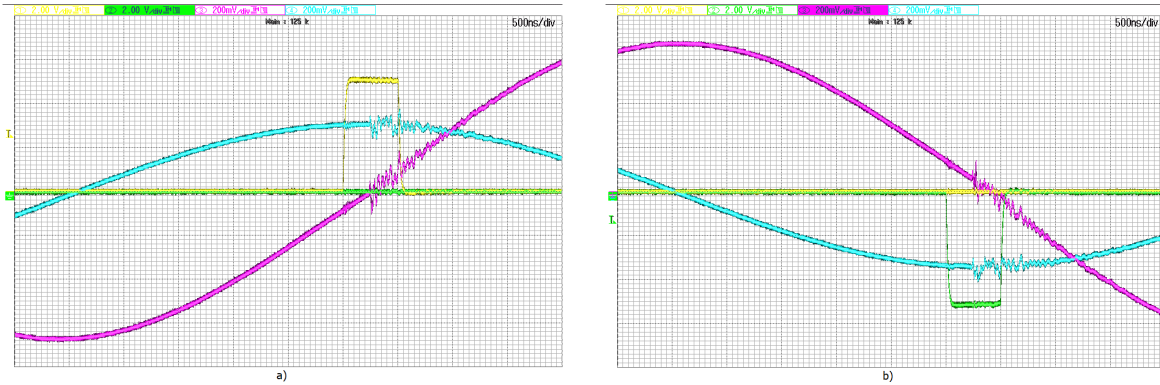


Figure 8.6: Channel 1 (yellow waveform) is the short pulse  $p_1$ . Channel 2 (green waveform) is the short pulse  $p_2$ , inverted. Channel 3 (pink waveform) is  $v_{i_1}$ . Channel 4 (blue waveform) is  $v_{diff}$ .  
a) Derivative centered at  $p_1$ , at the positive slope of  $v_{i_{1,B}}$ . b) Derivative centered at  $p_2$ , at the positive slope of  $v_{i_{1,B}}$ .

The dependence of  $V_{ref}$  on  $V_{diff}$  has to be found at different primary current values  $i_1$ . It could be done either varying the the input voltage  $V_{in}$  or the resistive load  $R_L$  or the coupling factor  $k$  or combining these variables. In case  $R_L$  or  $k$  are varied, the frequency will also vary as consequence of bifurcation. So, for the same value of primary current, the derivative could be very different. This factor needs to be taken into account since our system is supposed to be working at auto-resonant frequency.

The relation between  $V_{ref}$  and  $V_{diff}$  is found measuring their values at the maximum coupling condition and at fixed  $R_L$ , at different values of  $i_1$ . In fact,  $i_1$  is varied from about 1 A to 6 A changing the input voltage. In this way, also the current derivative of the negative and positive slope is changed.

Figure 8.7 shows the the measured points of  $V_{ref}$  and  $V_{diff}$  for each comparators, including trend lines that approximate linearly this dependence. Next to each line it is also reported its equation and its coefficient of determination  $R^2$ , which indicates how good the linear approximation is.

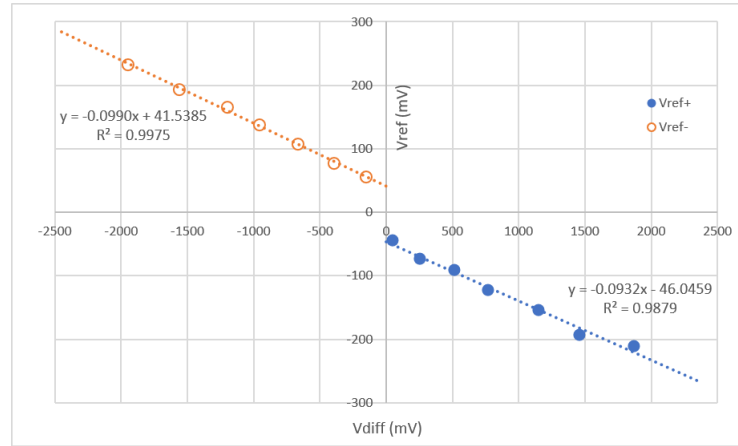


Figure 8.7: Dependence of the reference  $V_{ref}$  voltage on the derivative  $V_{diff}$  at the current at the zero-crossing, for both comparators. The measured points are plotted with their linear trend lines, equations and their coefficient of determination  $R^2$ .

Since  $R^2$  is close enough to 1, it is clear that for both the positive and negative slope of the current at the zero crossing  $V_{ref}$  is linearly dependent on  $V_{diff}$ . Therefore, the following step consists in implementing the found equation such that the reference voltage can be set automatically and the operation is always ZCS. However, that equations describe effectively the case of maximum coupling and medium-high current range. Both the equations have an off-set value of  $V_{ref}$  which would make the power transfer stops when the current drops under 0.5 A, because  $V_{ref}$  would be higher than the actual value of  $V_{l1}$  and the comparators would stop working. For this reason, starting from the equations in Figure 8.7, the off-sets are lowered of about 30%, and the gain increased proportionally, such that the system would also work for lower currents without stopping. The drawback of this adjustment is that the ZCS is not optimized any for the low and mid-range current values, but it is for higher current in which the ZCS is more important and critical. The linear relation between  $V_{diff}$  and  $V_{ref}$  is implemented for both the positive and negative comparators with the circuits in Figure 8.8 a) and b), respectively.

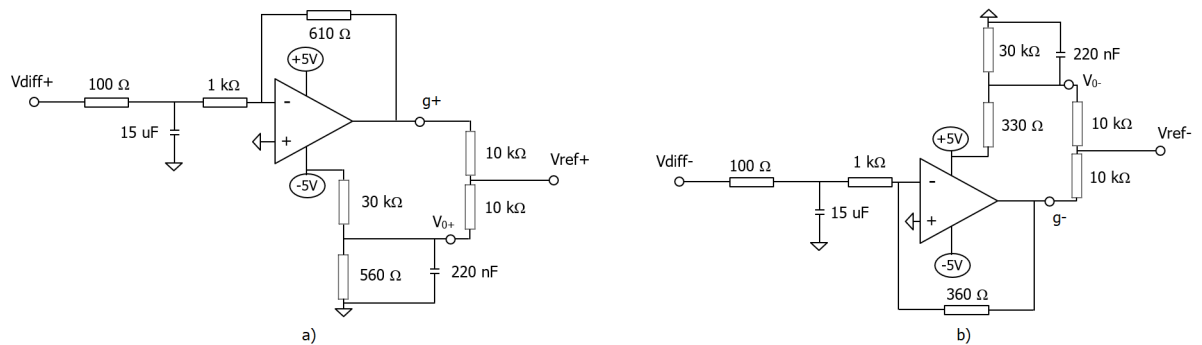


Figure 8.8: Circuits that automatically set the reference voltage  $V_{ref}$  depending on the derivative of the primary current  $V_{diff}$ . a)  $V_{ref+}$  for the positive comparator from  $V_{diff+}$ . b)  $V_{ref-}$  for the negative comparator from  $V_{diff-}$ .

Both the circuits in Figure 8.8 takes as input the rectified derivative  $V_{diff}$  at the zero-crossing of the current from the differentiator circuit in Figure 8.4. Then,  $V_{diff}$  passes through a low-pass filter with a cut-off frequency of 100 kHz, for eliminating the high-frequency harmonics since it is supposed to be a DC voltage. Then, the desired gain  $g$  is set via an opamp and resistors that act as a voltage divider. On the other hand, the off-set value  $V_0$  is created by a voltage divider connected to the supply voltage. Finally, the gain  $g$  and the off-set value  $V_0$  are summed via the output voltage divider, that gives  $V_{ref}$ . It must be taken into account, that  $g$  and  $V_0$  are double the desired value, because for summing them



a voltage divider is used that halves their value, giving the correct output  $V_{ref}$ . However, both the circuits are the results of trade-off that can be customized changing the resistors' value for having a different value of either the gain  $g+$ ,  $g-$  or the off-set  $V_{0+}$ ,  $V_{0-}$ .

After building the circuits in Figure 8.8, their outputs are directly connected to the reference voltage inputs of the comparators in Figure 8.2, disconnecting the outputs from the voltage dividers. The ZCS operation is now achieved automatically for different coupling and load conditions. The inner control loop board is shown in Figure 8.9 a), and the entire laboratory setup of the e-bike WPT charging system is shown in Figure 8.9 b).

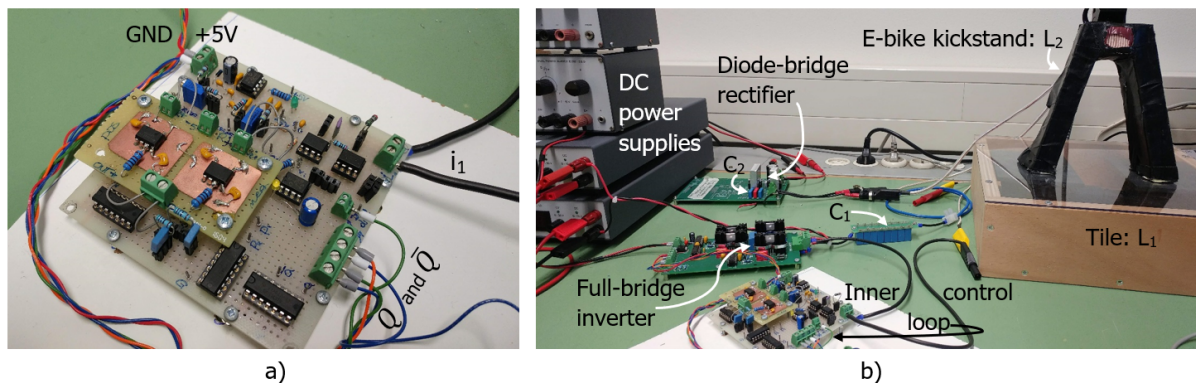


Figure 8.9: a) Inner control loop board. b) Entire laboratory setup of the e-bike WPT charging system.

## 8.2. PCB design

The control circuit described in Section 8.1 has been built step by step on breadboards with islands, soldering the components and realizing the connection between them as shown in Figure 8.2, 8.4 and 8.8. This first circuit has been useful in the developing stage, because it allows realizing all the sub-circuits gradually, to test them singularly and to easily make improvements to changes. However, once the final working configuration is achieved, the connections between the breadboards start being critical, making the whole circuit fragmented because each part was not built at the same time. Therefore, it is clear the need of designing a printed circuit board (PCB) for making connections between the components smarter and shorter and for reducing the circuit size. A double-layer PCB is then designed, using the circuit schematics shown in Figure 8.2, 8.4 and 8.8. The only components not included in the schematics are the decoupling capacitors of 100 nF connected close to each IC's voltage supply input (+5V/−5V). In Figure D.1 the designed PCB is schematically shown.

## 8.3. Properties of the primary inner control loop

### 8.3.1. Analog Control Circuit

The controller explained in Chapter 8 is completely analog, fast, robust and compact. It is composed of two current transformers, seven ICs of which five are opamps and two comparators, three DC voltage converter, three logic chips, and passive components. Therefore, there are no digital signals in the circuit since microcontrollers are not used. It has been chosen to have design without micro-controllers for three main reasons.

1. The total e-bike WPT charging system price should be affordable, such that it is a few times lower than the price of the bike itself. Therefore, each subsystem should be optimized not only qualitywise, but it also needs to be cost-effective. For what concerns this thesis, the subsystem to be developed is the control of the primary inverter. So, realizing a control circuit without micro-controller would decrease the costs dramatically.
2. Using just passives and ICs reduces the complexity of the control circuit. The programming is not necessary anymore, and all the faults and issues related to it are also obviously avoided. The control circuit would be simpler and more elegant.

3. The main goal is to have a fast auto-resonating control circuit which follows the resonance of the primary circuit such that ZCS operation is achieved. This operation is intrinsically simple, and adding a microcontroller is not necessary, it would only worsen the delays between the signals.

On the other hand, this simple analog control circuit works perfectly for its self-resonating operation, but in case extra functions should be included a microcontroller could become essential. For example, for implementing the communication between the primary and secondary power circuits, for the starting-up/shutting-down strategies and for realizing advanced safety measurements. However, a specific microcontroller for these extra functions can be used that might be cheaper and smaller than using a micro controller for the whole operation.

### 8.3.2. Low Cost Control Circuit

According to what explained in Section 8.3.1, the control circuit has only analog components. For this reason, the price of the control is also relatively low, and this characteristic is essential for being competitive in the market. All the costs are listed in Table 8.1, referring to the supplier Farnell [23].

Table 8.1: Components' and approximate total cost for the control circuit.

Component	Quantity used	Cost (€)	
		Single Unit	500+ Units
TC7662B Voltage Converter	3	2.04	1.29
TL071 Op-amp	5	0.428	0.222
LM211 Comparator	2	0.374	0.176
SN7404N Inverter	1	0.314	0.131
SN7432N OR Gate	1	0.314	0.131
SN7408N AND Gate	1	0.465	0.241
B82801B Current sensing transformer	2	1.97	1.36
Resistor, Capacitors, Diodes, LED etc	-	≤2	≤1
Connectors, terminals header etc.	-	≤4	≤2
PCB	1	50	3
<b>Total Cost for the Control Circuit</b>		<b>≈ 70€</b>	<b>≈ 21€</b>

The cost of the control circuit is moderate, but it drops exponentially while the number of ordered units increase. Therefore, the price stated in Table 8.1 is just an indication.

## Experimental set-up and results

In both Sections 3.3.2 and 6.2, the AC frequency analysis of both primary and secondary circuits is based on the equivalent circuit equations. Moreover, in Section 5.1, the simulated voltages and currents are plotted depending on the coupling factor  $k$  and load resistance  $R_L$ . These results are useful means to predict the system behavior, before executing the actual testing. However, these theoretical values need to be validated with measurements, such that the model is confirmed to be a good reference. The measurements are also useful means for improving the theoretical model itself, and correcting the possible mistakes.

In this Chapter, the laboratory prototype of the e-bike WPT charging system is tested, and it is divided into two main parts. Firstly, in Section 9.1, the theoretical results based on the equivalent circuit equations are compared to the measurements. In this section, also the coupling factor  $k$  is measured and the correct primary compensation capacitor  $C_1$  is selected. Secondly, in Section 9.2, the results and performance of the implemented inner control loop are evaluated.

### 9.1. Model validation

#### 9.1.1. Measurement of the circuit parameters and $C_1$ selection

Before starting with the actual validation of the theoretical model, the parameters in the circuit must be measured such that the comparison is valid. Therefore, both the primary and secondary coil inductances  $L_1$  and  $L_2$ , and their maximum coupling factor  $k_{max}$  are measured. In fact, in all theoretical analysis their values were supposed to be as the ones in Table 3.2 from [9], the previous work on this topic. However, it is important to verify their actual value in the laboratory prototype. The measured  $L_1$  and  $L_2$  at 100 kHz with an LCR meter are shown in Table 9.1. In particular,  $L_1$  and  $L_2$  are measured in two cases: when the two inductors are not coupled ( $k = 0$ ), and when they are one on the top of each other, such that their axis is completely aligned ( $k = k_{max}$ ). According to Table 9.1,  $L_1$  and  $L_2$  are highly dependent on  $k$  and, consequently, on their relative position.

Table 9.1: Measured primary and secondary resonant inductance values at 100 kHz, for  $k = 0$  a  $k = k_{max}$ .

$k$	$L_1(\mu\text{H})$	$L_2(\mu\text{H})$
0	58.07	40.78
$k_{max}$	70.28	48.87

After measuring  $L_1$  and  $L_2$ , the proper value for the primary compensation capacitor  $C_1$  is computed, such that the primary and secondary S-S compensation networks are tuned on the same resonant frequency. The secondary capacitor  $C_2$  value is already present on the rectifier board, and its capacitance

is  $C_2 = 50$  nF measured at 100 kHz. Therefore, according to Table 3.1 for the S-S compensation, the primary capacitance  $C_1$  has to be

$$C_1 = \frac{L_2 C_2}{L_1} = \frac{48.87 \mu\text{H} 50 \text{ nF}}{70.28 \mu\text{H}} = 34.8 \text{ nF} \quad (9.1)$$

This value of  $C_1$  is computed considering the values of  $L_1$  and  $L_2$  at  $k = k_{max}$ . Since the  $C_1$  has to stand high resonant voltage peaks, it is chosen to combine eight  $4.7$  nF ( $\pm 10\%$ ) capacitors in parallel, with a voltage rating of 2 kV DC/780 V RMS AC, such that a capacitance of 35 nF at 100 kHz is obtained. Paralleling these capacitors makes the total ESR eight times lower, giving less damping in the resonant primary circuit. This properly tuned primary compensation capacitor is then inserted in series with the primary coil, and this is one of the main contributions of this project.

Finally, for being able to verify the model, it is important to quantify the value of the maximum coupling factor  $k_{max}$ . Executing an open-circuit voltage test as shown in Figure 9.1, it is possible to compute the mutual inductance  $M$  as

$$M = \frac{V_{oc}}{j\omega I_1} = \frac{V_{oc}/90^\circ}{j\omega I_1/0^\circ} = \frac{V_{oc}}{\omega I_1} \quad (9.2)$$

Then, knowing the values of  $M$ ,  $L_1$  and  $L_2$ ,  $k$  can be found from (3.1).

$$k = \frac{M}{\sqrt{L_1 L_2}} \quad (9.3)$$

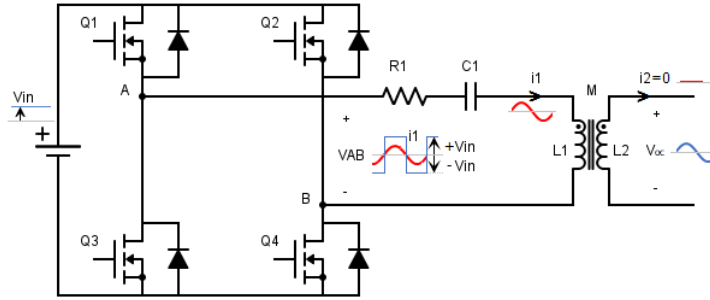


Figure 9.1: Open-circuit voltage test.

The open-circuit voltage test is executed with the two coils completely aligned, and at a relatively low input voltage  $V_{in} (= 7 \text{ V})$ , because  $V_{oc}$  and  $I_1$  become high when the secondary circuit is open. The measured waveforms are plotted in Figure 9.2. The used values of  $L_1$  and  $L_2$  are shown in Table 9.1.

Thus, it is possible to calculate  $k_{max}$  from (9.2) and (9.3):

$$k_{max} = \frac{V_{oc}}{2\pi f I_1 \sqrt{L_1 L_2}} = \frac{97.67 \text{ V}}{2\pi \cdot 101.5 \text{ kHz} \cdot 9.33 \text{ A} \cdot \sqrt{70.28 \mu\text{H} \cdot 48.87 \mu\text{H}}} = 0.28 \quad (9.4)$$

The measured  $k_{max} = 0.28$  is higher than 0.25 found in the former project about this topic. The reason for this difference is that the setup is not completely the same, and  $L_1$  has been replaced.

Moreover, the wire resistances  $R_1$  and  $R_2$  of both the primary and secondary circuit are also measured. The measured values of the circuit parameters are summarized in Table 9.2, and these are used of the further analysis.

Table 9.2: Parameters' value of the set-up, measured at 100 kHz, and  $k = k_{max}$ .

$k$	$L_1 (\mu\text{H})$	$L_2 (\mu\text{H})$	$C_1 (\text{nF})$	$C_2 (\text{nF})$	$R_1 (\Omega)$	$R_2 (\Omega)$
0.28	70.28	48.87	35	50	0.5	0.3

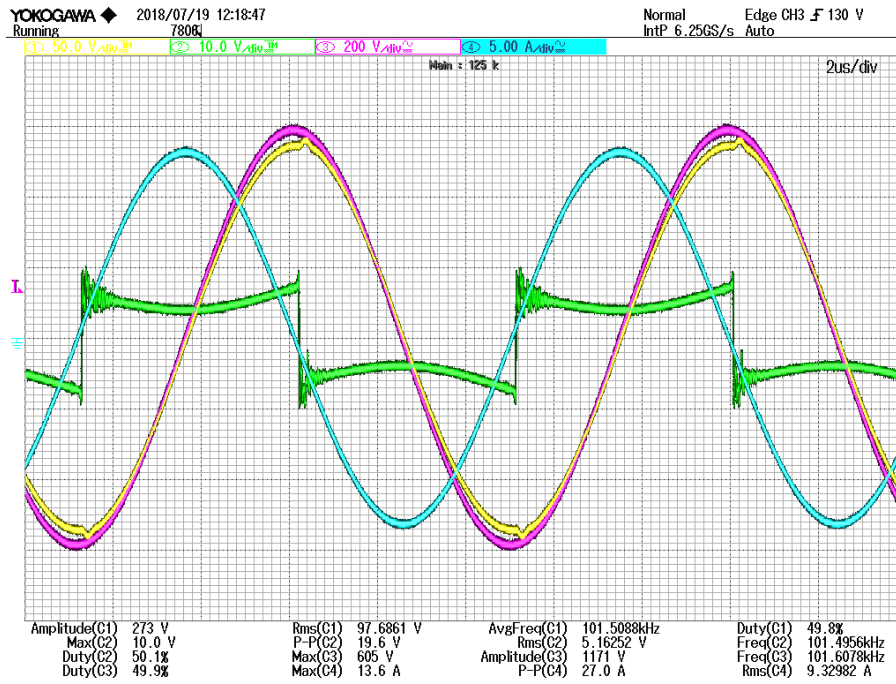


Figure 9.2: Open-circuit voltage test waveforms. The yellow waveform (channel 1) is open-circuit voltage  $v_{oc}$ , the green waveform (channel 2) is inverted voltage at the full-bridge output  $v_{AB}$ , pink waveform (channel 3) is the voltage across the primary capacitor  $C_1$  and the blue waveform (channel 4) is the primary current  $i_1$ .

### 9.1.2. Comparison between theoretical results and measurements

After measuring all the circuit parameters, measurements on the set-up shown in Figure 8.1 working at ZCS, at  $V_{in} = 48$  V and  $k = 0.28$  are executed. These measurements are compared with the theoretical results from the equivalent circuit equations of Section 3.3.1, for verifying the validity of the theoretical model. The comparison of  $i_1$  and  $i_2$  peak values depending on the operating frequency  $f_0$  is shown in Figure 9.3, for different value of  $R_L$ . Moreover, the absolute percentage errors of the equivalent model results respect to the measurements are shown in Figure 9.4.

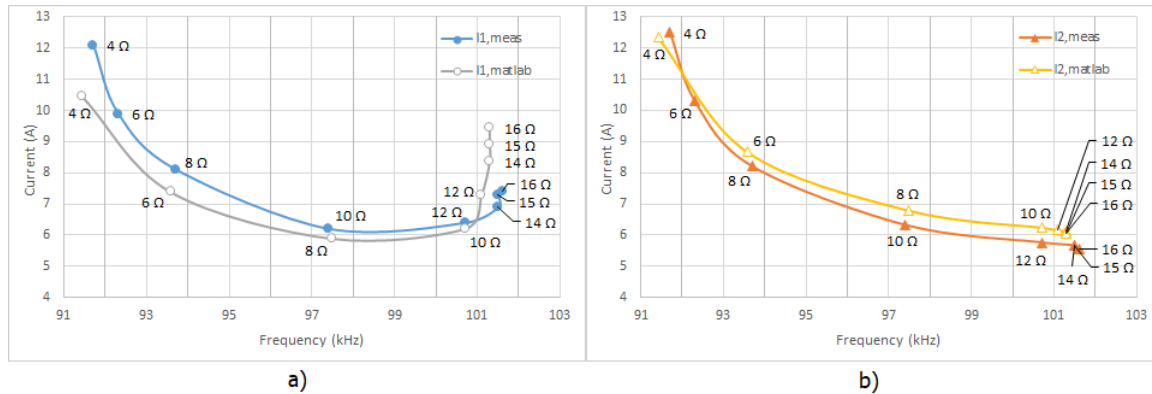


Figure 9.3: Comparison between the measured and theoretical peak values of: a)  $i_1$ , and b)  $i_2$ , depending on the operating frequency, at  $V_{in} = 48$  V,  $k = 0.28$  and different values of  $R_L$ .

The absolute percentage error is up to 27%. Therefore, there is still room for improving this comparison, and the reason of this relatively high error is investigated.

A possible cause of this mismatching, could be that in the equivalent circuit of the theoretical model,  $R_L$  is directly connected to the secondary compensation network, as shown in Figure 3.4. On the other hand, in the set-up shown in Figure 8.1 there is a diode-bridge rectifier between the secondary compensation network and  $R_L$ .

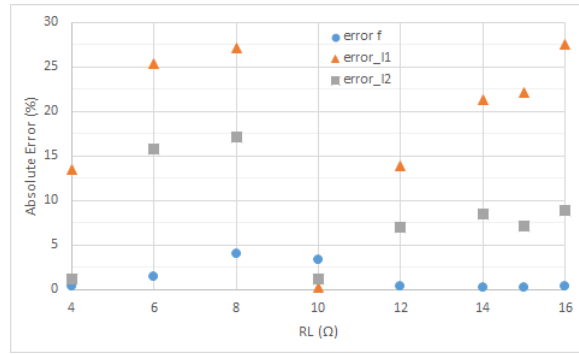


Figure 9.4: Absolute percentage errors of  $f$ ,  $i_1$  and  $i_2$  of Figure 9.3.

For having a secondary circuit more similar to the one in the equivalent circuit model of Figure 3.4, the diode-bridge rectifier is removed from the set-up, and  $R_L$  is directly connected to the secondary compensation network. The aim is to verify if the theoretical and the experimental results would be more similar in this case. In this configuration, measurements of the input impedance  $Z_{in}$ , and the peak values of  $i_1$  and  $i_2$  are executed at  $V_{in} = 20\text{ V}$  and  $k = 0.28$ . The comparison between the theoretical results and measurements is shown in Figure 9.5, depending on the operating frequency  $f_0$  and at different  $R_L$ . Moreover, the absolute percentage errors of the equivalent model results respect to the measurements are shown in Figure 9.6.

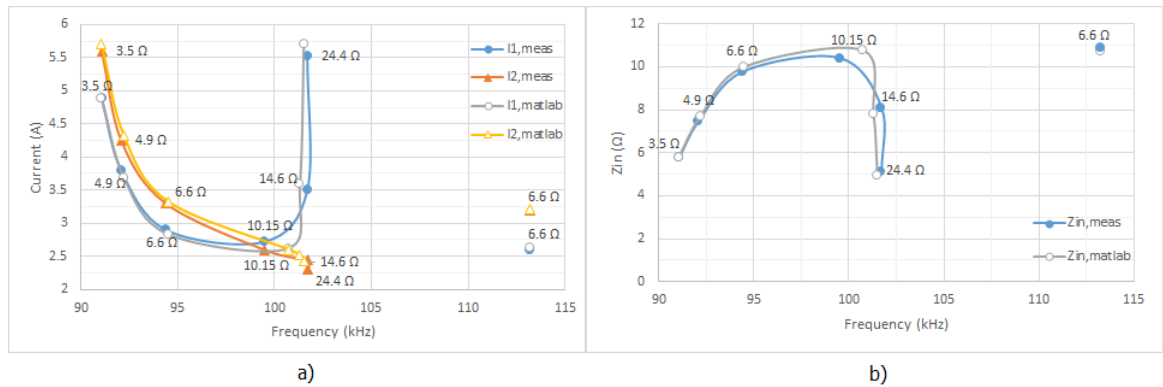


Figure 9.5: Comparison between the measured and the theoretical peak values of: a)  $i_1$ ,  $i_2$ , and b)  $Z_{in}$ , depending on the resonant working frequency. Moreover,  $V_{in} = 20\text{ V}$  and the rectifier is not included in the set-up.

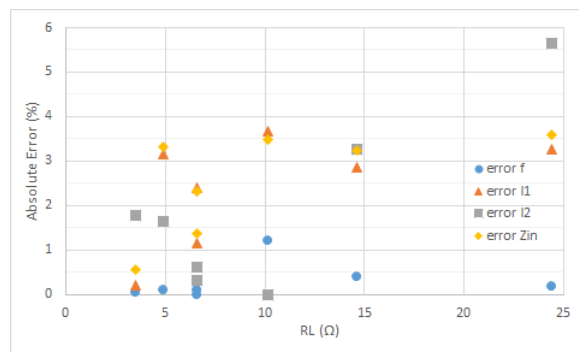


Figure 9.6: Absolute percentage errors of  $f$ ,  $I_1$ ,  $I_2$  and  $Z_{in}$  of Figure 9.5.

The percentage errors between the measured and theoretical values of  $I_1$ ,  $I_2$  and  $Z_{in}$  are mostly under 5%, and this error is due to measurement errors (see Notation) and to the variable value of each component. This means that the equivalent model is describing well the behavior of the real circuit. Figure 9.7, 9.8, 9.9, 9.10 and 9.11 show how the theoretical values of  $f_0$ ,  $I_1$ ,  $I_2$  and  $Z_{in}$  are found.

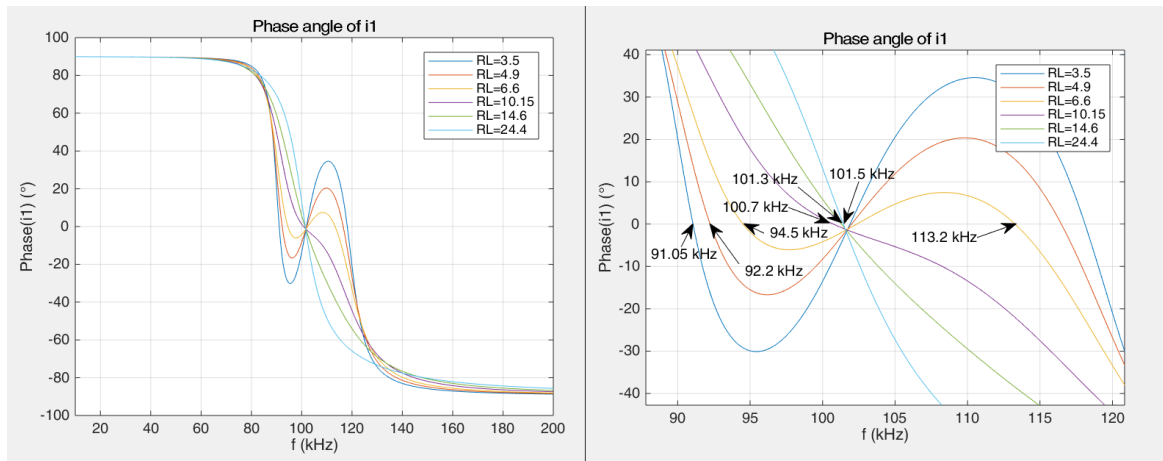


Figure 9.7: Plot of  $i_1$  phase angle depending on the operating frequency and at different  $R_L$  values. In the right pictures, the frequencies at which the phase angle is zero are pointed out.

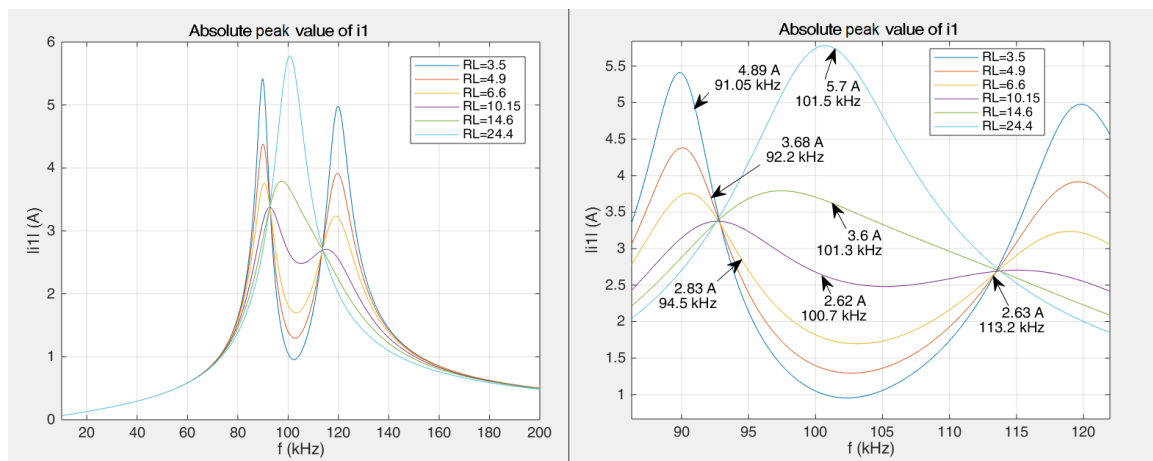


Figure 9.8: Plot of  $i_1$  absolute peak value depending on the operating frequency and at different  $R_L$  values. In the right pictures, the points at which the  $i_1$  phase angle is zero are pointed out.

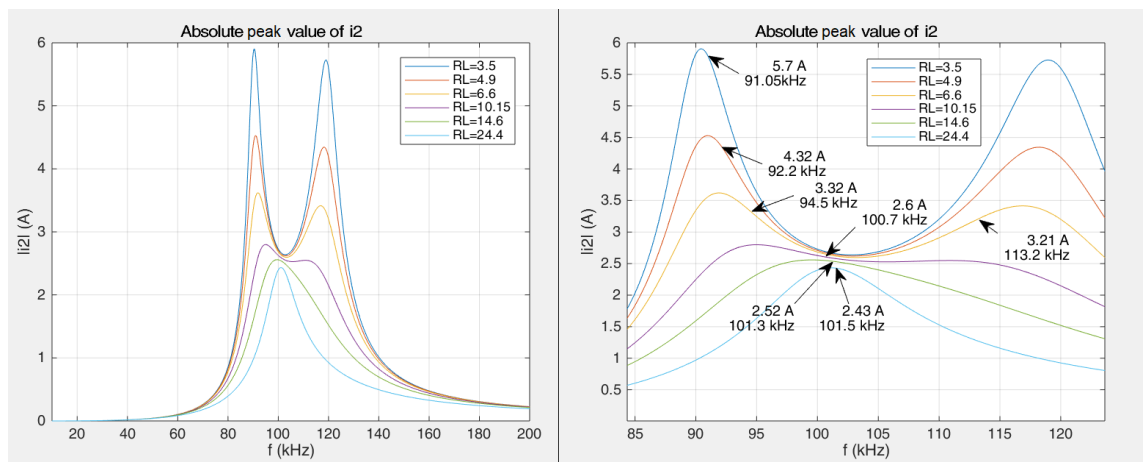


Figure 9.9: Plot of  $i_2$  absolute peak value depending on the operating frequency and at different  $R_L$  values. In the right pictures, the points at which the  $i_1$  phase angle is zero are pointed out.



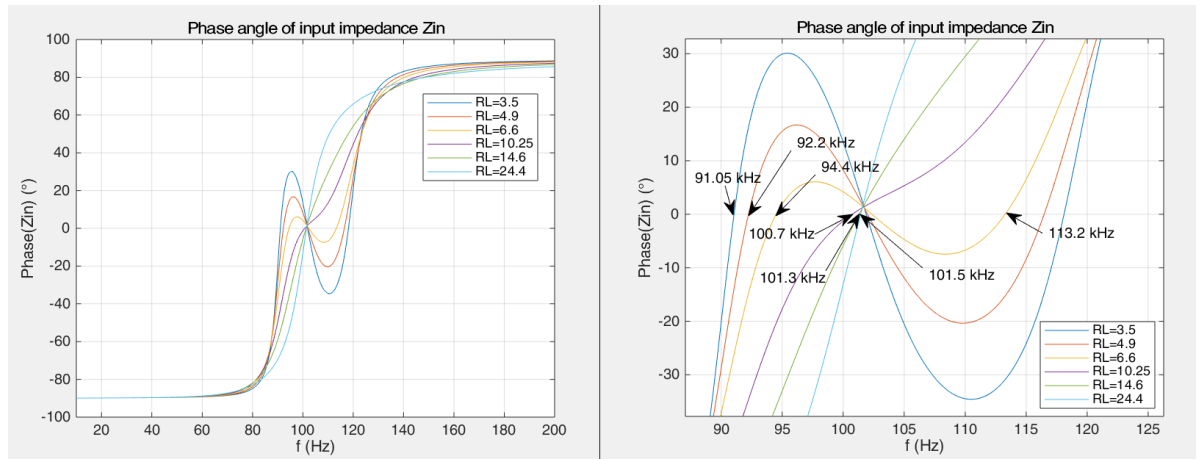


Figure 9.10: Plot of  $Z_{in}$  phase depending on the operating frequency and at different  $R_L$  values. In the right pictures, the points at which the  $i_1$  phase angle is zero are pointed out.

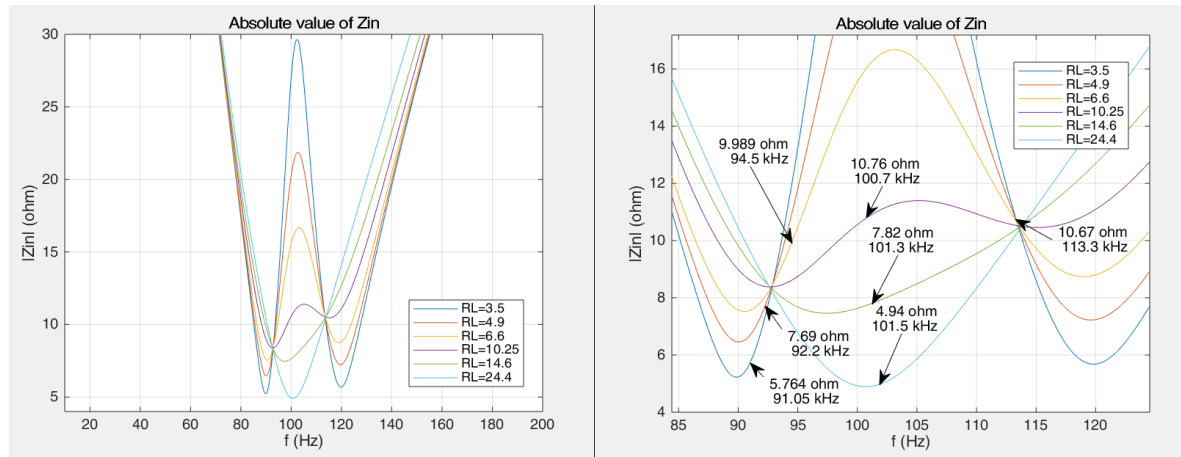


Figure 9.11: Plot of  $Z_{in}$  absolute value depending on the operating frequency and at different  $R_L$  values. In the right pictures, the points at which the  $i_1$  phase angle is zero are pointed out.

Figure 9.7, 9.8 and 9.9 are found from (3.7) and (3.8), plotting them depending on  $f$  for different values of  $R_L$ . On the other hand, Figure 9.10 and 9.11 are based on (3.6). However, it is interesting to notice that the phase angle of both  $i_1$  and  $Z_{in}$  are zero for the same operating frequency. These frequencies are pointed-out by the arrows in the right part of Figure 9.7 and 9.10. So, even if they are derived from different equations, this confirms that the model is unique.

Moreover, the ZCS operation of the inverter is achieved at those frequencies pointed-out by the arrows, since the phase angle of  $i_1$  is zero. In the right part of Figure 9.8, 9.9 and 9.11, the absolute peak value of  $i_1$  and  $i_2$ , and the absolute value of  $Z_{in}$  at the frequencies that give ZCS are found for each value of  $R_L$  and they are also pointed-out by arrows. It is interesting to notice that in both Figure 9.8 and 9.9 the arrows are not pointing at the maximum of any of  $i_1$ ,  $i_2$  curves, but the ZCS operating is happening for values slightly lower. This situation is also found in case of symmetrical primary and secondary circuits, with  $L_1 = L_2$  and  $C_1 = C_2$ . Therefore, with the inverter working at auto-resonant frequency, the operating points would be as indicated by the arrows.

On the other hand, in case the inverter would work at fixed frequency, the operating point is in correspondence of the maximum power measured at the primary circuit as shown in Figure 4.13 a). Therefore, the operating point would be at the maximum of the  $i_1$  curves in Figure 9.8. For comparing this two operating conditions, the efficiency  $\eta_{AC}$  in (9.5) is plotted in Figure 9.12. For each curve, the efficiency achieved with auto-resonant frequency operation is highlighted with a red square, and the one



achieved with fixed frequency operation is highlighted with a blue square.

$$\eta_{AC} = \frac{R_L i_2^2}{\sqrt{2} V_{in} i_1} \quad (9.5)$$

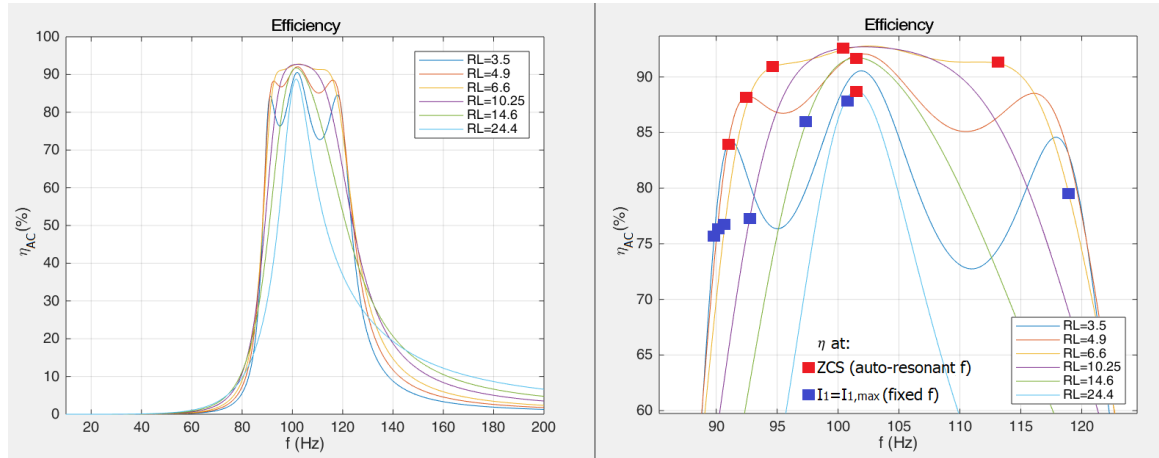


Figure 9.12: Plot of  $\eta_{AC}$  depending on the operating frequency and at different  $R_L$  values. In the right pictures, for each curve, the efficiency achieved with auto-resonant frequency operation is highlighted with a red square, and the one achieved with fixed frequency operation is highlighted with a blue square.

Figure 9.12 shows that  $\eta_{AC}$  is higher at auto-resonant frequency operation, for any load value of  $R_L$ . Moreover, this comparison between the fixed and auto-resonant frequency operation is also executed through measurements, such that the results in Figure 9.12 can be validated. The results from measurements on the setup are shown in Table 9.3, for two values of  $R_L$ . Also according to Table 9.3, the efficiency  $\eta_{AC}$  of the e-bike WPT charging system increases with the inverter working at auto-resonant frequency, compared to the case at fixed frequency.

Table 9.3: Power transfer efficiency at both ZCS and  $I_1 = I_{1,max}$  conditions, for two values of  $R_L$ .

$R_L$	$V_{in}$	Operating point	Frequency		$I_{1,max}$	$I_{2,max}$	$\eta_{AC}$
10.5 $\Omega$	20.05 V	$I_1 = I_{1,max}$	Fixed	93.5 kHz	3.38 A	2.62 A	75.2 %
	20.05 V	ZCS	Auto-resonant	97.8 kHz	2.9 A	2.58 A	85 %
14.6 $\Omega$	20.03 V	$I_1 = I_{1,max}$	Fixed	96.5 kHz	3.68 A	2.3 A	74%
	20.03 V	ZCS	Auto-resonant	100.7 kHz	3.46 A	2.28 A	77.4 %

Both results from Figure 9.12 and Table 9.3 are obtained considering the e-bike WPT charging system without the diode-bridge rectifier. However, similar results would be achieved in case the rectifier is included, with a lower total efficiency because of the voltage drop of the diodes.

## 9.2. Results and performance of the inner control loop

In Section 9.1 the experimental results are compared to the theoretical ones, which are found from the equivalent circuit's equations. In this Section 9.2, the results of set-up with the inner control loop that automatically sets the ZCS operation from the derivative of  $i_1$  are shown. Firstly, the start-up

transient is discussed and secondly, the steady-state operation. All these measurements are executed at  $V_{in} = 48 \text{ V}$ ,  $k = 0.28$  and  $R_L = 12 \Omega$ .

### 9.2.1. Start-up transient

Figure 9.13 and 9.14 show the start-up waveforms of the charging operation. Figure 9.13 a) shows that the primary voltage  $v_{AB}$  and current  $i_1$  take about 8 ms to reach the steady-state operation. In this picture, the waveforms are not clearly visible, and this is just used to evaluate the duration of the initial transient. These are plotted clearly in Figure 9.14.

On the other hand, Figure 9.13 b) shows the start-up transient of  $v_{ref+}$  and  $v_{ref-}$ . The starting procedure is done connecting the two  $v_{ref}$  through a button-switch, such that the two reference voltages drops to zero from their off-set values  $V_0$  and the comparators can start working. If  $V_0$  is higher than the first current pulses and the operation would not start if it is not lowered to zero. However, since the start button is pressed manually,  $v_{ref}$  stays to its low value for several dozens of milliseconds and this time depends on the duration of the switch press. At that time the current has already reached its steady-state value. Once the switch is released,  $v_{ref}$  jumps quickly to the new value, depending on the derivative of the current at the zero crossing.

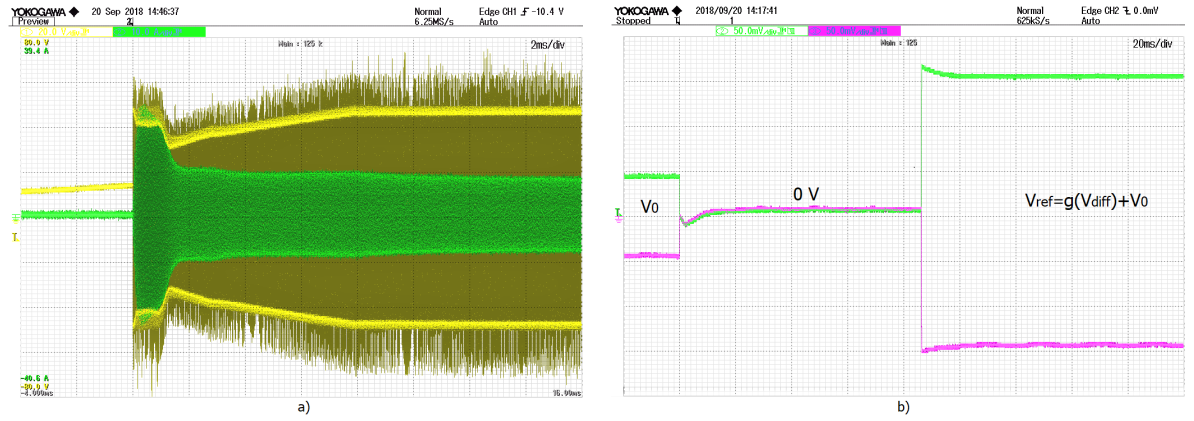


Figure 9.13: Start-up waveforms. a) The yellow waveform (channel 1) is the inverter voltage at the primary circuit  $v_{AB}$  and the green waveform (channel 2) is the primary current  $i_1$ . b) The green waveform (channel 2) is the voltage reference of the negative-current-slope comparator  $v_{ref-}$  and the purple waveform (channel 3) is the positive-current-slope comparator  $v_{ref+}$ .

Figure 9.14 a) and b) are a zoom-in overview on the waveforms of Figure 9.13. Since  $V_{ref}$  is approximately 0V at the starting, the ZCS is not achieved. However, this is acceptable for the first hundreds of seconds and, as soon as the switch is released, the phase shift between  $v_{AB}$  and  $i_1$  drops to zero.

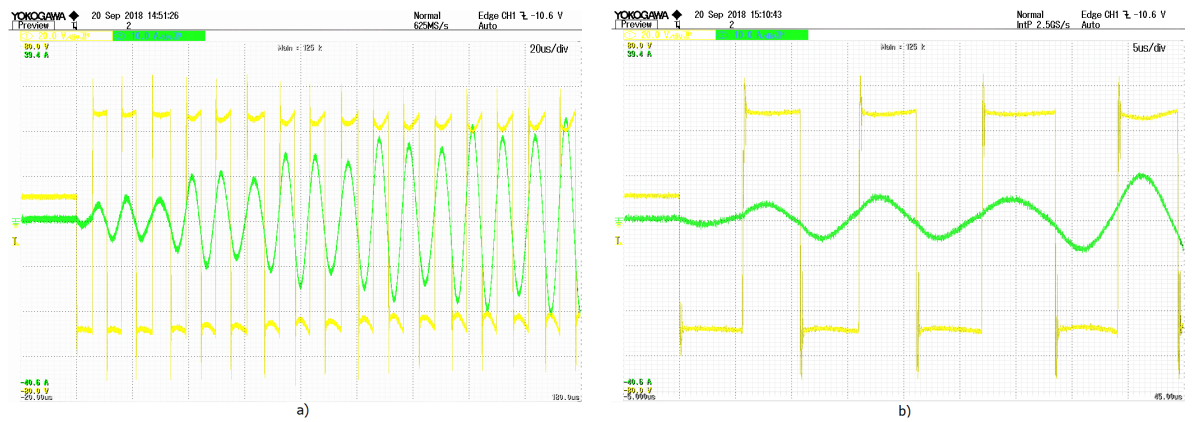


Figure 9.14: Start-up waveforms. The yellow waveform (channel 1) is the inverter voltage at the primary circuit  $v_{AB}$  and the green waveform (channel 2) is the primary current  $i_1$ . Time scale: a) 20  $\mu\text{s}/\text{div}$ , b) 5  $\mu\text{s}/\text{div}$ .

### 9.2.2. Steady-state operation

Figure 9.15 and 9.16 shows the steady-state waveforms of  $v_{AB}$  and  $i_1$  at  $V_{in} = 48$  V,  $k = 0.28$  and  $R_L = 12 \Omega$ . The ZCS operation is automatically achieved in the system, since  $v_{AB}$  and  $i_1$  are in phase. This condition is also kept if one or more of the parameters  $V_{in}$ ,  $k$ ,  $R_L$  is changed.

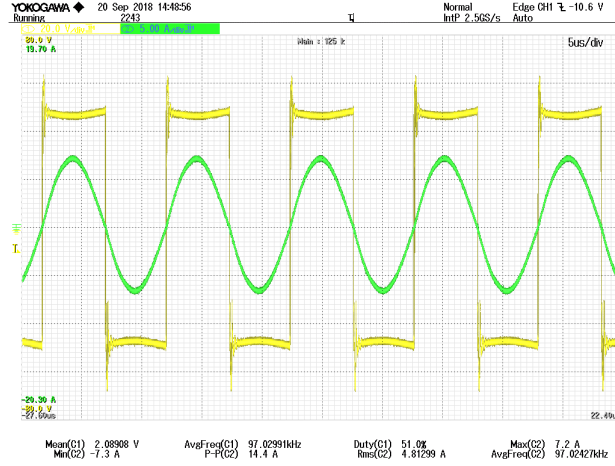


Figure 9.15: Steady-state waveforms. The yellow waveform (channel 1) is the inverter voltage at the primary circuit  $v_{AB}$  and the green waveform (channel 2) is the primary current  $i_1$ .

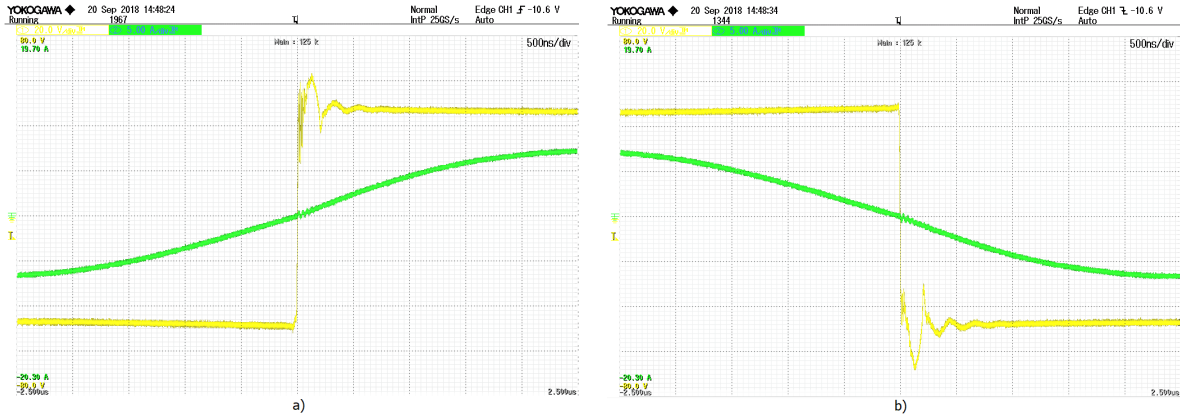


Figure 9.16: Zoom-in of the waveforms in Figure 9.15: a) positive-slope and b) negative-slope zero-crossing of  $i_1$ .

Moreover, in Table 9.4 are reported the DC input and output voltage and current, which are measured at the input of the primary inverter and across the secondary resistive load, respectively. The total efficiency  $\eta_{DC}$  of the system is also calculated, as the ratio between the output and the input power.

Table 9.4: Measured input and output DC voltage and current at  $V_{in} = 48$  V,  $k = 0.28$  and  $R_L = 12 \Omega$ .

$k$	$R_L$	$V_{in}$	$I_{in}$	$V_{out}$	$I_{out}$	$\eta_{DC}$
0.28	$12 \Omega$	48.04 V	4.67 A	45.53 V	3.91 A	79.34 %

The efficiency value reported in Table 9.4 need to be treated cautiously, because it involves the entire system efficiency while in this project just the control circuit for the primary inverter is optimized. Therefore, that number can easily increase optimizing the sub-circuits that were already part of the charging system. As an example, the full-bridge inverter and especially the diode-bridge rectifier, that could be replaced with a synchronous rectifier made of voltage-controlled switches. However, these issues were not part of this thesis project, because of lack of time.



# 10

## Conclusion

The Wireless Power Transfer (WPT) has been introduced decades ago for low power applications, and more recently, it has been used for industrial high power applications. WPT is gaining popularity because it presents several advantages over the power transfer through cable, such as the galvanic insulation between the power source and the load, the possibility of on-road charging for private EVs, and it obviates the need of bringing around bulky cables of portable devices, especially the ones not standardized yet.

The subject of this thesis is an e-bike WPT charging system, using electromagnetic power transfer with resonant coupling. The WPT works through two coupled ferromagnetic coils with compensation capacitors. In particular, this thesis focuses on the control of the inverter of the e-bike WPT charging system. Chapter 1 is the introduction, and it gives some background on the WPT. Chapter 2 defines the problem treated in this project, explaining the whole e-bike WPT charging system with its goals and constraints. Chapter 3 analyses both the inductive and the resonant coupling, including the possible compensation networks. Chapter 4 discusses power electronics topologies for both the primary and the secondary converters. Chapter 5 compares the S-S and LCC compensation networks for the e-bike WPT charging system. Chapter 6 presents control strategies for the inner and outer control loops. Chapter 7 discusses the existing communication standards for WPT, focusing in detail on the Qi specification from the Wireless Power Consortium. Chapter 8 explains the design of the inner control loop for the primary inverter. Chapter 9 consists of the theoretical model validation with measurements on the set-up. Finally, Chapter 10 contains the conclusions on the e-bike WPT charging system in Section 10.1, and recommendations for future research on this topic in Section 10.2.

In Chapter 2, the goals of the e-bike WPT charging system are listed in Table 2.2. All of them have been part of the literature research, but just some of them have been designed and implemented. These goals are mentioned again in Table 10.1, specifying their actual state in the project, such that the overall progress is summarized.

Table 10.1: Goals of the e-bike WPT charging system, specifying their actual state in the project.

<b>Efficiency and Power Factor (PF)</b>	<b>Actual state</b>
Unity PF for maximizing the power transfer.	Implemented
Maximize the power transfer efficiency at each coupling factor, choosing the most suitable inverter topology and compensation network.	
Minimize the inverter and rectifier losses.	
<b>Operation</b>	<b>Actual state</b>
Automatic adjustment of the operating point using the inner control loop.	Implemented
Implementation of the outer control loop for the communication between the transmitter and receiver.	Literature research
Suitable start up and shut down strategy.	
<b>Safety and protections</b>	<b>Actual state</b>
Overvoltage and overcurrent protection.	Literature research
Foreign object detection.	
Sleep-mode/standby option.	

### 10.1. Conclusions on the e-bike WPT charging system.

As conclusions, five considerations on the e-bike WPT charging system are pointed out.

1. The literature research, simulations and theoretical models are crucial stages of the project. Through these stages, a solid and strong knowledge on the topic can be built, such that the design and implementation stages are easier to handle.
2. The validation of the theoretical model with experimental results is the most important stage of the project. This stage allows to verify the correctness of the model and, eventually, to improve it. In particular, the model validation executed in Section 9.1 shows that the equivalent circuit of the S-S compensation network in Figure 3.4 approximates well the behavior of the e-bike WPT charging system, only if the rectifier is not included in the set-up. Once the rectifier is included, the theoretical model does not match the set-up behavior accurately. Therefore, an improved equivalent circuit must be found for predicting the real e-bike WPT charging system.
3. An improvement in the definition of the bifurcation phenomenon is necessary. The definition present in the literature is not satisfying, because it assumes that the primary and secondary circuits are perfectly tuned at the same resonant frequency, as explained in Section 3.3.3. In case the two circuits are not perfectly tuned, the resulting  $R_{L,min}$  would be the correct condition for a bifurcation-free operation. Moreover, according to the numerical example shown in Section 6.2.1, even if  $R_L$  satisfies the condition for a bifurcation-free operation, when  $k$  is low, the power level could be several times higher than the rated one. Therefore, the condition found in the literature does not ensure a safe operation.
4. The auto-resonant frequency operation of the inverter can be reached by finding the proper relation between the slope of the current at the zero-crossing, and the reference values of the comparators. Using this method, the inner control loop adapts automatically the operating point in case any of the circuit parameters changes. The auto-resonant frequency operation is also flexible, because the positive and the negative slopes of the current are treated separately.
5. The e-bike WPT charging system working at auto-resonant frequency have a higher efficiency than when it is working at fixed frequency. Initially, in Section 9.1, this result is found through the plot of the efficiency  $\eta_{AC}$  in Figure 9.6, using a numerical equation solver. For lower values of  $R_L$  ( $R_L < 11 \Omega$ ), the efficiency  $\eta_{AC}$  at auto-resonant frequency is up to 15% higher than at fixed frequency. For higher values of  $R_L$ , the difference between the two efficiencies is smaller, but the auto-resonant frequency still gives the higher efficiency. The measurements on the set-up confirm these results, as it is shown in Table 9.3. At  $R_L = 10 \Omega$ , the efficiency at fixed frequency is 75.2%, and at auto-resonant frequency is 85%. At  $R_L = 14 \Omega$ , the efficiency at fixed frequency is 74%, and auto-resonant frequency is 77.4%. Therefore, it is possible to achieve a better performance

with an analog, simple, cheap and fast inner control loop, avoiding complex programming of digital signals.

## 10.2. Recommendations for future research

This thesis project could be used as a starting point for several types of research on the e-bike WPT charging system, which have not been executed because of lack of time. In particular, five recommendations are pointed out.

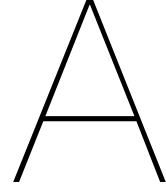
1. The inner control circuit and the FB inverter could be integrated in the same PCB, such that long connections are avoided, for having as small disturbances as possible.
2. Both the FB inverter and the diode-bridge rectifier could be optimized for minimizing their losses. In this project, the total efficiency of the e-bike WPT charging system has been calculated, and it is found to be  $\eta_{DC} \approx 80\%$ . However, this value is just an indication, because  $\eta_{DC}$  could be easily increased by replacing the diodes with actively controlled switches, such that both conduction and switching losses are lowered. Since the voltage drop in the rectifier would be lower using the switches, the theoretical model based on the equivalent circuit could match better the measurements on the e-bike WPT charging system, when the rectifier is included. Therefore, a synchronous rectifier could be used instead of the diode-bridge rectifier.
3. The design and the implementation of the outer control loop could be executed, according to the literature research in Chapter 7, which consists in the communication between the transmitter and the receiver. Therefore, the communication has to be programmed using the ASK modulation, as described in Chapter 7. The outer control loop should also include start-up and shut-down strategies, sleep mode, FOD and circuit protections.
4. The DC/DC converters could be included in the e-bike WPT charging system, such that they work in combination with the outer control loop for controlling the power transfer. In particular, a buck converter should be placed at the input of the primary inverter, such that the input power can be stepped down, and a buck/boost converter should be placed between the secondary rectifier output and the load, such that the output voltage can be kept constant to its nominal value.
5. A system that tunes the primary and secondary circuits automatically to the same resonant frequency should be developed. This tuning system could be realized using variable capacitors. The reason for this is that the circuit parameters are not constant during the operation as it is assumed in the theoretical analysis. The primary and secondary coil inductances are highly dependent on their coupling and, on top of that, all the parameters change depending on their actual conditions, such as temperature, voltage and current stress. Therefore, it is really probable that the primary and the secondary circuits are not tuned to the same resonant frequency, which means that the power transfer is not maximized, and the theoretical analysis is not valid since it is based on tuned circuits.





# **Appendices**





## Primary compensation capacitor $C_1$ calculation

The primary compensation capacitor  $C_1$  is chosen such that the imaginary part of the equivalent input impedance  $Z_{in}$  in Figure 3.2 is zero at the resonant frequency.  $Z_{in}$  is found combining the primary circuit equivalent inductance with the reflected inductance  $Z_r$  in Table A.1. [10] The resulting  $Z_{in}$  are reported in Table A.2 for all the compensation topologies.

The formula of  $C_1$  in Table 3.1 can be found imposing the imaginary part of  $Z_{in}$  equal to zero.

Table A.1: Reflected inductance  $Z_r$  on the primary circuit.

S-S and P-S topology	$Z_2 = R_2 + R_L + j\omega L_2 + \frac{1}{j\omega C_2}$	$Z_r = \frac{\omega^2 M^2}{Z_2} = \frac{\omega^2 M^2}{R_2 + R_L + j\omega L_2 + \frac{1}{j\omega C_2}}$
S-P and P-P topology	$Z_2 = R_2 + j\omega L_2 + \frac{1}{j\omega C_2 + \frac{1}{R_L}}$	$Z_r = \frac{\omega^2 M^2}{Z_2} = \frac{\omega^2 M^2}{R_2 + j\omega L_2 + \frac{1}{j\omega C_2 + \frac{1}{R_L}}}$

Table A.2: Primary compensation capacitance  $C_1$  for all the compensation topologies.

S-S topology	$Z_{in} = Z_r + R_1 + j\omega L_1 + \frac{1}{j\omega C_1} = \frac{M^2 \omega^2}{R_2 + R_L + j\omega L_2 + \frac{1}{j\omega C_2}} + R_1 + j\omega L_1 + \frac{1}{j\omega C_1}$
S-P topology	$Z_{in} = Z_r + R_1 + j\omega L_1 + \frac{1}{j\omega C_1} = \frac{\omega^2 M^2}{R_2 + j\omega L_2 + \frac{1}{j\omega C_2 + \frac{1}{R_L}}} + R_1 + j\omega L_1 + \frac{1}{j\omega C_1}$
P-S topology	$Z_{in} = \frac{1}{j\omega C_1 + \frac{1}{Z_r + R_1 + j\omega L_1}} = \frac{1}{j\omega C_1 + \frac{1}{\frac{\omega^2 M^2}{R_2 + R_L + j\omega L_2 + \frac{1}{j\omega C_2}} + R_1 + j\omega L_1}}$
P-P topology	$Z_{in} = \frac{1}{j\omega C_1 + \frac{1}{Z_r + R_1 + j\omega L_1}} = \frac{1}{j\omega C_1 + \frac{1}{\frac{\omega^2 M^2}{R_2 + j\omega L_2 + \frac{1}{j\omega C_2 + \frac{1}{R_L}}} + R_1 + j\omega L_1}}$

# B

## Equivalent circuit and calculation of double-sided LCC compensation

Figure B.1 a) is the equivalent circuit of the double-sided LCC compensation circuit in Figure 3.15, treating the coupled coils as a transformer. The turns ratio is considered to be one, such that the secondary parameters do not have to be referred to the primary circuit.  $L_m = kL_1$  is the magnetizing inductance and  $L_{p1} = (1 - k)L_1$  and  $L_{p2} = (1 - k)L_2$  are respectively the primary and secondary leakage inductance. (3.28), (3.29), (3.30), (3.31), (3.32), and (3.33) are the results of the superposition principle applied to the circuit in Figure B.1 a), for understanding the influence of the input  $V_{AB}$  and output  $V_{ab}$  voltage. Firstly, the currents in the circuit are calculated applying an input voltage  $V_{AB}$  and short-circuiting the output voltage  $V_{ab}$  as shown in Figure B.1 b). Secondly, the currents in the circuit are calculated short-circuiting the input voltage  $V_{AB}$  and applying an output voltage  $V_{ab}$  as shown in Figure B.1 c). Finally, the currents calculated in both cases are summed up and the final results are found.

In both Figures B.1 b) and c) the dashed circuit legs mean that no current flowing there. Moreover, the series  $C_1 - L_{p1}$  and  $C_2 - L_{p2}$  are rewritten as

$$L_{e1} = \frac{1}{j\omega_0} \left( \frac{1}{j\omega_0 C_1} + j\omega_0 L_{p1} \right) = L_{f1} - kL_1 \quad (\text{B.1})$$

$$L_{e2} = \frac{1}{j\omega_0} \left( \frac{1}{j\omega_0 C_2} + j\omega_0 L_{p2} \right) = L_{f2} - kL_1 \quad (\text{B.2})$$

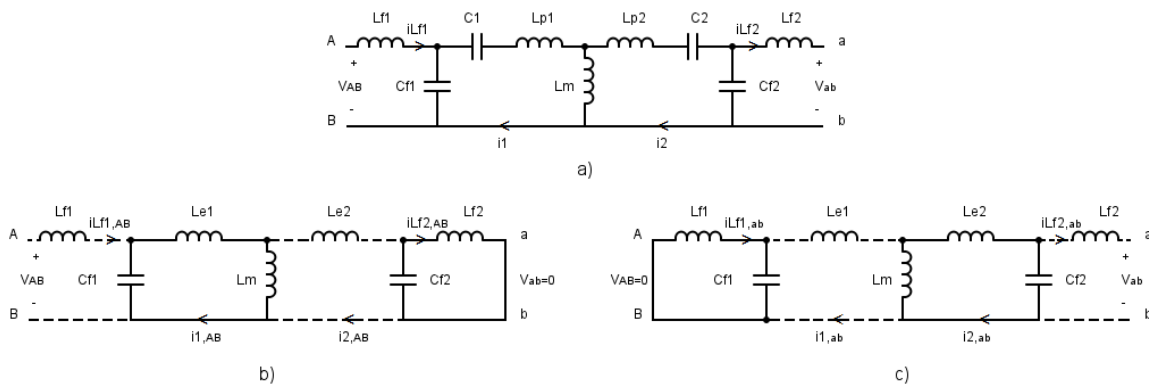


Figure B.1: a) Equivalent circuit of the double-sided LCC compensation, treating the coupled inductors as a transformer. b) Equivalent circuit of LCC based on superposition principle: a input voltage applied an the output is shorted. c) Equivalent circuit of LCC based on the superposition principle: input is shorted and a output voltage is applied.

*Superposition 1 - Figure B.1 b)*

$C_{f2}$  and  $C_{f2}$  are connected in parallel because the circuit terminals  $a$  and  $b$  are shorted. When the circuit is operating at the resonant frequency, this parallel consists in a resonant parallel that is equal to a open circuit. So, there is no current flowing through  $L_{e2}$

$$I_{2,AB} = 0. \quad (B.3)$$

$L_{e1}$  and  $L_m$  are then connected in series such that

$$L_{e1} + L_m = L_{f1} - kL_1 + kL_1 = L_{f1} \quad (B.4)$$

Since this series is in parallel with  $C_{f1}$ , also in this case this parallel consists in a resonant parallel that is equal to a open circuit. So, there is no current flowing through  $L_{f1}$

$$I_{L_{f1},AB} = 0. \quad (B.5)$$

$I_{1,AB}$  and  $I_{L_{f2},AB}$  can be found considering that the  $V_{C_{f2}} = V_{L_m}$  and  $V_{C_{f1}} = V_{AB}$ .

$$I_{1,AB} = \frac{V_{AB}}{j\omega_0 L_{f1}} \quad (B.6)$$

$$I_{L_{f2},AB} = \frac{kV_{AB}L_1}{j\omega_0 L_{f1}L_{f2}} \quad (B.7)$$

*Superposition 2 - Figure B.1 c)*

The same method applied also in this second superposition, leading to

$$I_{1,ab} = 0 \quad (B.8)$$

$$I_{L_{f2},ab} = 0 \quad (B.9)$$

$$I_{1,ab} = \frac{-V_{ab}}{j\omega_0 L_{f2}} \quad (B.10)$$

$$I_{L_{f1},ab} = \frac{-kV_{ab}L_1}{j\omega_0 L_{f1}L_{f2}} \quad (B.11)$$

Finally, (3.29), (3.30), (3.32) and (3.33) can be found summing up (B.5)+(B.11), (B.6)+(B.8), (B.3)+(B.10), and (B.7)+(B.9).

The results are then verified with simulations using the parameters in Table 5.1 with  $R_L = 5$  and  $k = 0.25$ . Figure B.2 shows that  $V_{AB}$  and  $I_{L_{f1}}$  are in phase. Figure B.3 shows that  $V_{ab}$  and  $I_{L_{f2}}$  are in phase. Finally, Figure B.4 shows that  $I_{L_{f2}}$  leads  $I_{L_{f1}}$  of  $90^\circ$ . Moreover,  $I_2$  is in phase with  $I_{L_{f1}}$  and  $I_1$  is in phase with  $I_{L_{f2}}$ .

The currents' amplitude and their phase shift match the calculations.

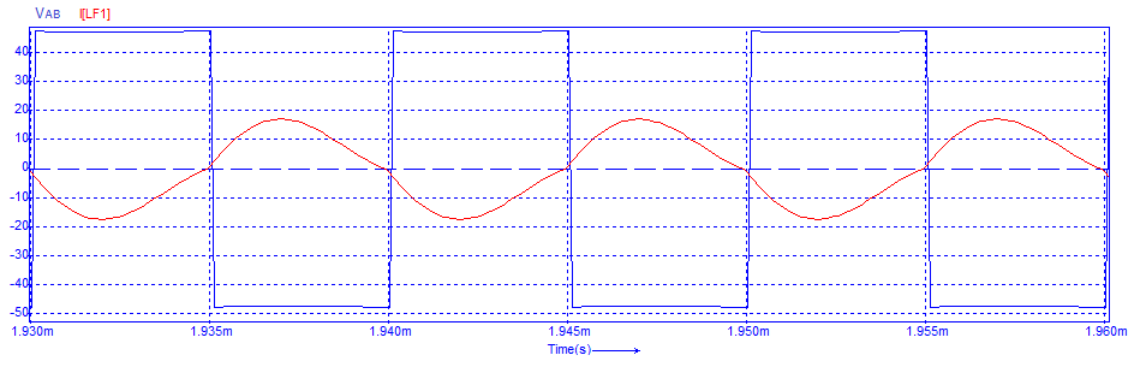


Figure B.2: Simulated  $V_{AB}$  and  $I_{Lf1}$ .

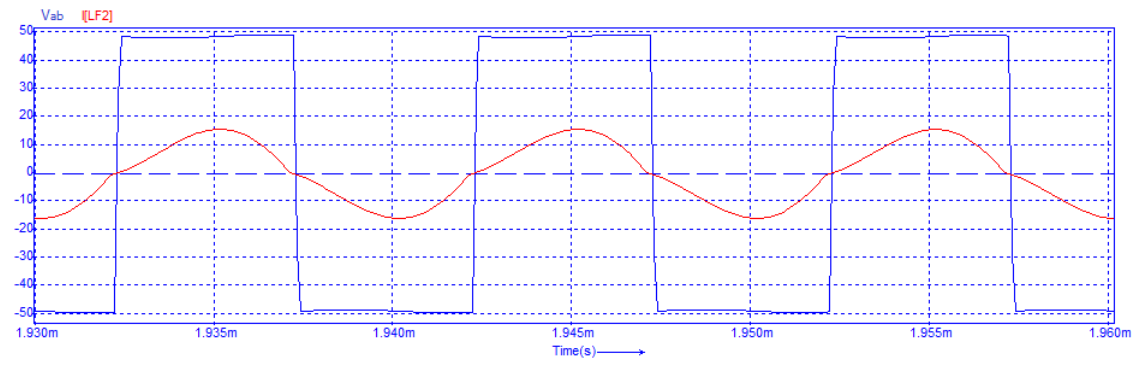


Figure B.3: Simulated  $V_{ab}$  and  $I_{Lf2}$ .

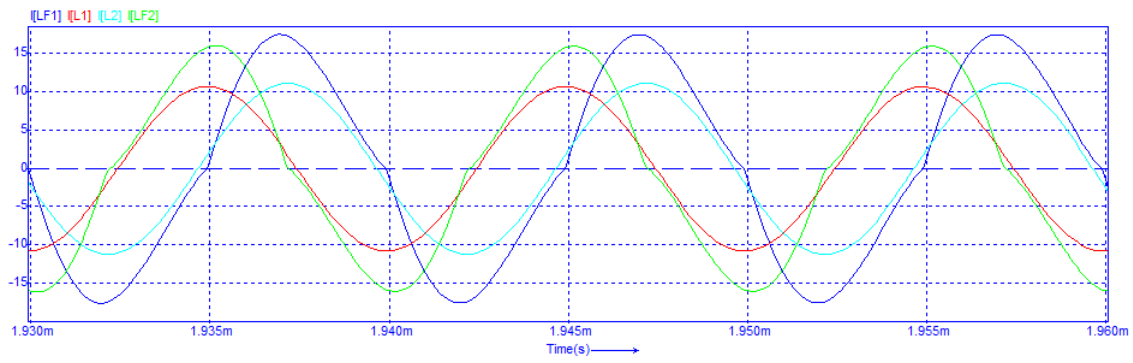
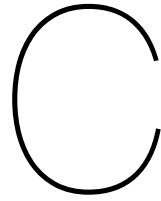


Figure B.4: Simulated  $I_{Lf1}$ ,  $I_{L1}$ ,  $I_{L2}$  and  $I_{Lf2}$ .







## Matlab Code of the equivalent circuit

In this chapter, the Matlab code used to plot the equivalent model's results is attached.

```
1 %% clear all
2
3 clear all; close all;
4 %% Parameters
5 j=1i;
6 Vin=20*sqrt(2);
7 L1=70.28*10^(-6);
8 C1=35*10^(-9);
9 L2=70.28*10^(-6);
10 C2=35*10^(-9);
11 k=0.28;
12 f2=1/(sqrt(L2*C2)*2*pi);
13 M=k*sqrt(L1*L2);
14 w0=1/sqrt((L1)*C1);
15 f0=w0/(2*pi);
16 RL=20;
17 R1=0.5;
18 R2=0.3;
19
20 %% Calculations
21
22 d=1;
23 a=1;
24 for RL=4:2:14
25     if RL==4
26         RL=3.5;
27     end
28     if RL==6
29         RL=4.9;
30     end
31     if RL==8
32         RL=6.6;
33     end
34     if RL==10
35         RL=10.15;
36     end
37     if RL==12
38         RL=14.6;
39     end
40     if RL==14
41         RL=24.4;
42     end
43     c=1;
44     for w=0:500:1300000
45
46         den(c,d)=R2+RL+j*w*L2+1/(j*w*C2)+(w^2*M^2)/(R1+j*w*L1+1/(j*w*C1));
47         i2(c,d)=-(j*w*M*Vin)/(R1+j*w*L1+1/(j*w*C1))*(1/den(c,d));
48
49         i1(c,d)=(Vin-j*w*M*i2(c,d))/(R1+j*w*L1+1/(j*w*C1));
```

```

50 i1_mod(c,d)=abs(i1(c,d));
51 i1_real(c,d)=real(i1(c,d));
52 i1_imag(c,d)=imag(i1(c,d));
53 i1_phase(c,d)=atan(imag(i1(c,d)/real(i1(c,d))))*180/pi;
54 if (imag(i1(c,d))<0 && real(i1(c,d)<0)) || (imag(i1(c,d))>0 && real(i1(c,d)<0))
55     i1_phase(c,d)=i1_phase(c,d)-180;
56 end
57
58 i2_mod(c,d)=abs(i2(c,d));
59 i2_phase(c,d)=atan(imag(i2(c,d)/real(i2(c,d))))*180/pi;
60 i2_real(c,d)=real(i2(c,d));
61 i2_imag(c,d)=imag(i2(c,d));
62 if (imag(i2(c,d))<0 && real(i2(c,d)<0)) || (imag(i2(c,d))>0 && real(i2(c,d)<0))
63     i2_phase(c,d)=i2_phase(c,d)-180;
64 end
65
66 v1(c,d)=Vin-(R1+1/(j*w*C1))*i1(c,d);
67 v1_mod(c,d)=abs(v1(c,d));
68 v1_phase(c,d)=atan(imag(v1(c,d)/real(v1(c,d))))*180/pi;
69 if (imag(v1(c,d))<0 && real(v1(c,d)<0)) || (imag(v1(c,d))>0 && real(v1(c,d)<0))
70     v1_phase(c,d)=v1_phase(c,d)+180;
71 end
72
73 v2(c,d)=-(i2(c,d)*(-R2-RL-1/(j*w*C2)));
74 v2_mod(c,d)=abs(v2(c,d));
75 v2_phase(c,d)=atan(imag(v2(c,d)/real(v2(c,d))))*180/pi;
76 if ((imag(v2(c,d))>0 && real(v2(c,d)<0)) || (imag(v2(c,d))<0 && real(v2(c,d)<0)))
77     v2_phase(c,d)=v2_phase(c,d)-180;
78 end
79 if ((imag(v2(c,d))>0 && real(v2(c,d)>0)))
80     v2_phase(c,d)=v2_phase(c,d)-360;
81 end
82
83 vout=i2*RL;
84 vout_mod(c,d)=abs(vout(c,d));
85 vout_phase(c,d)=atan(imag(vout(c,d)/real(vout(c,d))))*180/pi;
86 if ((imag(vout(c,d))<0 && real(vout(c,d)<0)) || (imag(vout(c,d))>0 && real(vout(c,d)<0)))
87     vout_phase(c,d)=vout_phase(c,d)-180; Zs=R2+RL+j*w*L2+1/(j*w*C2);
88 end
89
90 Zs(c,d)=R2+RL+j*w*L2+1/(j*w*C2);
91 Zr(c,d)=(w*k*sqr(L1*L2))^2/Zs(c,d);
92 Zin(c,d)=R1+j*w*L1+1/(j*w*C1)+Zr(c,d);
93 Zin_mod(c,d)=abs(Zin(c,d));
94 Zin_phase(c,d)=atan(imag(Zin(c,d)/real(Zin(c,d))))*180/pi;
95
96 Gv(c,d)=(RL)*abs(i2(c,d))/Vin;
97 Gi(c,d)=abs(i2(c,d))/abs(i1(c,d));
98 load(c,d)=RL;
99
100 PF(c,d)=cosd(Zin_phase(c,d));
101 eff(c,d)=load(c,d)*(abs(i2(c,d)))^2/(Vin*abs(i1(c,d)));
102
103 w_vect(c,d)=w/(2*pi*1000);
104 c=c+1;
105 end
106
107 d=d+1;
108 end
109
110 Gv(Gv==0)=nan; Gi(Gi==0)=nan;
111 Zin_mod(Zin_mod==(0+j*0))=nan; Zin_phase(Zin_phase==(0+j*0))=nan;
112 i1_mod(i1_mod==(0+j*0))=nan; i1_phase(i1_phase==(0+j*0))=nan;
113 i2_mod(i2_mod==(0+j*0))=nan; i2_phase(i2_phase==(0+j*0))=nan;
114 v1_mod(i2_mod==(0+j*0))=nan; v1_phase(i2_phase==(0+j*0))=nan;
115 v2_mod(i2_mod==(0+j*0))=nan; v2_phase(i2_phase==(0+j*0))=nan;
116 vout_mod(i2_mod==(0+j*0))=nan; vout_phase(i2_phase==(0+j*0))=nan;
117
118 %% Plot Gv Gi eff PF Zin
119 figure(1)
120 P=plot(w_vect,Gv);

```

```

121 axis([10 200 0 2]);
122 xlabel('f (Hz)');
123 ylabel('Gv=Vout/Vin');
124 legend('RL=3.5','RL=4.9','RL=6.6','RL=10.25','RL=14.6','RL=24.4');
125 grid ON
126
127 figure(2)
128 P=plot(w_vect, Gi);
129 title('Current Gain Gi');
130 axis([10 200 0 3.5]);
131 xlabel('f (Hz)');
132 ylabel('Gi=Iout/Iin');
133 legend('RL=3.5','RL=4.9','RL=6.6','RL=10.25','RL=14.6','RL=24.4');
134 grid ON
135
136 figure(3)
137 P=plot(w_vect, eff);
138 title('Efficiency');
139 axis([10 200 0 1]);
140 xlabel('f (Hz)');
141 ylabel('eff (p.u.)');
142 legend('RL=3.5','RL=4.9','RL=6.6','RL=10.25','RL=14.6','RL=24.4');
143 grid ON
144
145 figure(4)
146 P=plot(w_vect, PF);
147 title('Power Factor');
148 axis([10 200 0 1]);
149 xlabel('f (Hz)');
150 ylabel('PF (p.u.)');
151 legend('RL=3.5','RL=4.9','RL=6.6','RL=10.25','RL=14.6','RL=24.4');
152 grid ON
153
154 figure(5)
155 P=plot(w_vect, Zin_mod);
156 title('Absolute value of Zin');
157 axis([10 200 4 50]);
158 xlabel('f (Hz)');
159 ylabel('|Zin| (ohm)');
160 legend('RL=3.5','RL=4.9','RL=6.6','RL=10.25','RL=14.6','RL=24.4');
161 grid ON
162
163 figure(6)
164 P=plot(w_vect, Zin_phase);
165 title('Phase angle of input impedance Zin');
166 axis([10 200 -100 100]);
167 xlabel('f (Hz)');
168 ylabel('Phase(Zin) (°)');
169 legend('RL=3.5','RL=4.9','RL=6.6','RL=10.25','RL=14.6','RL=24.4');
170 grid ON
171 %% Plot of i1 i2
172 figure(7)
173 P=plot(w_vect, i1_mod);
174 title('Absolute value of i1');
175 axis([10 200 0 7]);
176 xlabel('f (kHz)');
177 ylabel('|i1| (A)');
178 legend('RL=3.5','RL=4.9','RL=6.6','RL=10.25','RL=14.6','RL=24.4');
179 grid ON
180
181 figure(8)
182 P=plot(w_vect, i1_phase);
183 title('Phase angle of i1');
184 axis([10 200 -100 100]);
185 xlabel('f (kHz)');
186 ylabel('Phase(i1) (°)');
187 legend('RL=3.5','RL=4.9','RL=6.6','RL=10.25','RL=14.6','RL=24.4');
188 grid ON
189
190 figure(9)
191 P=plot(w_vect, i2_mod);

```

```

192 title('Absolute value of i2');
193 axis([10 200 0 7]);
194 xlabel('f (kHz)');
195 ylabel('|i2| (A)');
196 legend('RL=3.5','RL=4.9','RL=6.6','RL=10.25','RL=14.6','RL=24.4');
197 grid ON
198
199 figure(10)
200 P=plot(w_vect, i2_phase);
201 title('Phase angle of i2');
202 axis([10 200 -300 100]);
203 xlabel('f (kHz)');
204 ylabel('Phase(i2) (°)');
205 legend('RL=3.5','RL=4.9','RL=6.6','RL=10.25','RL=14.6','RL=24.4');
206 grid ON
207
208 %% Plot of v1 v2 vout
209 figure(11)
210 P=plot(w_vect, v1_mod);
211 title('Absolute value of V1');
212 axis([10 200 0 350]);
213 xlabel('f (Hz)');
214 ylabel('|V1| (V)');
215 legend('RL=3.5','RL=4.9','RL=6.6','RL=10.25','RL=14.6','RL=24.4');
216 grid ON
217
218
219 figure(12)
220 P=plot(w_vect, v1_phase);
221 title('Phase angle of V1');
222 axis([10 200 0 200]);
223 xlabel('f (Hz)');
224 ylabel('Phase(V1) (°)');
225 legend('RL=3.5','RL=4.9','RL=6.6','RL=10.25','RL=14.6','RL=24.4');
226 grid ON
227
228 figure(13)
229 P=plot(w_vect, v2_mod);
230 title('Absolute value of V2');
231 axis([10 200 0 350]);
232 xlabel('f (Hz)');
233 ylabel('|V2| (V)');
234 legend('RL=3.5','RL=4.9','RL=6.6','RL=10.25','RL=14.6','RL=24.4');
235 grid ON
236
237 figure(14)
238 P=plot(w_vect, v2_phase);
239 title('Phase angle of V2');
240 axis([10 200 -400 50]);
241 xlabel('f (Hz)');
242 ylabel('Phase(V2) (°)');
243 legend('RL=3.5','RL=4.9','RL=6.6','RL=10.25','RL=14.6','RL=24.4');
244 grid ON
245
246 figure(15)
247 P=plot(w_vect, vout_mod);
248 title('Absolute value of Vout');
249 axis([10 200 0 55]);
250 xlabel('f (Hz)');
251 ylabel('|Vout| (V)');
252 legend('RL=3.5','RL=4.9','RL=6.6','RL=10.25','RL=14.6','RL=24.4');
253 grid ON
254
255 figure(16)
256 P=plot(w_vect, vout_phase);
257 title('Phase angle of Vout');
258 axis([10 200 -300 100]);
259 xlabel('f (Hz)');
260 ylabel('Phase(Vout) (°)');
261 legend('RL=3.5','RL=4.9','RL=6.6','RL=10.25','RL=14.6','RL=24.4');
262 grid ON

```

D

## PCB design

The schematic of the inverter control PCB is shown in Figure D.1. The dotted red and blue rectangles close to the external perimeter are the top and bottom ground layer, respectively. Moreover, the red connections between the components are on the top layer and the blues ones on the bottom layer. The width of both layers is  $35\text{ }\mu\text{m}$ .

The PCB size is about  $13 \times 8.5\text{ cm}$ , which is three times smaller than the initial configuration with the breadboards.

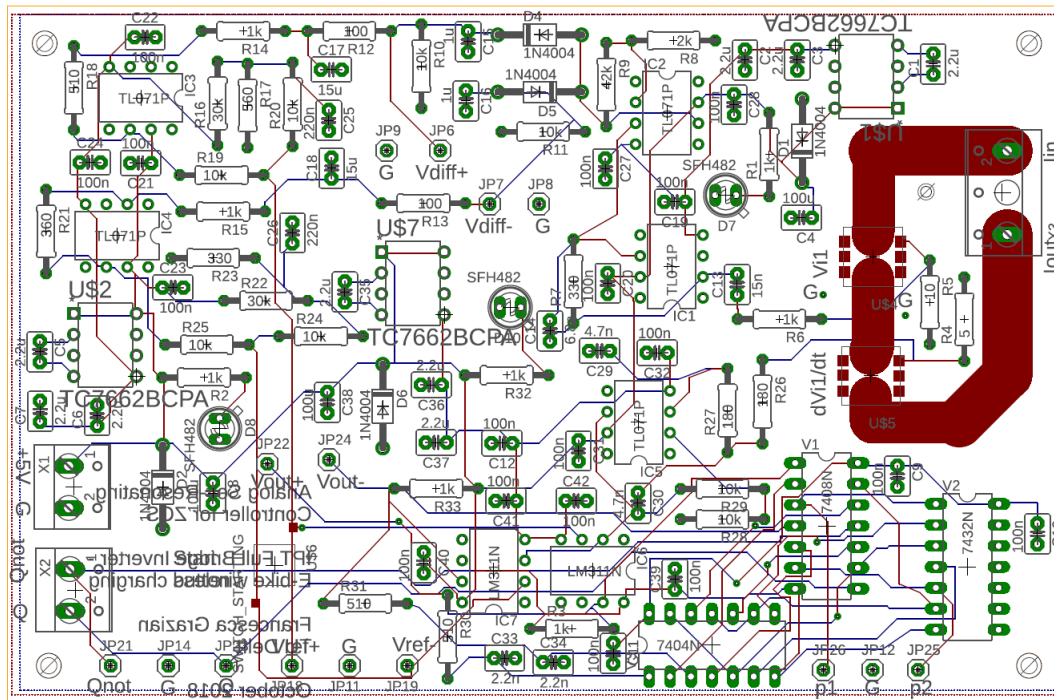


Figure D.1: Controller PCB.



# Bibliography

- [1] P. Blanchard, R. L. Devaney, and G. R. Hall, *Differential Equations*. Brooks/Cole, 2006.
- [2] L. W. Nagel, *SPICE 2: A COMPUTER PROGRAM TO SIMULATE SEMICONDUCTOR CIRCUITS*, Electronics Research Laboratory, College of Engineering University of California, Berkeley, May 1975.
- [3] W. H. Press, S. A. Teukolsky, W. T. Vetterling, and B. P. Flannery, *NUMERICAL RECIPES The Art of Scientific Computing*, 3rd ed. Cambridge University Press, 2007.
- [4] M. H. Rashid, Ed., *Power Electronics Handbook*, 4th ed. Elsevier Inc., 2018.
- [5] J. T. Boys and G. A. Covic, "Ipt fact sheet series: No. 1 – basic concepts," *Qualcomm*, 2012.
- [6] T. R. Kuphaldt, *Lessons in Electric Circuits*, D. S. License, Ed., 2017, vol. 2-AC.
- [7] S. Chopra and P. Bauer, "Analysis and design considerations for a contactless power transfer system," *Telecommunications Energy Conference (INTELEC), 2011 IEEE 33rd International*, 2011.
- [8] K. A. Kalwar, M. Aamir, and S. Mekhilef, "Inductively coupled power transfer (icpt) for electric vehicle charging – a review," *Renewable and Sustainable Energy Reviews*, no. 47, p. 462–475, Mar. 2015.
- [9] T. Velzeboer, "Sustainable & contactless charging of e-bikes," Master's thesis, Delft University of Technology, Dec. 2016.
- [10] C.-S. Wang, G. A. Covic, , and O. H. Stielau, "Power transfer capability and bifurcation phenomena of loosely coupled inductive power transfer systems," *148 IEEE TRANSACTIONS ON INDUSTRIAL ELECTRONICS*, vol. 51, no. 1, pp. 148–157, Feb. 2004.
- [11] Q. Zhao, A. Wang, and H. Wang, "Analysis resonant compensation for wireless power transfer via magnetic coupling," *Metallurgical and Mining Industry*, vol. 5, p. 46, 2015. [Online]. Available: [https://www.metaljournal.com.ua/assets/MMI\\_2014\\_6/MMI\\_2015\\_5/006-Qiang-Zhao.pdf](https://www.metaljournal.com.ua/assets/MMI_2014_6/MMI_2015_5/006-Qiang-Zhao.pdf)
- [12] S. Li, W. Li, J. Deng, T. D. Nguyen, and C. C. Mi, "A double-sided lcc compensation network and its tuning method for wireless power transfer," *IEEE TRANSACTIONS ON VEHICULAR TECHNOLOGY*, vol. 64, no. 6, 2015.
- [13] B. Bell and ajay Hari, "Topology key to power density in isolated dc-dc converters," *Power Electronics Technology*, Feb. 2011.
- [14] H. W. E. Koertzen, J. A. Ferreira, and J. D. van Wyk, "Comparative study of single switch induction heating converter using novel component effectivity concepts," *Power Electronics Specialists Conference IEEE*, vol. 1, pp. 298–305, 1992.
- [15] Z. Liu, "High frequency inverter power stage design considerations for non-magnetic materials induction cooking," Master's thesis, Virginia Polytechnic Institute and State University, 2011.
- [16] T. Barcelo, *Application Note 138 - Wireless Power User Guide*, Linear Technology, Oct. 2013.
- [17] N. Mohan, T. M. Underland, and W. P. Robbins, *Power Electronics: Converters, Applications, and Design*, 2nd ed. John Wiley & Sons, Inc., 1995.
- [18] W. Li, H. Zhao, S. Li, J. Deng, T. Kan, and C. C. Mi, "Integrated lcc compensation topology for wireless charger in electric and plug-in electric vehicles," *IEEE TRANSACTIONS ON INDUSTRIAL ELECTRONICS*, vol. 62, no. 7, Jul. 2015.

- [19] R. van Roy, *Introduction to RT1650 Wireless Power Receiver - AN036*, RICHTEK, Sep. 2015.
- [20] P. Belleau, "Wireless power for portable devices," Engineering Solutions Center, Arrow Electronics, techreport, Jan. 2016.
- [21] WPC, *Introduction to the Power Class 0 Specification*, version 1.2.3 ed., Wireless Power Consortium, Feb. 2017.
- [22] ———, *The Qi Wireless Power Transfer System Power Class 0 Specification. Parts 1 and 2: Interface Definitions*, version 1.2.3 ed., Wireless Power Consortium, Feb. 2017.
- [23] F. element 14, Sep. 2018. [Online]. Available: <https://nl.farnell.com/>



